ARMY RESEARCH LABORATORY

Optical Turbulence at Kitt Peak National Observatory, Fred Whipple Observatory, Apache Point Observatory, Horace Mesa, and the Atmospheric Profiler Research Facility

by Frank D. Eaton
John R. Hines
Battlefield Environment Directorate

James J. Drexler
James Northrup
Lockheed Engineering and Sciences Company

ARL-TR-1013

June 1996

DISCLAIMER NOTICE

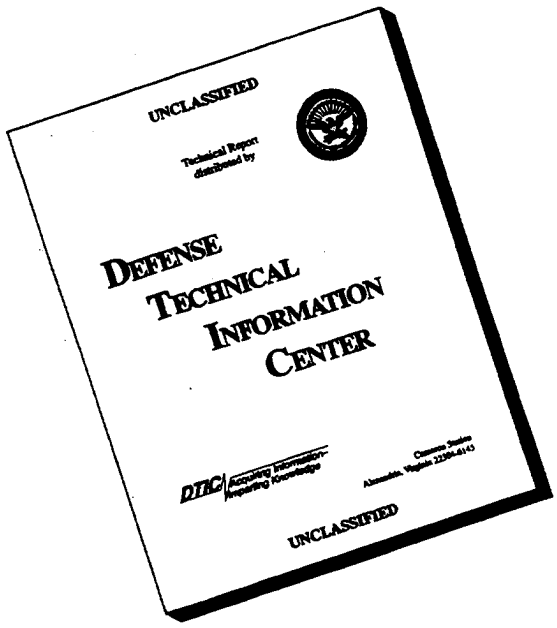

THIS DOCUMENT IS BEST QUALITY AVAILABLE. THE COPY FURNISHED TO DTIC CONTAINED A SIGNIFICANT NUMBER OF PAGES WHICH DO NOT REPRODUCE LEGIBLY.

NOTICES

Disclaimers

The findings in this report are not to be construed as an official Department of the Army position, unless so designated by other authorized documents.

The citation of trade names and names of manufacturers in this report is not to be construed as official Government indorse-ment or approval of commercial products or services referenced herein.

Destruction Notice

When this document is no longer needed, destroy it by any method that will prevent disclosure of its contents or reconstruction of the document.

REPORT DOCUMENTATION PAGE

Form Approved
OMB No. 0704-0188

1. AGENCY USE ONLY (Leave blank)	2. REPORT DATE	3. REPORT TYPE AND DATES COVERED
	June 1996	Final

4. TITLE AND SUBTITLE
Optical Turbulence at Kitt Peak National Observatory, Fred Whipple Observatory, Apache Point Observatory, Horace Mesa, and The Atmospheric Profiler Research Facility

5. FUNDING NUMBERS

6. AUTHOR(S)
Frank D. Eaton, John R. Hines (BED)
James J. Drexler, James Northrup (Lockheed Engineering and Sciences Company

7. PERFORMING ORGANIZATION NAME(S) AND ADDRESS(ES)
U.S. Army Research Laboratory
Battlefield Environment Directorate
Attn: AMSRL-BE-S
White Sands Missile Range, NM 88002-5513

8. PERFORMING ORGANIZATION REPORT NUMBER
ARL-TR-1013

9. SPONSORING/MONITORING AGENCY NAME(S) AND ADDRESS(ES)
U.S. Army Research Laboratory
2800 Powder Mill Road
Adelphi, MD 20783-1145

10. SPONSORING/MONITORING AGENCY REPORT NUMBER
ARL-TR-1013

11. SUPPLEMENTARY NOTES

12a. DISTRIBUTION/AVAILABILITY STATEMENT
Approved for public release; distribution is unlimited.

12b. DISTRIBUTION CODE
D

13. ABSTRACT *(Maximum 200 words)*

The transverse coherence length r_0 derived from differential image emotion of stellar sources, was measured at three astronomical sites (Kitt Peak National Observatory, Fred Whipple Observatory, and Apache Point Observatory), a high mesa (Horace Mesa), and in a desert basin (Atmospheric Profiler Research Facility) at White Sands Missile Range. Composite results of r_0 on the order of a few minutes are seen under convectively unstable conditions. The quiescent periods, neutral events, when local near surface adiabatic conditions occur, show substantial reductions in the fluctuations of the same quantity. Image motion results for night (stable) conditions display slowing and varying patterns with reduced short term (few minutes) variations.

Measurements were taken using a suite of instrumentation probing the same volume of atmosphere. The instrumentation includes the Atmospheric Turbulence Measurement and Observation System, a sodar, a scintillometer, and tower-mounted sensors. A time-height display of sodar data, calibrated for the refractive index structure parameter, C_n^2 coupled with scintillometer measurements show the diurnal evolution of the boundary layer responding to the local heating-cooling cycle and drainage flows from surrounding mountains. Several atmospheric features are seen and discussed in the results becasue they affect the nature of the patterns of r_0. Of particular interest are the development of convection, changes in the capping inversion, thermal plume structures, neutral events, and wave-turbulence interactions. Sinusoidal oscillations, identified as internal gravity waves, are seen in the night laminated structures.

14. SUBJECT TERMS
turbulence, r_0, KPNO, APO, APRF, C_n^2

15. NUMBER OF PAGES
117

16. PRICE CODE

17. SECURITY CLASSIFICATION OF REPORT	18. SECURITY CLASSIFICATION OF THIS PAGE	19. SECURITY CLASSIFICATION OF ABSTRACT	20. LIMITATION OF ABSTRACT
Unclassified	Unclassified	Unclassified	SAR

Preface

Measurements were taken of the transverse coherence length at three astronomical sites (Kitt Peak National Observatory, Fred Whipple Observatory, and Apache Point Observatory), a high mesa (Horace Mesa), and in the Tularosa Basin of White Sands Missile Range at the Atmospheric Profiler Research Facility using the Atmospheric Turbulence Measurement and Observation System. Additional measurements (taken with a sodar, a scintillometer, and a tower-mounted sensor at the research facility) were used to explain atmospheric effects on the patterns of results obtained from the Atmospheric Turbulence Measurement and Observation System. This work was partially supported by U.S. Air Force Phillips Laboratory and the University of New Mexico.

Acknowledgments

Special appreciation is expressed to William Hatch, Computer Specialist, for processing the surface data, and David Favier and Noah Montoya, electronics specialists. Their help made the study possible.

This work was partially supported by the U. S. Air Force Phillips Laboratory, contract monitor Robert Fugate. The University of New Mexico, contract monitor Neb Duric, partially supported the Horace Mesa mesurements.

Contents

Preface 1

Acknowledgments 3

Executive Summary 9

1. Introduction 11

2. Sites 13
2.1 Kitt Peak National Observatory 13
2.2 Fred Lawrence Whipple Observatory 14
2.3 Apache Point Observatory 14
2.4 Horace Mesa 15
2.5 Atmospheric Profiler Research Facility 15

3. Theoretical Basis of the Measurements and Instrumentation 17
3.1 Transverse r_o and the ATMOS 17
3.2 Profiles of C_n^2 and Sodar 19

4. Results and Discussions 21
4.1 KPNO 21
4.2 FLWO 21
4.3 APO 29
4.4 Horace Mesa 52
4.5 APRF 52

5. Conclusions 79

References 81

Acronyms and Abbreviations 87

Appendix 89

Distribution 105

Figures

1. Measurements of r_0 taken on 30 Mar 91 at KPNO 22
2. Frequency distribution of the measurements of r_0 taken on 30 Mar 91 at KPNO 23
3. Measurements of r_0 taken on 24 Aug 91 at KPNO 24
4. Measurements of r_0 taken on 26 Aug 91 at KPNO 25
5. Frequency distribution of the measurements of r_0 taken on 24 and 26 Aug 91 at KPNO 26
6. Measurements of r_0 taken on 29 Nov 90 at FLWO 27
7. Frequency distribution of the measurements of r_0 taken on 29 Mar 91 at FLWO 28
8. Measurements of r_0 taken on 21 May 94 at APO 30
9. Measurements of r_0 taken on 23 May 94 at APO 31
10. Measurements of r_0 taken on 22 May 94 at APO 32
11. Frequency distribution of the measurements of r_0 taken 21 and 22 May 94 at APO 33
12. Measurements of r_0 taken on 9 Jun 94 at APO 34
13. Frequency distribution of the measurements taken on 9 Jun 94 at APO . . . 35
14. Measurements of r_0 taken on 24 Jun 94 at APO 36
15. Measurements of r_0 taken on 25 Jun 94 at APO 37
16. Frequency distribution of the measurements of r_0 taken on 24 and 25 Jun 94 at APO 38
17. Frequency distribution for r_0 for Apr 95 at APO 39
18. Frequency distribution for r_0 for May 95 at APO 40
19. Frequency distribution for r_0 for Jun 95 at APO 41
20. Frequency distribution for r_0 for Jul 95 at APO 42
21. Frequency distribution for r_0 for Aug 95 at APO 43
22. Frequency distribution for r_0 for Sept 95 at APO 44
23. Frequency distribution for r_0 for Oct 95 at APO 45
24. Composite plot of r_0 measurements for Apr and May 94 and 95 at APO . . 46
25. Diurnal composite plot of r_0 measurements for Jun 94 and 95 at APO 47

26. Composite plot of r_o measurements for Jul 95 at APO 48
27. Composite plot of r_o measurements for Aug 95 at APO 49
28. Composite plot of r_o measurements Sept 95 at APO 50
29. Composite plot of r_o measurements for Oct 95 at APO 51
30. Measurements of r_o taken on 8 Nov 95 at Horace Mesa 53
31. Measurements of r_o taken on 9 Nov 95 at Horace Mesa 54
32. Distribution of the measurements of r_o taken on 8 and 9 Nov 95 at Horace Mesa 55
33. Measurements of r_o taken on 24 May 91 at the APRF 56
34. Measurements of r_o taken on 29 May 91 at the APRF 57
35. Measurements of r_o taken on 4 Jun 91 at the APRF 58
36. Measurements of r_o taken on 18 Jun 91 at the APRF 59
37. Frequency distribution of day measurements of r_o taken at the APRF during May and Jun 91 60
38. Frequency distribution of night measurements of r_o taken at the APRF during May and Jun 91 61
39. A continuous 24-h period of r_o measurements taken at the APRF on 8 Oct 91 62
40. Frequency distribution of r_o measurements taken during daylight on 8 Oct 91 63
41. Frequency distribution of r_o measurements taken during the night of 8 Oct 91 64
42. Diurnal cycle of C_n^2 measured with scintillometers mounted 4 and 20 m AGL at the APRF 66
43. Differential image motion variances for three 1-h periods during the day: a) 1100 to 1200 MST, b) 1630 to 1730 MST, and c) 2000 to 2100 MST 67
44. r_o calculations using the image motion results in figure 43 68
45. Time-height display of 1-min backscattered power sensed on 8 Oct 91. Backscatter is ordered as in a rainbow with red being the strongest return and dark blue being the weakest return. Black is the background strength. 70

46. Diurnal cycle of sodar-derived 5-m C_n^2 averaged over the height increment 119 to 276 m. 72
47. Coefficient of determination values (r^2) calculated for the ATMOS and scintillometer results (C_n^2) and the ATMOS and sodar results (C_n^2) for the 24-h period on 8 Oct 91. 74
48. Coefficient of determination values (r^2) calculated for the ATMOS and scintillometer results (C_n^2) and the ATMOS and sodar results (C_n^2) for the midnight to near sunrise period (0000 to 0630 MST). 75
49. Coefficient of determination values (r^2) calculated for the ATMOS and scintillometer results (C_n^2) and the ATMOS and sodar results (C_n^2) for the near sunrise period (0630 to 1715 MST). 76
50. Coefficient of determination values (r^2) calculated for the ATMOS and scintillometer results (C_n^2) and the ATMOS and sodar results (C_n^2) for the near sunset to midnight period (1715 to 2400 MST) 77

Executive Summary

Optical turbulence measurements were taken at Kitt Peak National Observatory, Fred Whipple Observatory, Apache Point Observatory, Horace Mesa and the Atmospheric Profiler Research Facility to characterize the "seeing" conditions at these sites. Short-term fluctuations in the transverse coherence length r_o, were examined under different atmospheric conditions such as free convection, stable (nighttime), and the quiescent events (times when the local near surface layer is adiabatic). The r_o measurements were taken using the Atmospheric Turbulence Measurement and Observation System by sensing differential image motion of stellar sources. Additional measurements using a scintillometer, sodar, and tower-mounted sensors at the Atmospheric Profiler Research Facility were used to examine the diurnal evolution of the boundary layer and explain the patterns of r_o. Various features in the planetary boundary layer, including gravity waves, convection, capping inversions, thermal plumes, and neutral events were identified and discussed as to their effects on "seeing" conditions.

1. Introduction

The refractive index structure parameter (C_n^2), including derived quantities such as the transverse coherence length (r_o) and the isoplanatic angle (θ_o), are of considerable interest to many propagation and remote sensing efforts using optical, radio, and acoustic techniques. Images observed at major astronomical observatories using large telescopes are degraded by atmospheric optical turbulence. Adaptive optics techniques, coupled with artificial or guide star approaches, are being implemented at various astronomical sites to mitigate turbulent effects on imagery. These efforts have generated new interest in understanding optical turbulence parameters.

Traditionally, optical turbulent effects known as astronomical seeing have been examined for selection and evaluation of observatory sites. The formulation of the r_o puts the classical seeing problem on a quantitative basis (Fried 1966). A derived quantity of C_n^2, r_o is defined as:

$$r_o = [0.423k^2 \int_o^\infty C_n^2(z)dz]^{-3/5} \quad (1)$$

where

k = $2\pi/\lambda$ (λ(m) is the wavelength of light)

z = the distance along the path between source and receiver (m).

Although r_o is an integrated path value, high-resolution profiles of C_n^2 can be sensed using thermosondes, state-of-the-art, clear-air radars, and acoustic sounders (Eaton et al. 1988a). This study also involves several types of instrumentation sensing the same volume of atmosphere for a 24-h period at White Sands Missile Range (WSMR). The ensemble of measurements is used to provide insight into the atmospheric phenomena responsible for observed patterns of r_o.

2. Sites

2.1 Kitt Peak National Observatory

Kitt Peak is a large astronomical facility housing two divisions of the National Optical Astronomy Observatories (NOAO): Kitt Peak National Observatory (KPNO) and the National Solar Observatory (NSO). KPNO operates the Mayall 4 m, the 2.1 m, the 0.9 m Coude' feed, and the Burrell Schmidt telescopes. A 3.5 m telescope, developed by the consortium of the University of Wisconsin, Indiana University, Yale University and the NOAO (WIYN), is operated by NOAO at Kitt Peak. The NSO telescope at Kitt Peak includes the McMath-Pierce Solar Telescope Facility, containing the world's three largest solar telescopes, as well as the Vacuum Telescope and the Razdow small solar patrol telescope.

Kitt Peak is located on the Tohono O'odham Reservation. Kitt Peak is 92 km southwest of Tucson, AZ. The elevation of the summit is 2095 m. Measurements presented in this report were taken with the Atmospheric Turbulence Measurement and Observation System (ATMOS) at 31° 45′ N, 111° 30′ W adjacent to the 2.1 m telescope on 30 March, 24 August, and 26 August 1991. Additional measurements that are not presented here were taken with an ATMOS charge-coupled device (CCD) camera and data system coupled to the 2.1 m telescope.

The National Science Foundation (NSF) signed a lease with the Tribal Council in 1959 for use of 200 acres on the mountaintop for the scientific facility. Other universities lease space from NSF for operation of telescopes, including the University of Arizona, Case Western University, the National Radio Astronomy Observatory (NRAD), the MDM Observatory (University of Michigan, Dartmouth College, and Massachusetts Institute of Technology) and the Southeastern Association for Research in Astronomy.

2.2 Fred Lawrence Whipple Observatory

The Fred Lawrence Whipple Observatory (FLWO) is located about 56 km south of Tucson, AZ on Mt. Hopkins. It is the largest field installation of the Smithsonian Astronomical Observatory outside Cambridge, MA. The site is known for its extremely dark skies, dry climate, and good seeing. The KPNO to the west and the Catalina Mountains installations, operated by the University of Arizona, are within lines of sight from Mt. Hopkins. Research activities at FLWO include spectroscopic observations of extragalactic, stellar, and planetary bodies, gamma-ray and cosmic-ray astronomy, solar energy research, and local environmental studies.

The peak of Mt. Hopkins at 2606 m above ground level (AGL) is the site for the large multiple mirror telescope jointly built and operated by the Smithsonian and the University of Arizona. Most of the instrumentation at FLWO is on a ridge at 2316 m AGL and includes a 1.5-m and 61-cm reflecting telescopes, a 10-m optical array, and a Baker-Nunn satellite tracking camera. The measurements presented in this report were taken on 29 Nov 90 with the ATMOS in the observation dome of the 1.5-m telescope located at 31° 40′ 48" N, 110° 53′ 04" W.

2.3 Apache Point Observatory

Apache Point Observatory (APO) is an astronomical observatory located in the Lincoln National Forest in the Sacramento Mountains, NM, at an altitude of 2800 m mean sea level (MSL). It is owned and operated by the Astrophysical Research Consortium consisting of the University of Chicago, Institute of Advanced Study, Johns Hopkins University, New Mexico State University, Princeton University, University of Washington, and Washington State University. APO was established for operation on 10 May 94 when the 3.5-m multipurpose telescope observed a solar eclipse. This telescope is located at 32° 46′ 50.4" N, 105° 49′ 11.7" W.

Three other telescopes at APO are in various stages of completion. One unique-purpose telescope under design is the Sloan Digital Sky Survey (SDSS)

telescope that will be used under appropriate seeing conditions to survey the night sky with sensitive imaging equipment. The SDSS telescope was constructed on pillars west of the mountain ridge to reduce degrading turbulent conditions, because excellent seeing is a requirement for this effort. The ATMOS used in this study was first mounted atop the pedestal constructed for future installation of the 2.5-m SDSS telescope. Measurements were taken on 21, 22, and 23 May and 9, 24, and 25 Jun 94. The ATMOS was relocated in a portable dome south of the 3.5-m telescope. Measurements were taken 14, 26, and 27 Apr, and 25 through 31 May 94. 1 through 5, 7, 9, 13 through 17, 19, 28, and 29 Jun, 1, 3, 9 through 14, 21, 23 through 31 Jul, 2, 11, 13, 22, and 23 Aug, 3 through 7, 12, 13, and 21 through 28 Sept, 1, 3 through 22 and 31 Oct 95.

2.4 Horace Mesa

Horace Mesa is a large mesa located northwest of Grants, NM. The top edge of the mesa is 2250 m MSL with the closest part of the edge being about 10 km from Grants. The mesa has steep walls to the south, west, and north. Mt. Taylor is located northeast of the mesa at 3445 m MSL. Of particular interest are the lava flows located throughout the area. The surface at the measurement site has black lava rock mixed with soil. Vegetation is grasses, herbaceous plants, and sparse pinon and juniper trees.

The ATMOS was operated about 50 m back from the western edge of the mesa edge at 107° 43′ 13.3" W, 35° 5′ 17.3" N. Measurements of r_o were taken at night on 8 and 9 Nov 95.

2.5 Atmospheric Profiler Research Facility

Measurements of optical turbulence were taken with the ATMOS at the Atmospheric Profiler Research Facility (APRF) on 24 and 29 May, 4 and 18 Jun, and 8 Oct 91. The 8 Oct measurements were taken over a 24-h period with a sodar ATMOS, and a scintillometer. A complete description of all equipment at the facility, including optical devices, instrumented towers, and a radiation station is described by Hines et al. (1993).

The APRF is located in the Tularosa Basin at 32° 24′ N, 106° 21′ W and is approximately 10 km east of the headquarters area of WSMR, NM. The elevation of the site is 1220 m MSL and is characterized by low brush (predominantly mesquite), associated desert grasses, and other herbaceous plants indigenous to the Chihuahuan Desert. The San Andres and Organ Mountains, part of the southern end of the Rocky Mountains, run north-south and are located west of the APRF. Organ Peak, 2704 m MSL, is the highest peak in the Organ Mountains and is 13 km southwest of the APRF. The mountains are steep and create a physical knife edge affecting airflow from the predominant southwesterly to westerly wind directions. The slopes support piñon pine and juniper trees with ponderosa pine trees interspersed at higher elevations. The Sacramento Mountains are about 30 km east of the APRF, also running north-south. Peaks in the Sacramento Mountains exceed 2800 m MSL, slightly above the lower boundary of the spruce-fir forest type.

Specific climatological records for the APRF do not exist. However, the climatology for WSMR has been compiled (Hoidale et al. 1975; Taft and Hoidale 1969) and provides insight into the local climatology. The general climate is continental arid with an annual precipitation of 180 to 280 mm. Seventy percent of the annual rainfall occurs from June through October as a result of moist air advection. Thunderstorm activity and associated cloud cover are high during this time of the year with the maximum number of storms in July. A case study of the onset of the summer monsoon over WSMR in June, as seen by the APRF 50 MHz radar, is found in Nastrom and Eaton (1993). Temperature, wind, and cloud-cover data have been taken at other sites at WSMR. Typically, October has the highest number of clear sky conditions of any month at the APRF. A 24-h period of clear sky conditions was required for an aspect of this study. This was not found for several months prior to 8 Oct 91.

3. Theoretical Basis of the Measurements and Instrumentation

Different techniques are used to measure r_0 and profiles of C_n^2: the theoretical basis for each of the different measurement techniques used is discussed. The principal instrumentation used in this study includes an ATMOS and a sodar.

3.1 Transverse r_0 and the ATMOS

Seeing conditions have been incorporated for over 59 yrs using various experimental techniques, such as sensing image spread and wander by photography or photoelectric devices (Whitford and Stebbins 1936; Couder 1936). Moroder and Righini (1973) used image motion extracted from photographic recordings to calculate r_0 from a single aperture telescope. Because photographic techniques are tedious to analyze and high frequency information generally is lacking, Forbes (1982) designed and used a system incorporating a charge injected diode camera as the detector. Recognizing that errors are introduced in determining r_0 from vibration effects, Merrill et al. (1986) used a dual-beam approach to provide differential image motion measurements. An application of this approach was the implementation of an optical glass wedge. The wedge was placed over one of the two subapertures to allow the images from the two subapertures to be separated and in focus at the focal plane. As a result, the two distinct images provide easy determination of centroids and eliminate the need for a defocus correction (Miller and Kellen 1975). Roddier (1981) summarized the dual-beam approach to centroid location. Fried (1975) evaluated the theory and measurement feasibility of this technique using differential motion.

Technology developments have been incorporated into seeing monitors, such as replacing film techniques with linear array CCD's to obtain the line-spread function. Analyses of such information to obtain r_0 from the modulation transfer function as well as the technique used in this study, differential image motion, are documented in Eaton et al. (1988b). The same differential image motion technique using four pairs of apertures was used to experimentally determine the phase-structure function (Eaton et al. 1989).

In this study, a telescope equipped with two subapertures (ATMOS) is used to sense the relative distance between the centroids of two stellar images. Image motion that is related to angle-of-arrival fluctuations, is produced by fluctuations of the phase front of the received light. The following relationship is used in this study to calculate r_o, as developed by Roddier (1981):

$$r_o = \{\frac{27.5\ F^2}{k^2\ d^{1/3}\sigma_r^2}[1-\frac{25}{36}(\frac{d}{\mu})^{1/3}]\}^{3/5} \qquad (2)$$

where

F = the focal length of the receiving telescope (m)
d = the diameter of each subaperture (m)
μ = center-to-center separation of the subapertures (m)
σ_r^2 = mean-square of the relative distance between the centroids of the two images (m^2).

The ATMOS uses a differential angle-of-arrival approach by collecting light from a single star with two subapertures (11-cm diameter) on a 35.5-cm diameter telescope. The subapertures have optical glass wedges so the two images are separated and focused onto a two-dimensional CCD camera that is placed at the focal plane. Two nearly parallel paths of turbulence are measured at 23.5-cm separation. As proposed by Merrill et al. (1986), the method eliminates common system errors caused by tracking errors, vibration, and wind loading because such effects will display identical image motion and not be included in the variance of centroid differences. The ATMOS includes a frame grabber that can vary exposure time and frame rates up to an excess of 300 frames per second (fps). The CCD camera is intensified and uses an electronic shutter capable of limiting exposure times to as short as 25 μs. The camera and frame grabber have been incorporated into an optical schlieren system to examine the evolution of atmospheric transparent inhomogeneities (Eaton et al., 1990).

Noise of the complete ATMOS system (consisting of the optics, detection, digitization, and recording equipment) was evaluated by a method suggested by Merrill et al. (1986). By placing a birefringent quartz Rochon prism over one subaperture, the Rochon prism produces two images of known separation on the

detector from a single source, either laser or stellar. Data reduction is performed with methods similar to those for the dual aperture approach. The sensed differential image motion with this arrangement is due to system noise. Eaton et al. (1989) compared ATMOS noise levels to actual data and found the signal-to-noise ratio generally exceeded 50/1 for normal operating conditions.

3.2 Profiles of C_n^2 and Sodar

Profiles of the temperature structure function (C_T^2) were obtained from sodar techniques of sonic detection and ranging. C_n^2 ultimately is derived from the relationship described by Tatarskii (1961).

$$C_n^2=(\frac{79p}{T^2}x\ 10^{-6})^2C_T^2 \tag{3}$$

where

p = atmospheric pressure in mb
T = absolute temperature.

The following sodar equation was developed by Forbes et al (1985) and used in this study.

$$C_T^2 = \frac{P_r T_o^2 e^{2\bar{\alpha}R} L_e}{E_r[P_t \cdot E_t][(\frac{c\tau}{2})(\frac{A}{R^2} \cdot G)][0.0039k^{1/3}]} \tag{4}$$

where

P_r = the received power (W)
P_t = the transmitted power (W)
R = the sodar range (m)
T_o = surface temperature (°K)
$\bar{\alpha}$ = molecular and classical adsorption (m^{-1})
E_r = receiver efficiency
E_t = transmitter efficiency
c = speed of sound (m\s)
τ = pulse length (s)

A = antenna area (m^2)
G = antenna directivity
L_e = excess attenuation coefficient
k = wave number (m^{-1}).

The sodar used is an Echosonde model three-axis system manufactured by Radian Corporation. The three antennas are 1.5-m diameter. The sodar is typically operated at 1850-Hz and 86-W transmitted power using a 40-ms pulse length. Backscatter (for deriving C_T^2) is averaged every 30 s in 200 range gates for obtaining C_n^2 from 19 through 276 m AGL. Some researchers obtain C_T^2 values from sodar by comparing the backscattered values to those obtained by in situ measured values from tower sensors. Calibration of the sodar used in this study was accomplished by a first-principles approach that accounted for the various terms in equation 7. Intercomparisons of the C_n^2 values derived from the sodar have been made with spatially separated temperature probes mounted at several heights on a 152-m tower. Agreement between the two systems is within 3 dB. The excess attenuation coefficient L_e is a complex function of the measured C_n^2, mean horizontal wind, and nominal beam width. Forbes et al. (1985) developed a method to estimate L_e. Using this technique, the actual beam width and the light winds sensed by tower-mounted sensors on 8 Oct 91, L_e was found to be near 1.0. Therefore, an L_e value of 1.0 was used for this study.

4. Results and Discussions

Results of r_0 measurements are presented separately for each of the five sites; KPNO, FLWO, APO, Horace Mesa, and the APRF.

4.1 KPNO

Measurements of r_0 were taken at KPNO during two periods; one on 30 Mar 91 and the other 23 through 26 Aug 91. A small, portable, 8-ft diameter observation dome was set up outside the 2.1-m telescope dome for these campaigns. Snow fell on 28 Mar 91, with snow cover remaining on the ground for the next two nights. The conditions were clear, breezy, and cold with frost occasionally forming on the optical wedges of the ATMOS on 30 Mar 91. The first night (23 Aug 91) of the second measurement session was cloudy, rainy, and windy. Sufficient clearing occurred so a few stars could be observed by 2200 mountain standard time (MST) on 23 Aug 91. Scattered clouds persisted for the remainder of the measurement period.

Figure 1 shows a time series of r_0 measurements on 30 Mar 91 for about a 10-h period. Figure 2 shows a frequency distribution of the 99 data sets. The r_0 values range from about 6 to 14 cm with most of the values between 8 and 12 cm. The August measurements, shown in figures 3 and 4, show a higher fraction of poorer seeing than for the March period. As displayed in figure 5, the r_0 values for August are distributed from 4 to 13 cm with a large contribution in the poorer seeing part of the distribution.

4.2 FLWO

The ATMOS was operated inside the observation dome used for the 1.5-m telescope on 29 Nov 90. During this measurement period, the weather was windy, gusting to 8 mps, and cold. Fred Forbes of KPNO operated his r_0 system on the 1.5-m telescope and stated that these were the worst seeing conditions he had experienced on Mt. Hopkins. Figure 6 shows the November time series of r_0 measurements taken with the ATMOS. As shown in figure 7, the March values ranged from 3 cm to slightly above 9 cm.

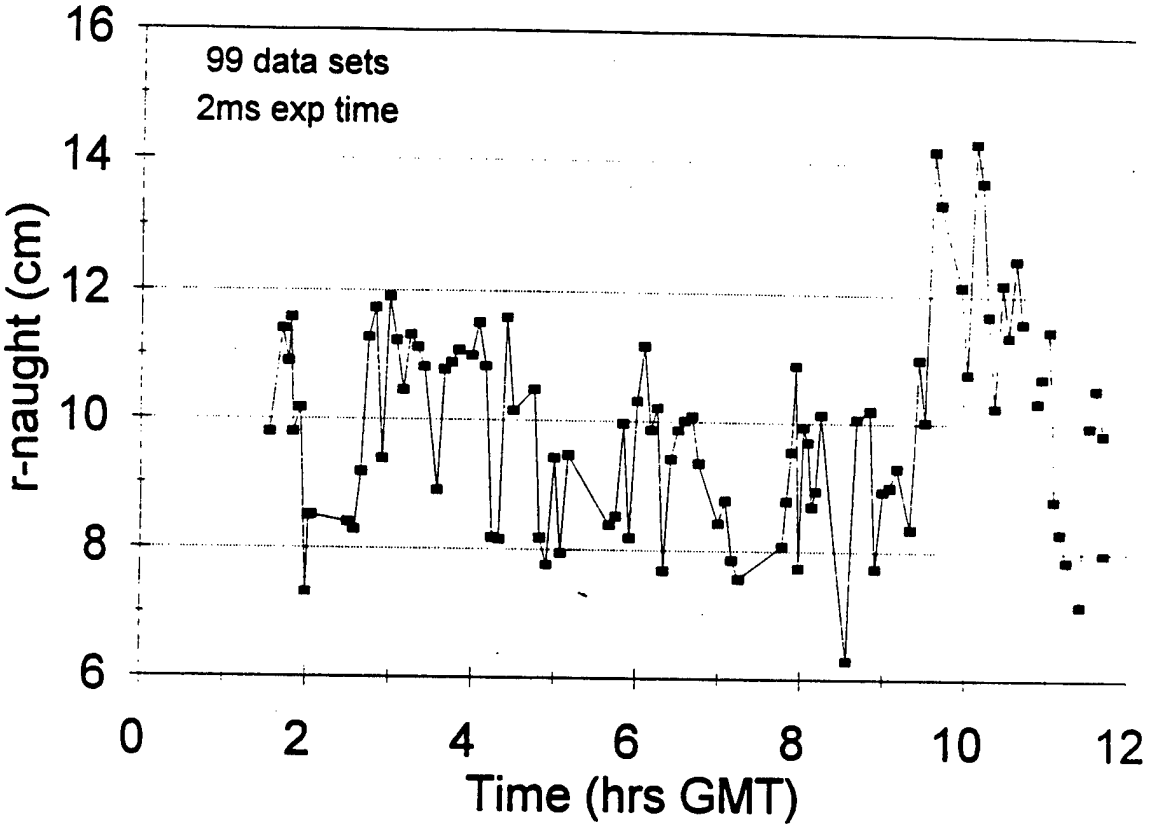

Figure 1. Measurements of r_0 taken on 30 Mar 91 at KPNO.

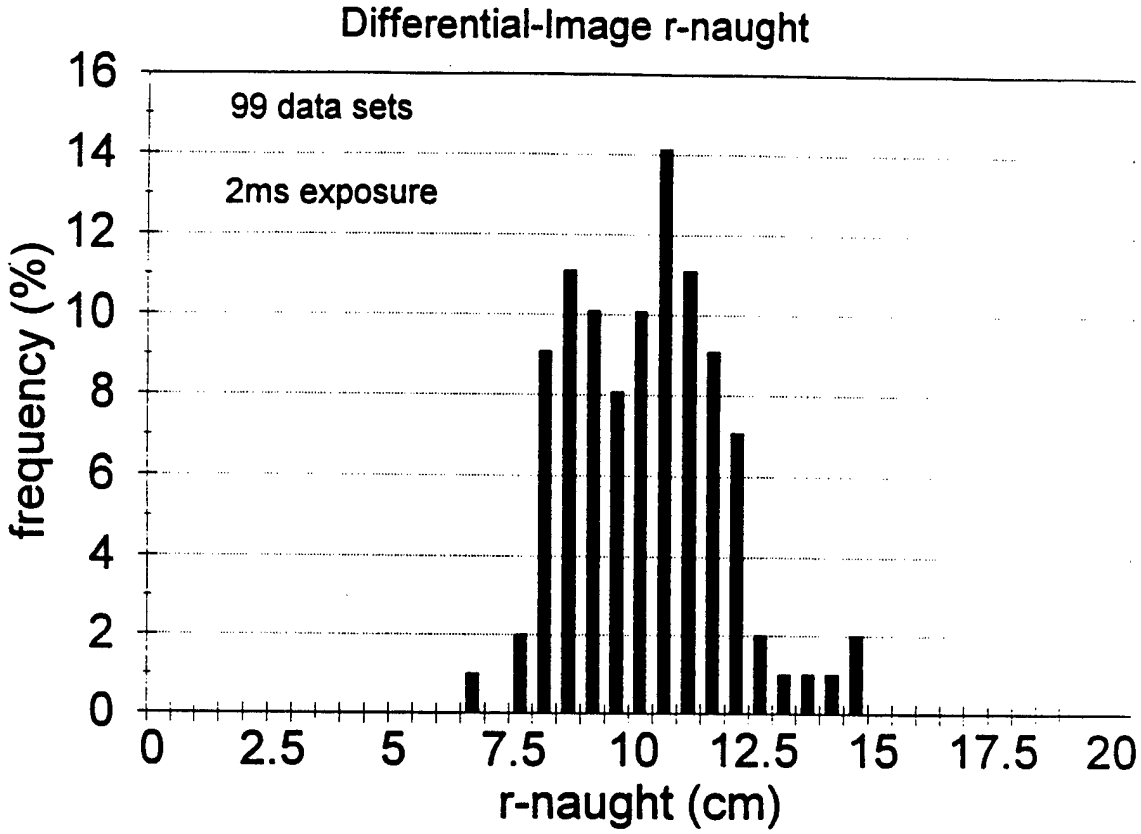

Figure 2. Frequency distribution of the measurements of r_o taken on 30 Mar 91 at KPNO.

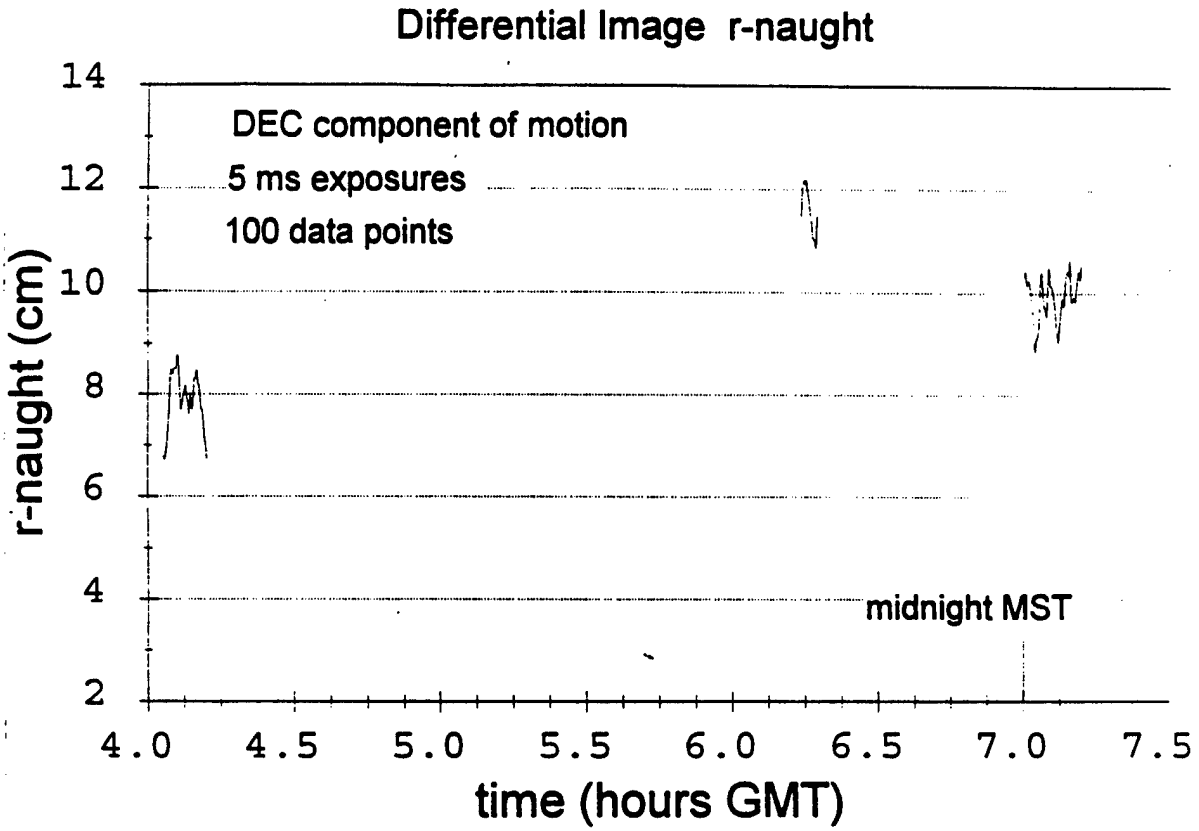

Figure 3. Measurements of r_o taken on 24 Aug 91 at KPNO.

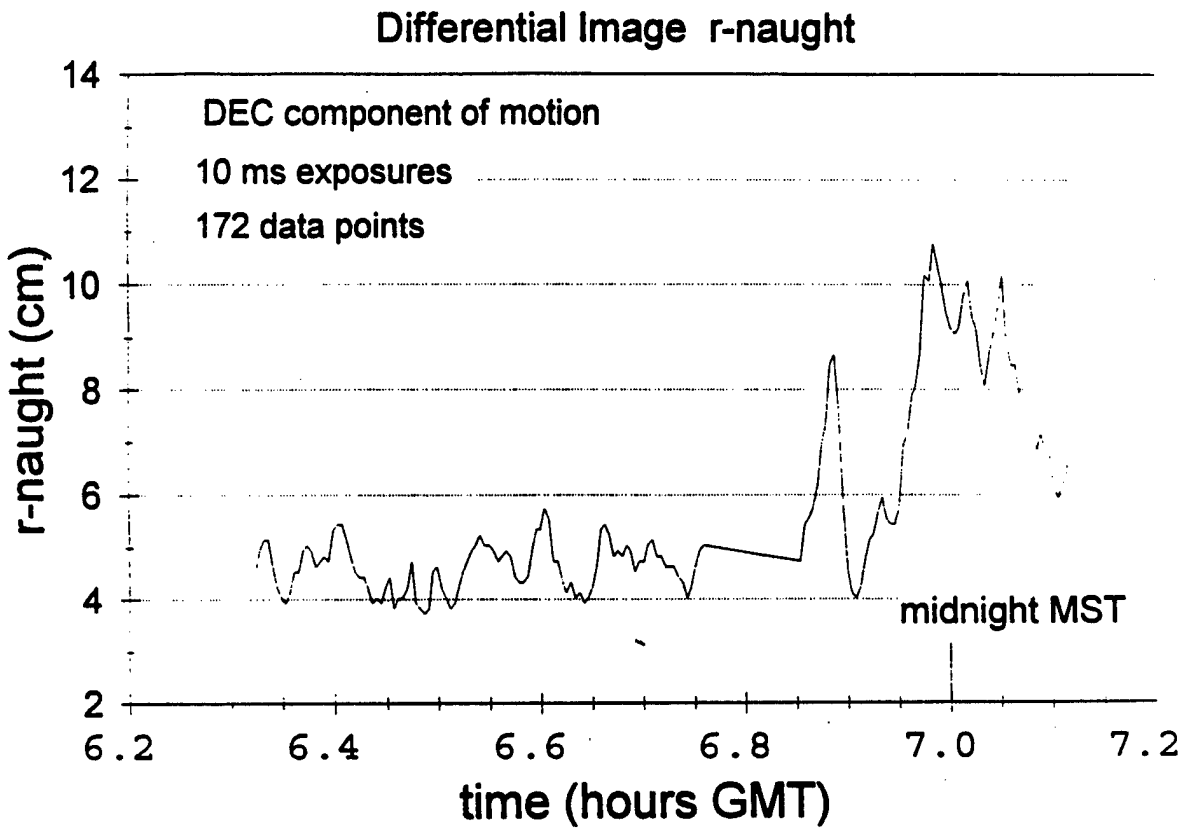

Figure 4. Measurements of r_o taken on 26 Aug 91 at KPNO.

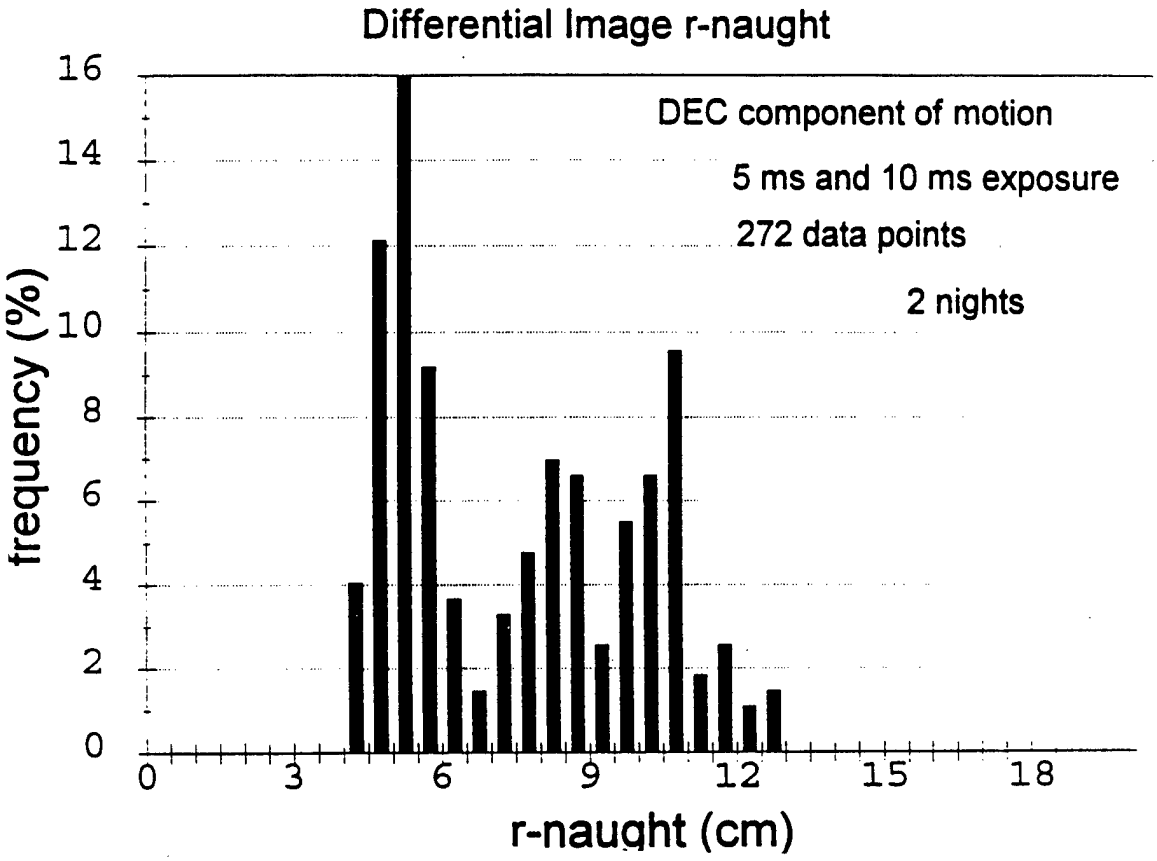

Figure 5. Frequency distribution of the measurements of r_o taken on 24 and 26 Aug 91 at KPNO.

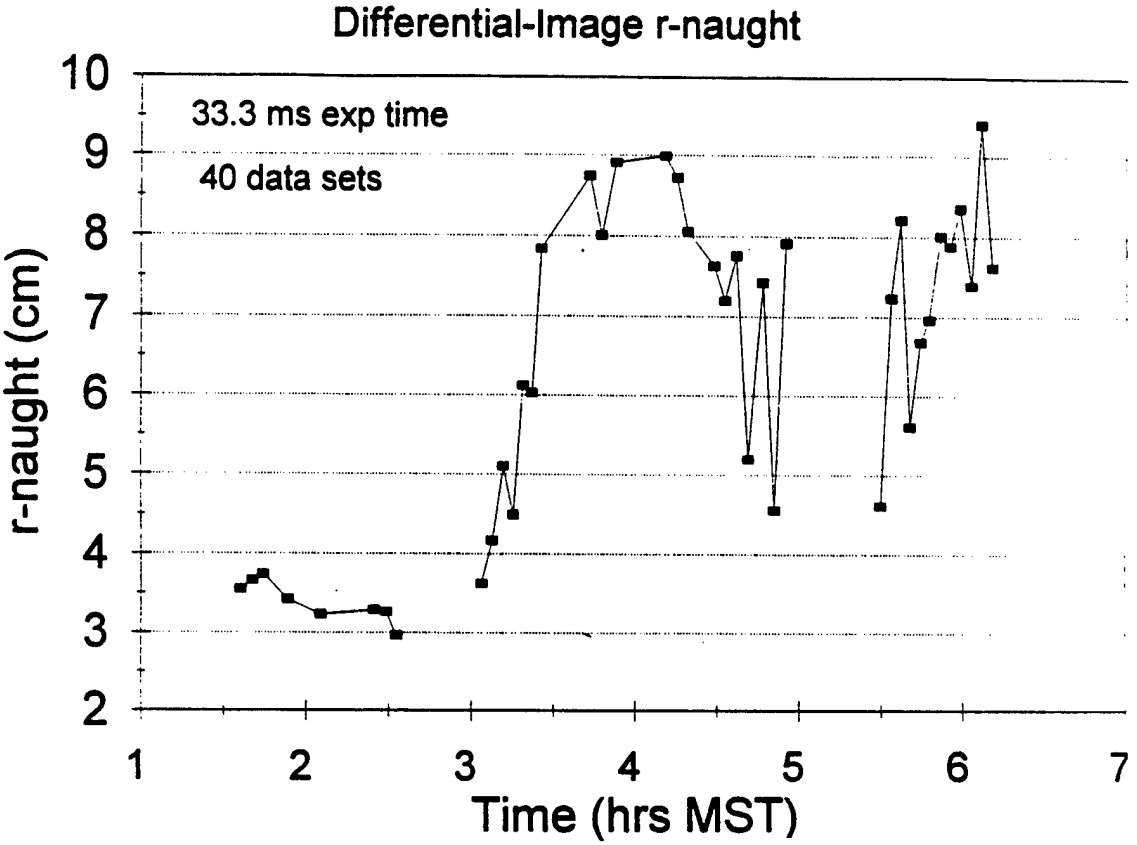

Figure 6. Measurements of r_0 taken on 29 Nov 90 at FLWO.

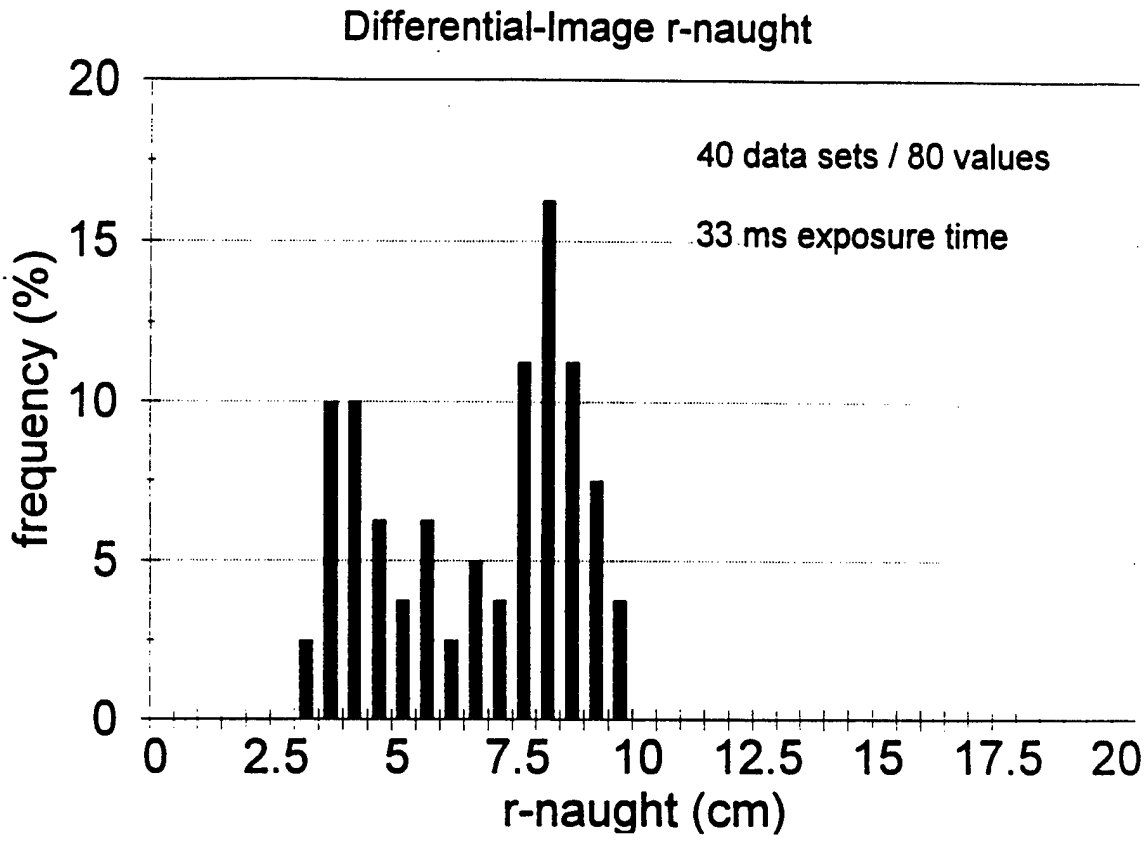

Figure 7. Frequency distribution of the measurements of r_o taken of 29 Mar 91 at FLWO.

4.3 APO

As previously listed in section 2.3, APO in the site description section, measurements of r_0 were taken on six nights during the spring of 1994 and on 84 nights in 1995. Some measurements were also taken during daylight, within the measurement periods. The time series of the r_0 values for 1995 are in the appendix. Frequency distributions of the data per month are displayed in this section. For convenience to the reader, the frequency distributions for each month in 1995 are also included in the appendix after each monthly presentation of r_0 time series. Diurnal monthly or bimonthly composite plots are also shown for the r_0 results. Figures 8 through 10 show the r_0 measurements for 21, 22 and 23 May 94. Figure 11 shows the frequency distribution of the 477 data sets during May 94. Figure 12 shows r_0 measurements taken on 9 Jun 94 with 1-ms exposure time. Figure 13 shows the corresponding frequency distribution. Figures 14 and 15 show measurements taken on 24 and 25 Jun 94. Because exposure times varied from 1 to 20 ms (as annotated in the figures), the data was used in a separate frequency distribution (figure 16) from that for 9 Jun. Figures 17 through 23 show individual monthly frequency distributions of r_0 for Apr to Oct 95. During 1995, 16,821 r_0 data sets were measured at APO. Most of the frequency distributions display the anticipated lognormal, or near lognormal shapes. The distributions that deviate from smooth shapes are derived from months with the smallest number of data points. Although the distributions vary somewhat month-to-month, most of the values measured during 1995 fell between 2.5 and 12.5 cm.

Figure 24 shows a diurnal composite plot of the combined r_0 measurements taken during Apr and May of 94 and 95. The measurements represent the whole night and show an improvement in seeing during 1200 to 1400 Greenwich Mean Time. Figure 25 shows the diurnal composite plot of the combined Jun 94 and 95 measurements. The r_0 values shown for approximately the first 2 h occurred just before sunset on 24 Jun 94. The dramatic increase (from 2.5 to 16 cm) is attributed to entering the evening neutral event. This pattern was enhanced from strong solar heating during late afternoon on the west-facing slope adjacent to the ATMOS. Figures 26 through 29 display the Jul to Oct 95 composite diurnal r_0 plots. No distinct trends or patterns are seen in these presentations. There is a separation in the r_0 values during the first

four hours during October. The unusual low measured values are primarily from the night of 14 Oct 95.

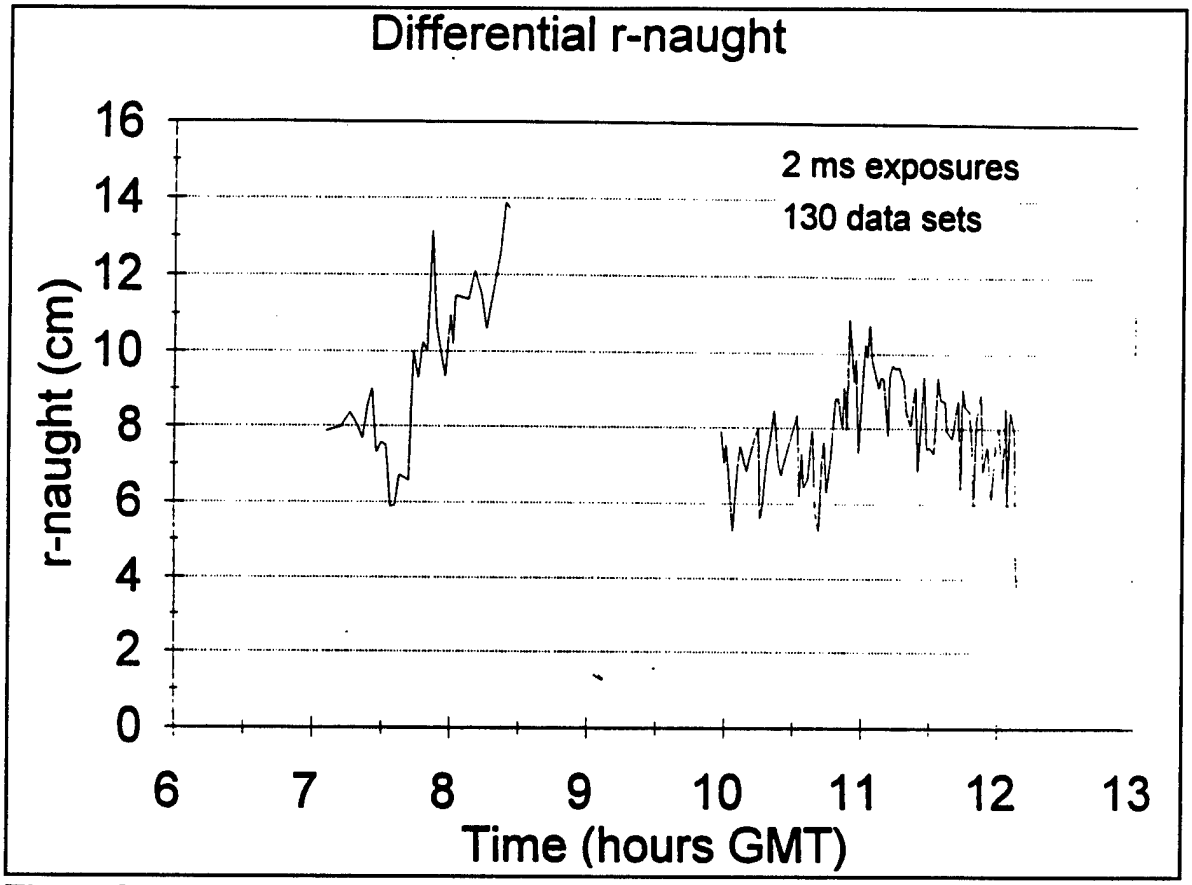

Figure 8. Measurements of r_o taken on 21 May 94 at APO.

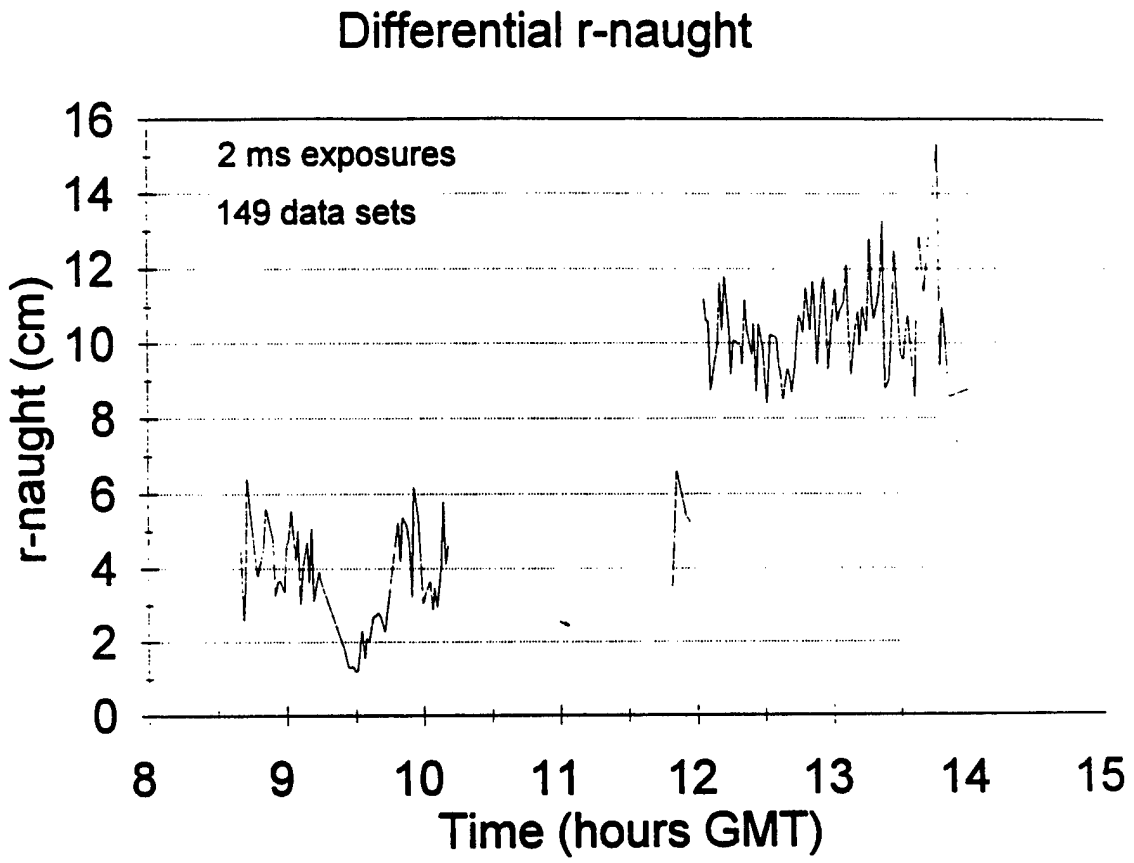

Figure 9. Measurements of r_o taken on 22 May 94 at APO.

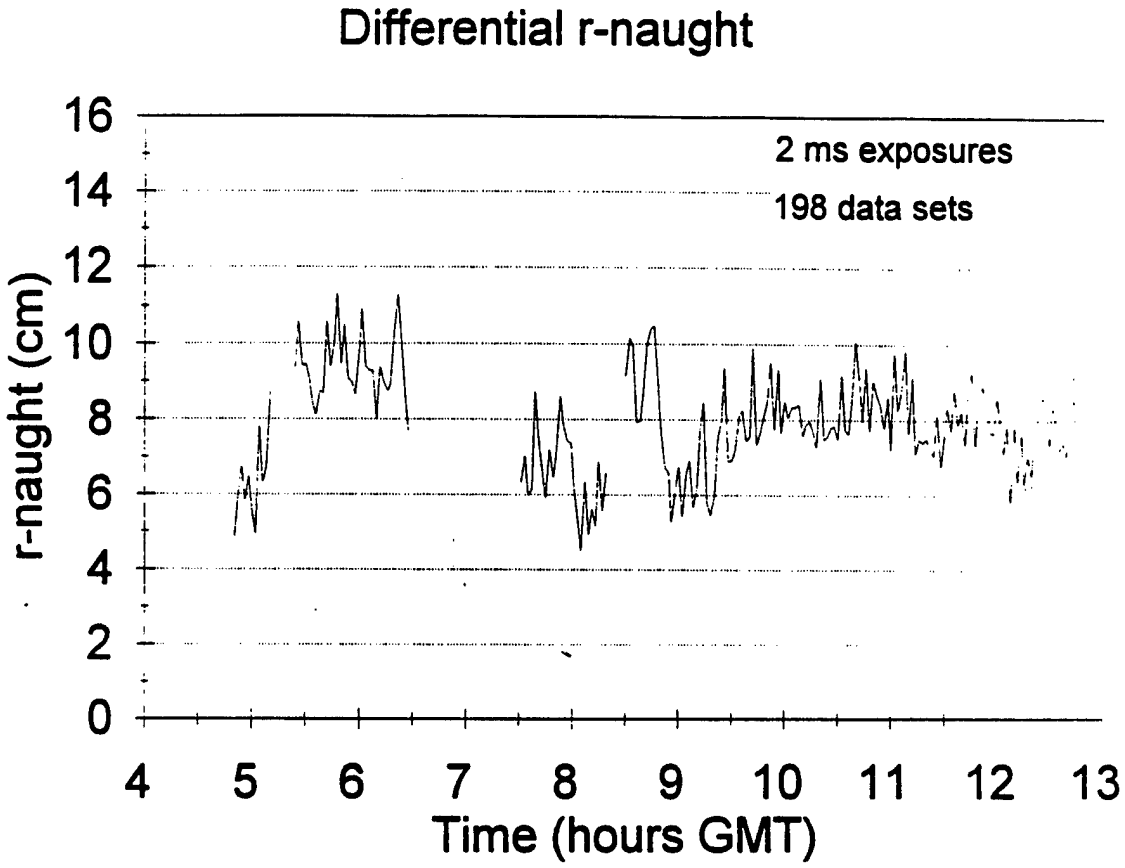

Figure 10. Measurements of r_0 taken on 23 May 94 at APO.

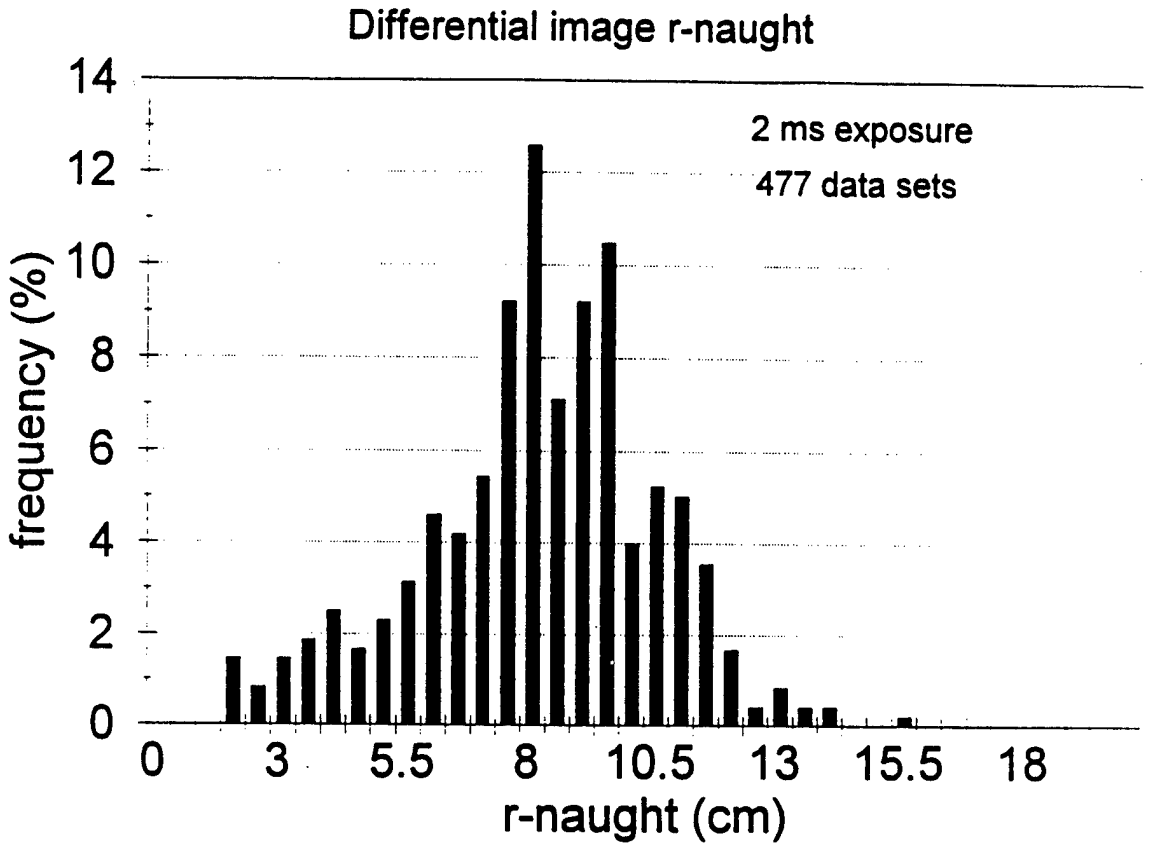

Figure 11. Frequency distribution of the measurements of r_o taken 21 and 22 May 94 at APO.

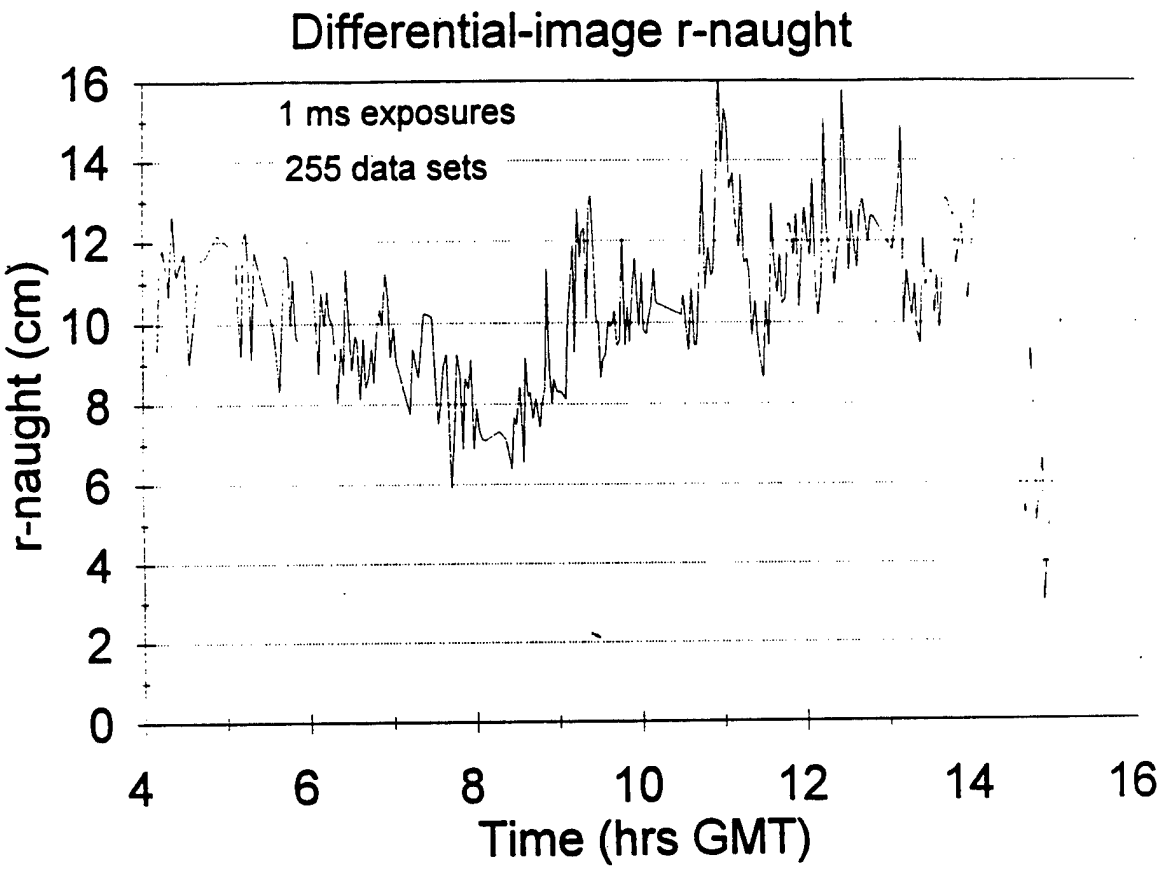

Figure 12. Measurements of r_0 taken on 9 Jun 94 at APO.

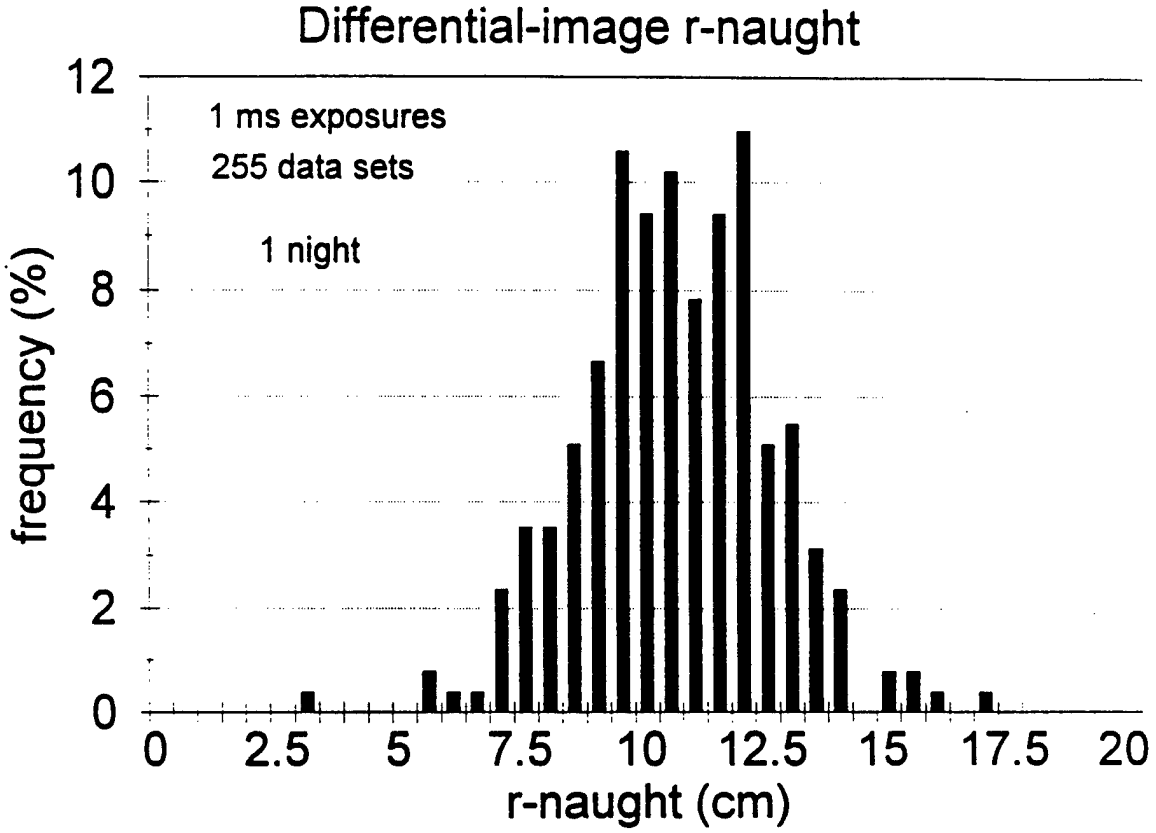

Figure 13. Frequency distribution of the measurements taken on 9 Jun 94 at APO.

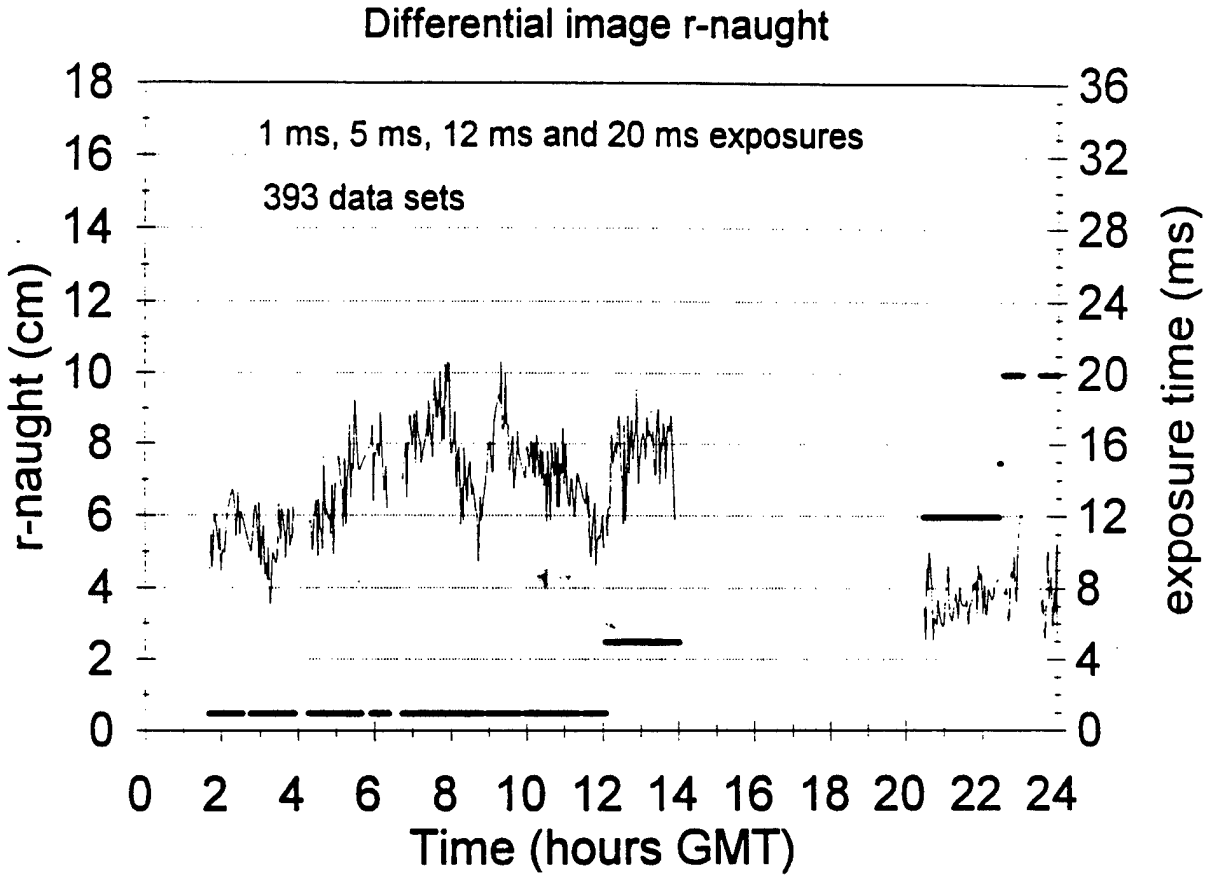

Figure 14. Measurements of r_0 taken on 24 Jun 94 at APO.

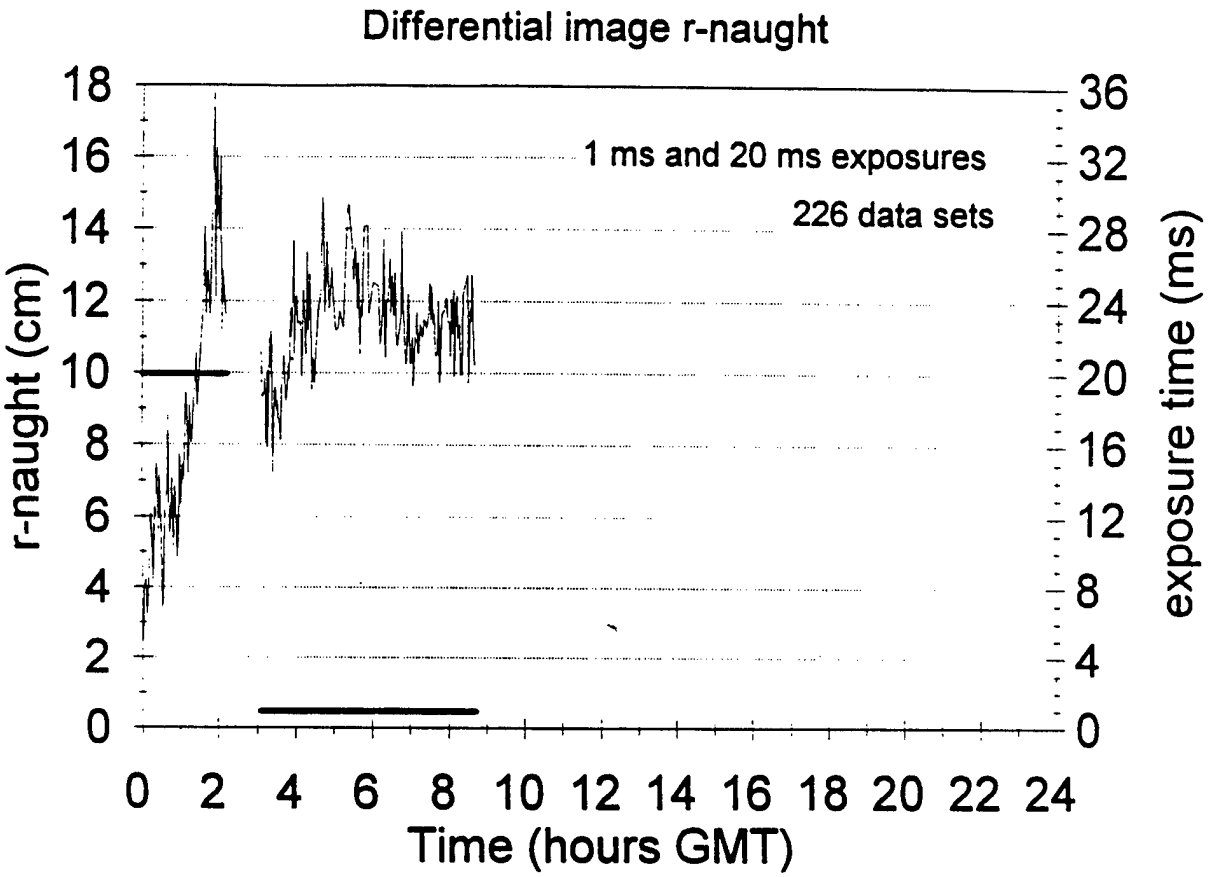

Figure 15. Measurements of r_0 taken on 25 Jun 94 at APO.

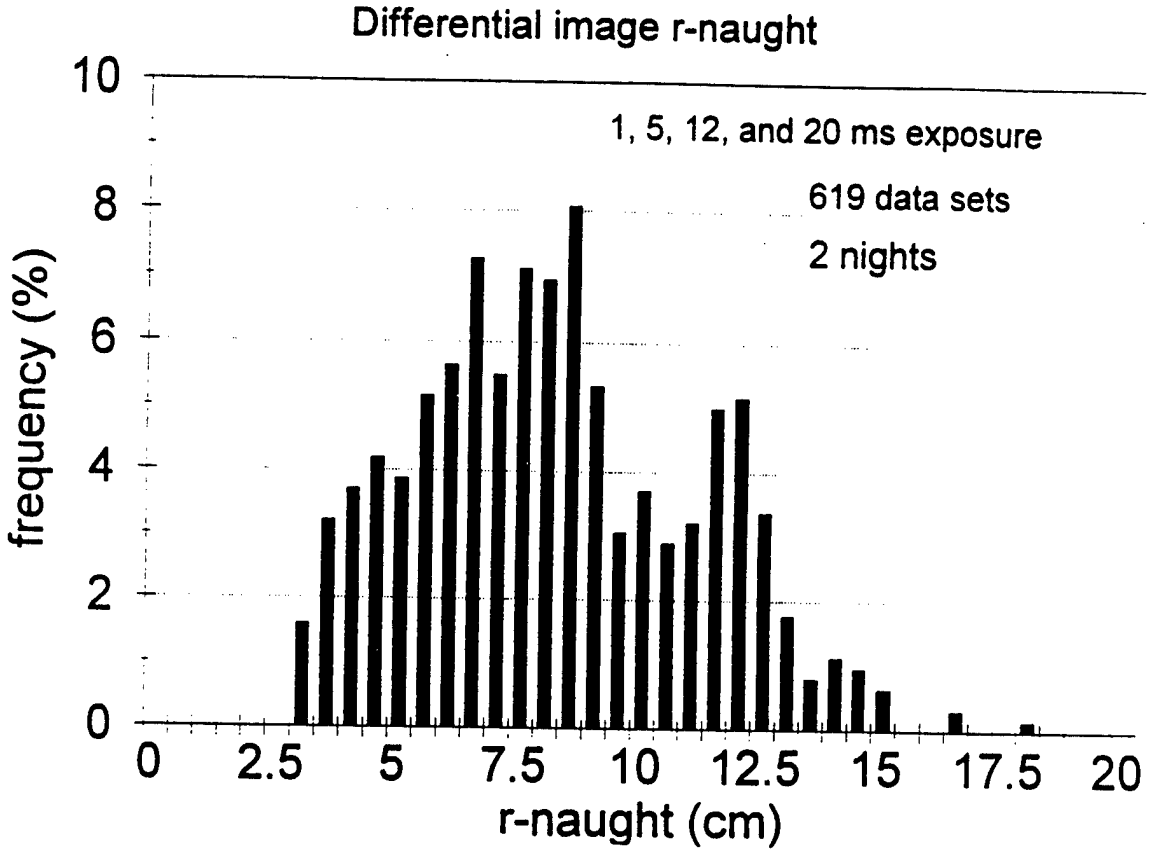

Figure 16. Frequency distribution of the measurements of r_o taken on 24 and 25 Jun 94 at APO.

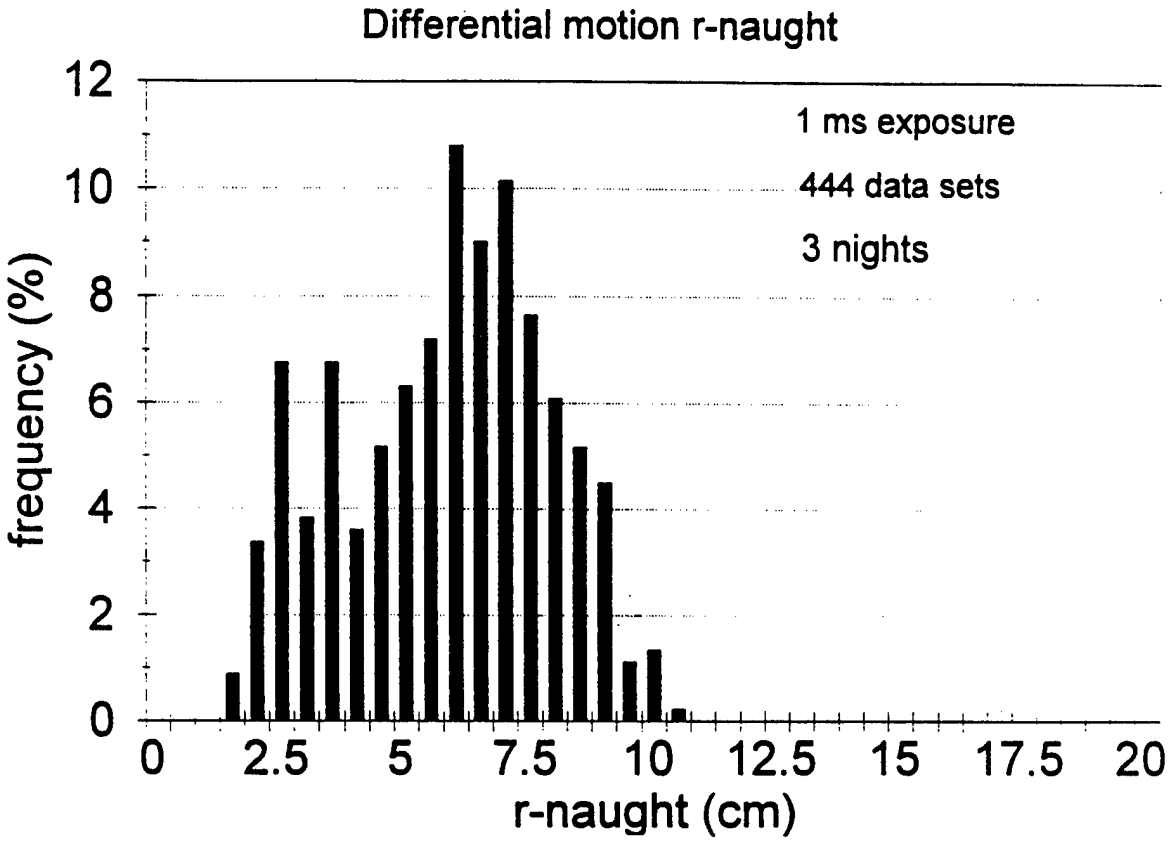

Figure 17. Frequency distribution for r_0 for Apr 95 at APO.

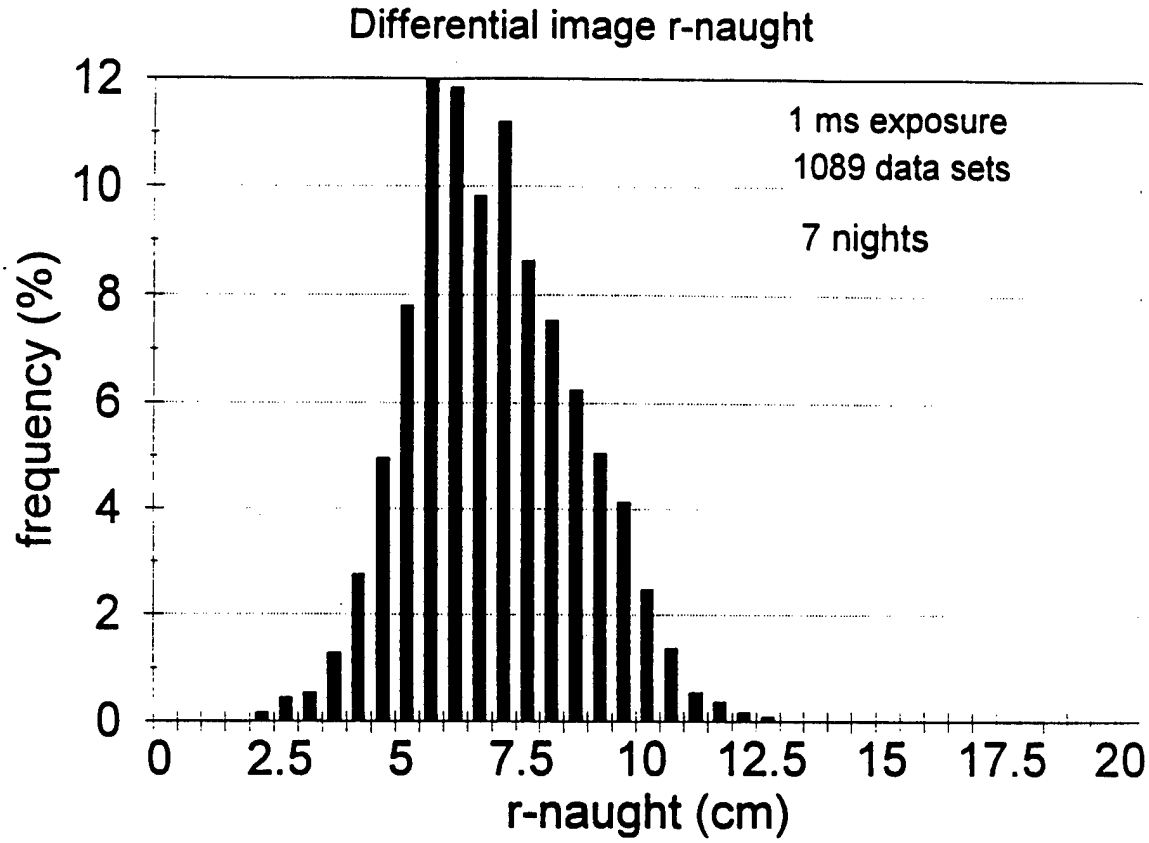

Figure 18. Frequency distribution for r_o for May 95 at APO.

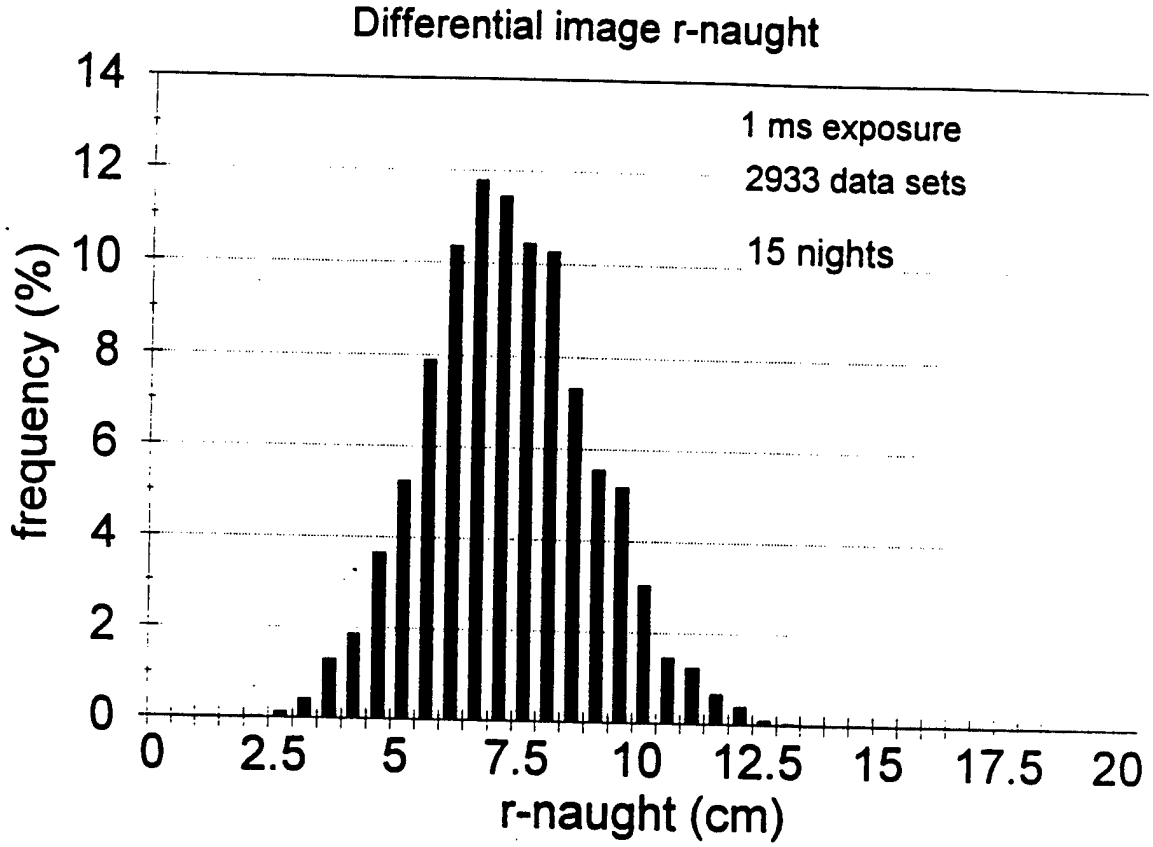

Figure 19. Frequency distribution for r_o for Jun 95 at APO.

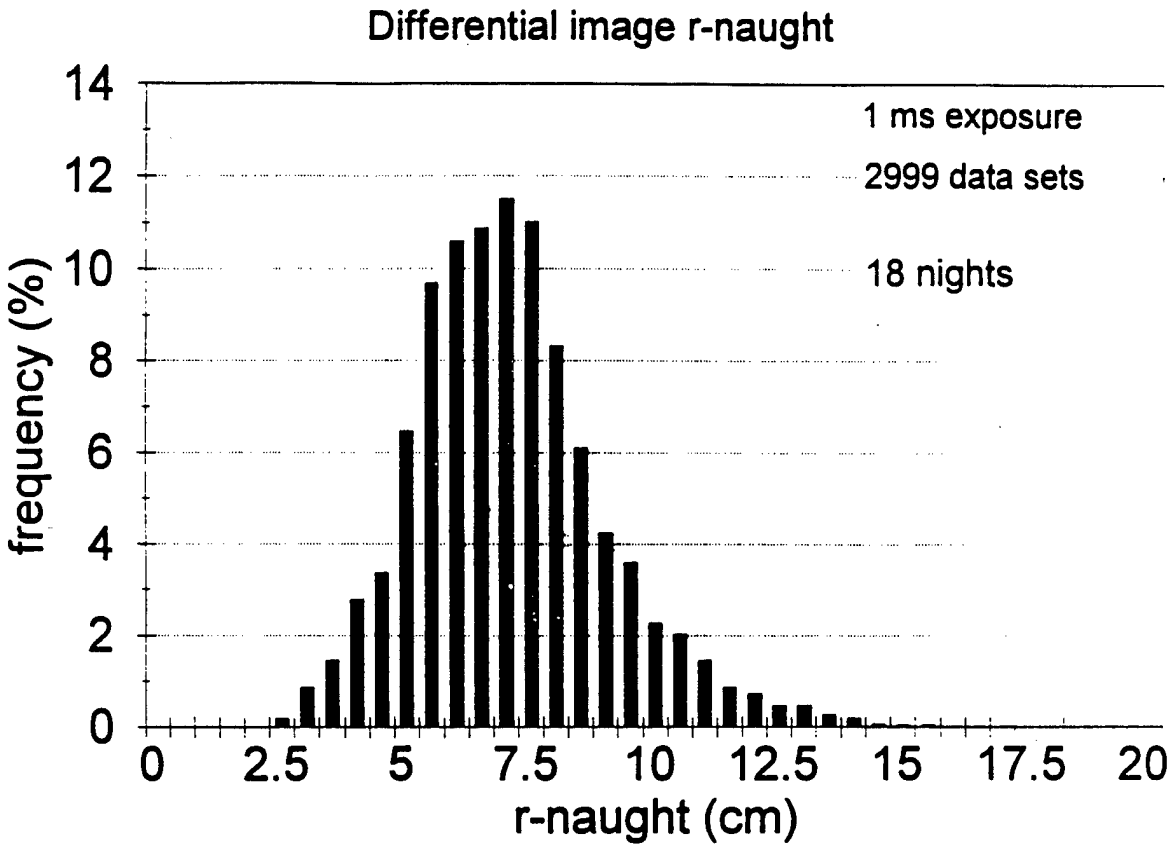

Figure 20. Frequency distribution for r_0 for Jul 95 at APO.

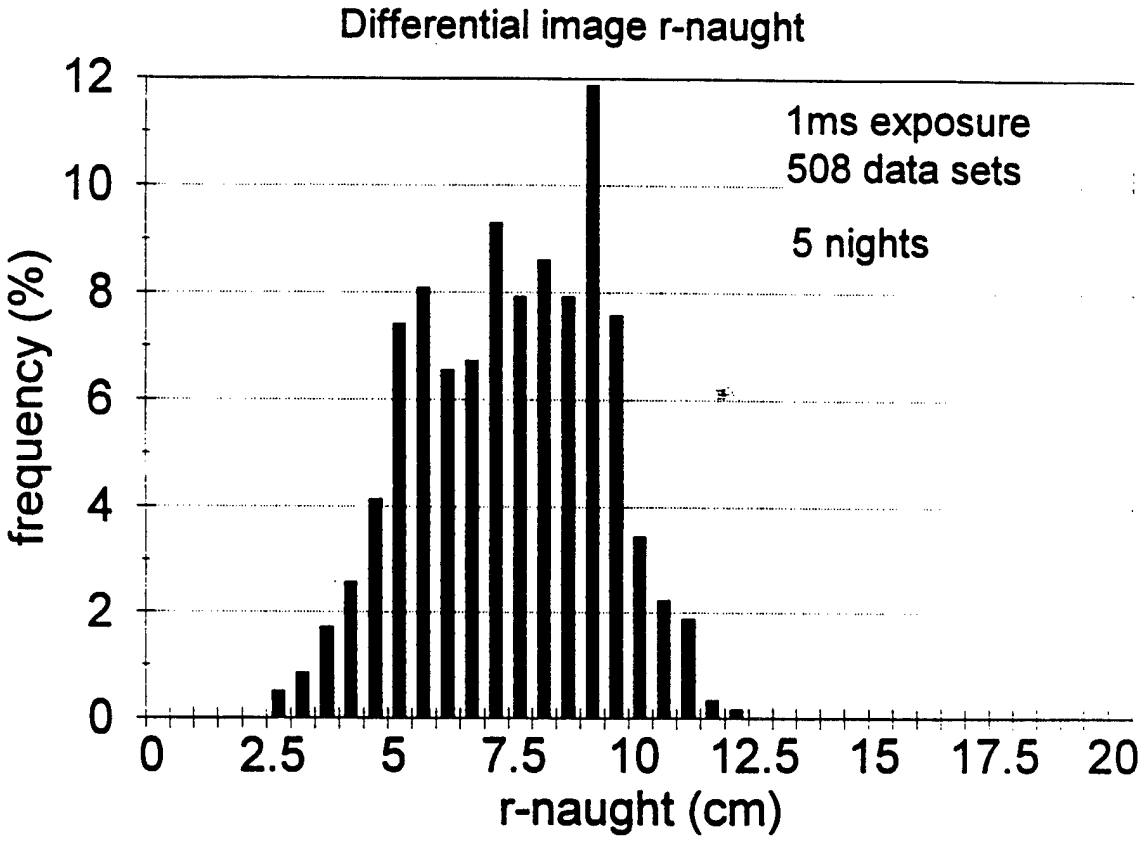

Figure 21. Frequency distribution for r_o for Aug 95 at APO.

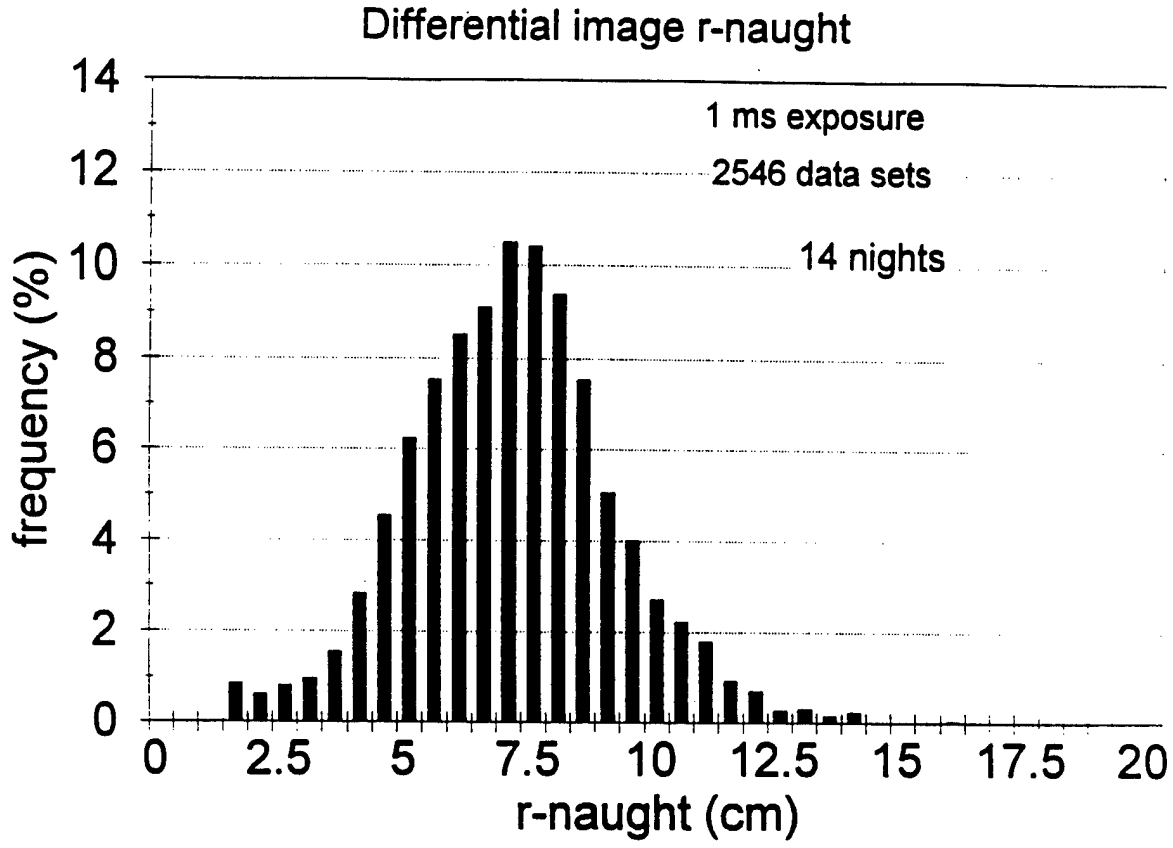

Figure 22. Frequency distribution for r_0 for Sept 95 at APO.

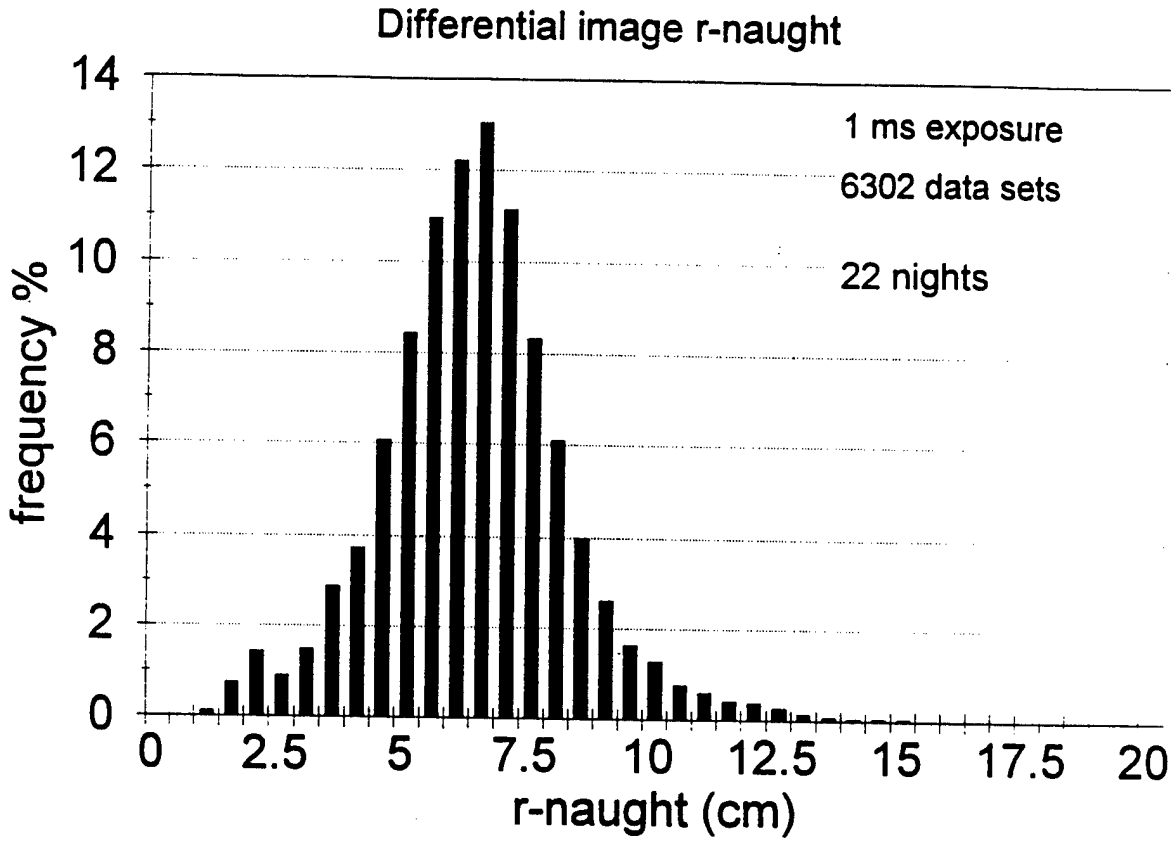

Figure 23. Frequency distribution for r_0 for Oct 95 at APO.

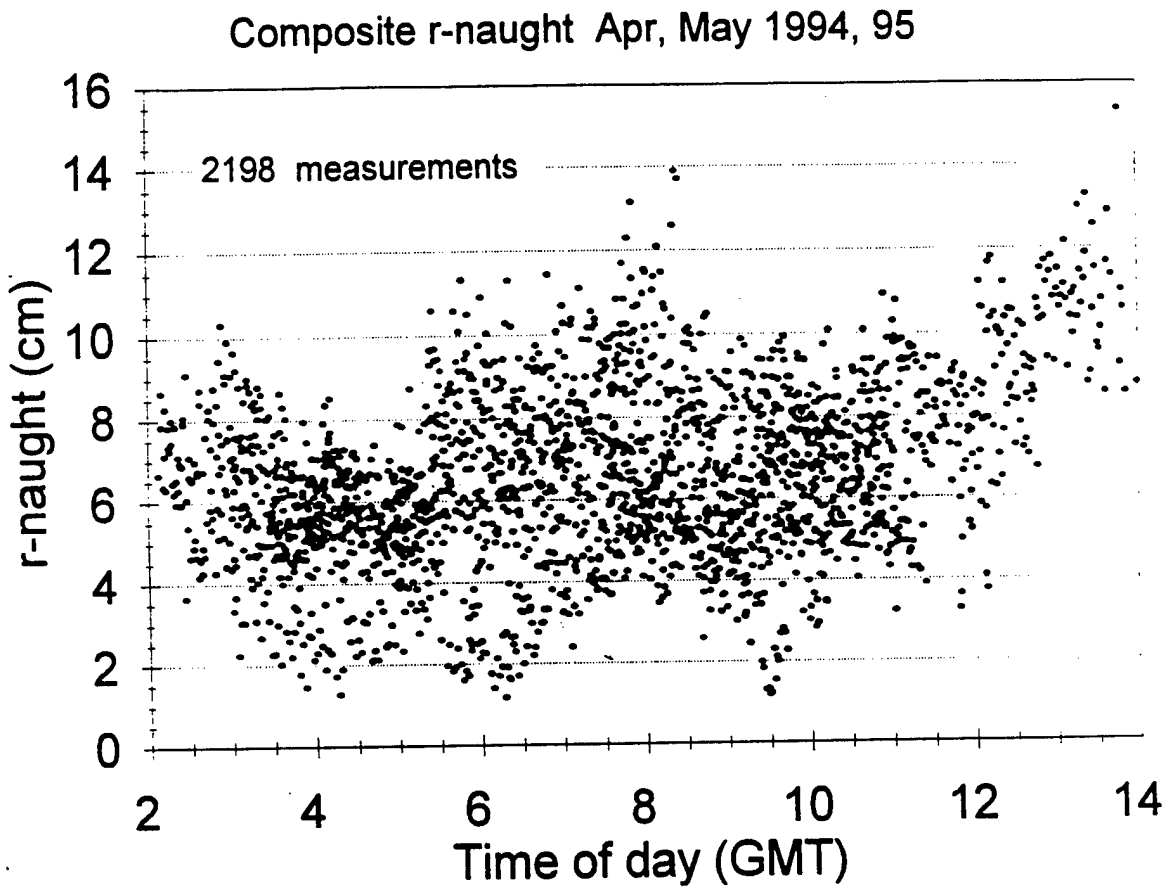

Figure 24. Composite plot of r_0 measurements for Apr and May 94 and 95 at APO.

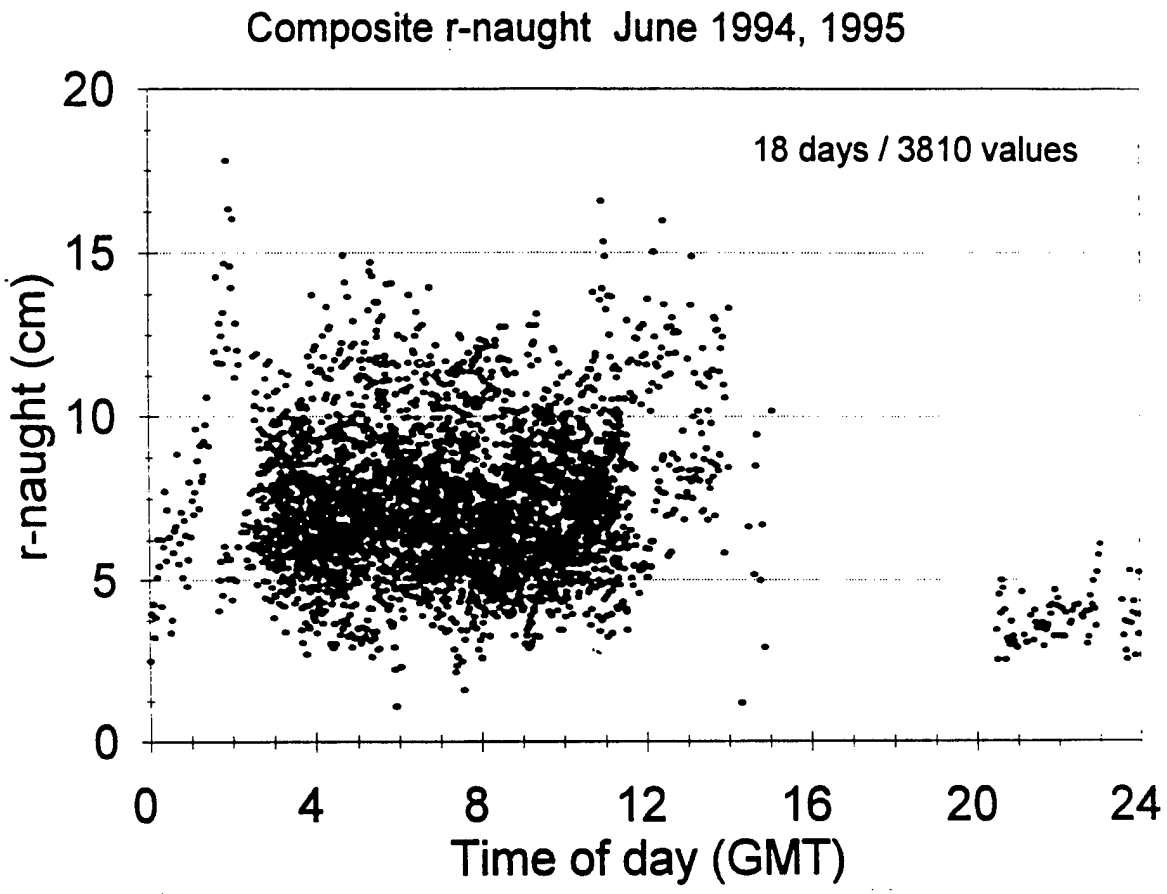

Figure 25. Diurnal composite plot of r_0 measurements for Jun 94 and 95 at APO.

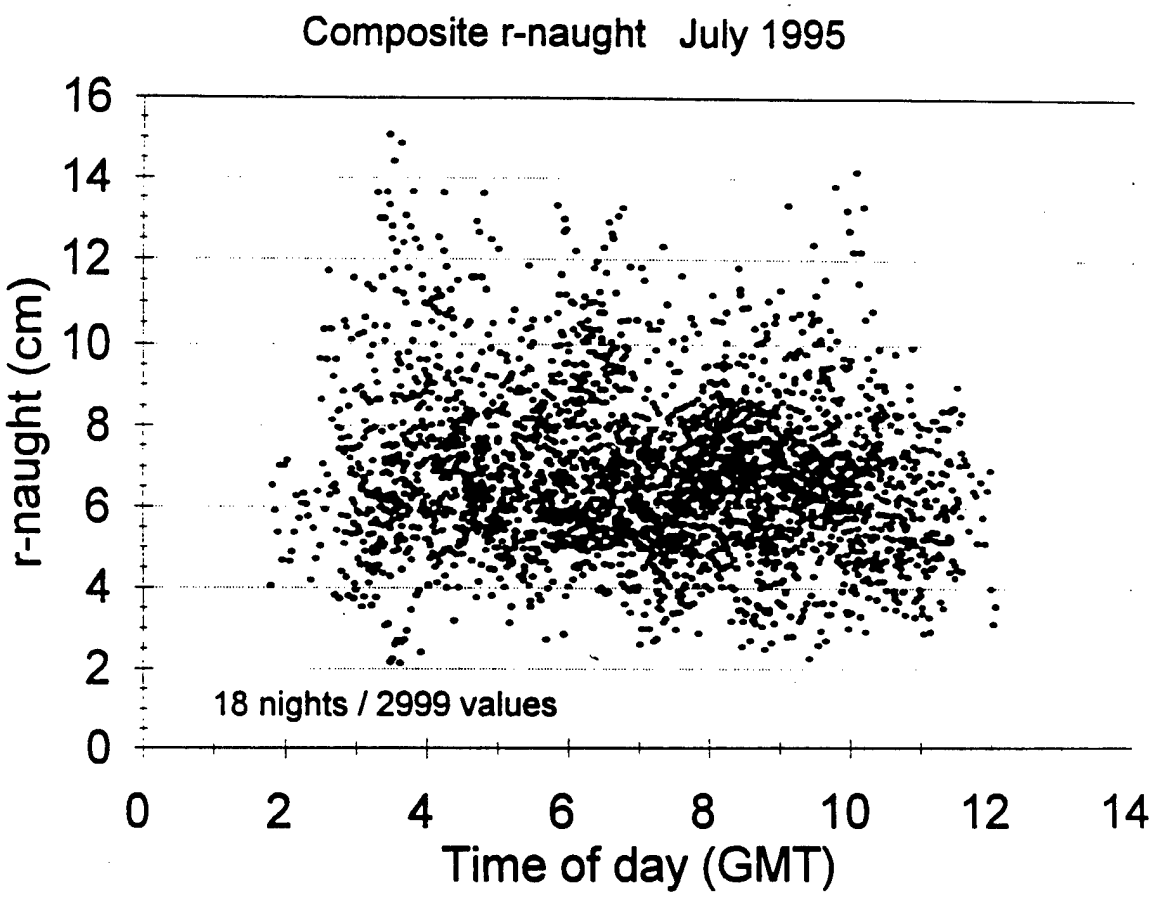

Figure 26. Composite plot of r_o measurements for Jul 95 at APO.

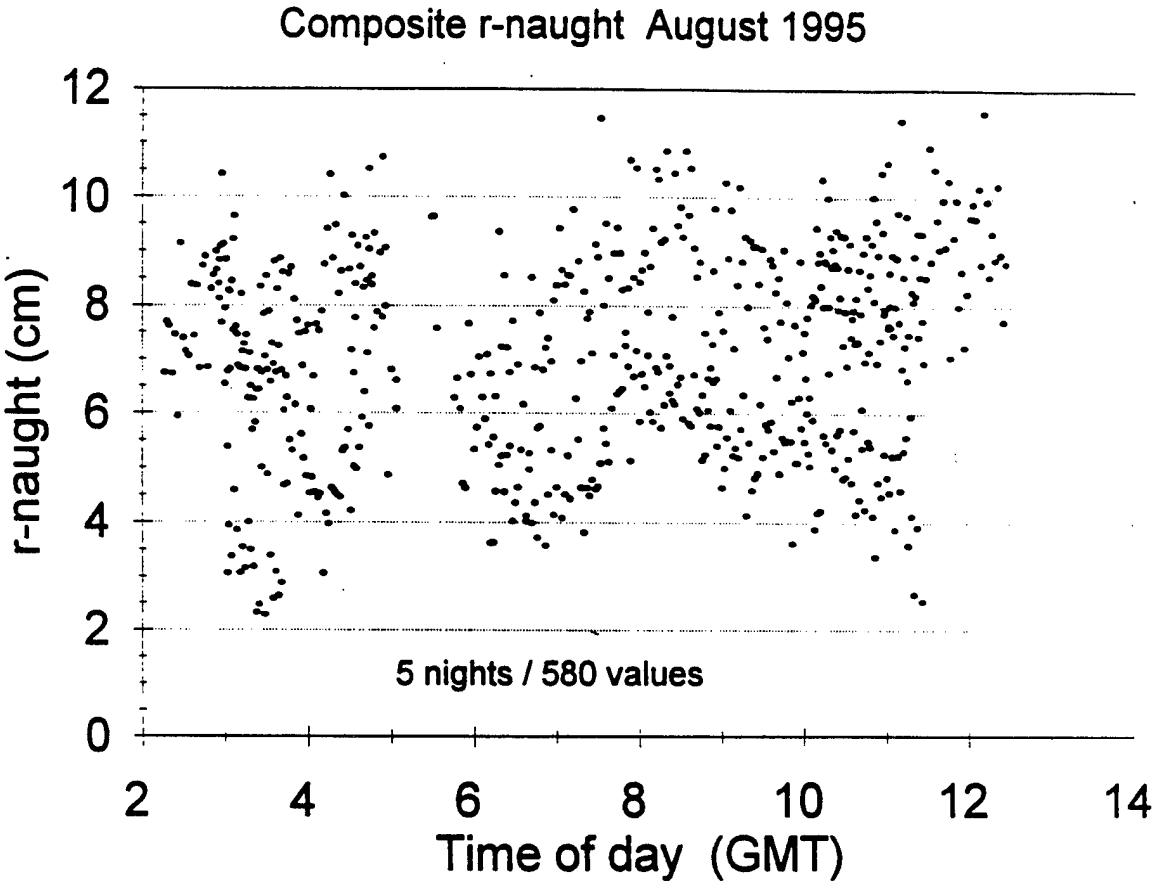

Figure 27. Composite plot of r_0 measurements for Aug 95 at APO.

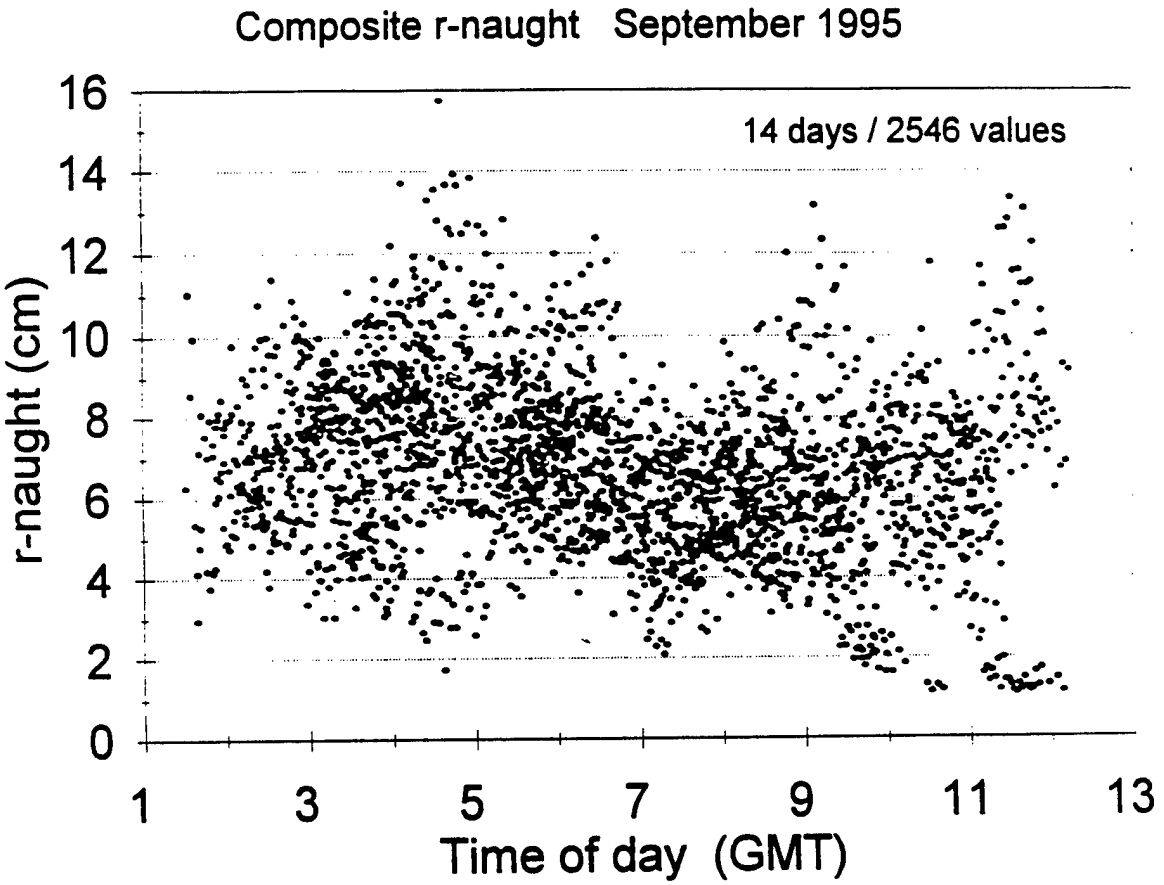

Figure 28. Composite plot of r_o measurements Sept 95 at APO.

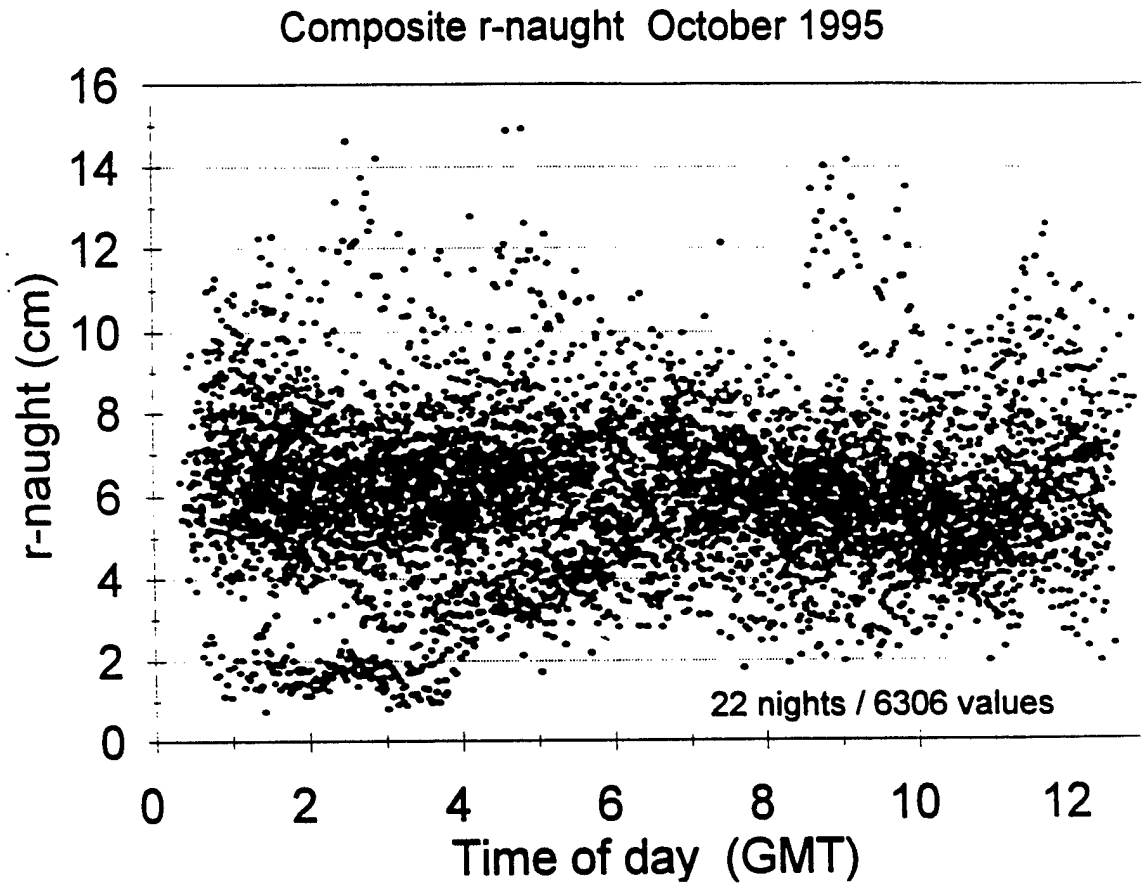

Figure 29. Composite plot of r_0 measurements for Oct 95 at APO.

4.4 Horace Mesa

Figures 30 and 31 show the r_o measurements taken at Horace Mesa with the ATMOS for 8 and 9 Nov 95. Figure 32 shows the frequency distribution of the data. While transporting the equipment to Horace Mesa, we encountered rough road. After transport, it was noticed that the focusing mechanism did not operate properly for this measurement period. A subsequent check on the average separation distances, formed by the two images, showed variations that would produce an uncertainty in the measured r_o values of approximately 10 percent from this single effect.

4.5 APRF

Figures 33 and 34 show measurements of r_o taken on 24 and 29 May 91. The 29 May values are unusually low. Figure 35 shows a few hours of r_o measurements also taken on 4 Jun 91. Figure 36 shows results from measurements taken at various times throughout a 24-h period on 18 Jun 91. The evening neutral event shows enhanced seeing conditions. Figures 37 and 38 show frequency distributions of the 2021 samples taken during May and Jun 91, separated into day and night. The overall pattern is very broad for the daylight values and narrower during night.

Figure 39 shows a 24-h (midnight to midnight local time) time series of r_o values calculated from a differential image motion variance measured on 8 Oct 91 with the ATMOS. Variances were calculated from the centroids of the differential images for 1-min periods and stepped every 15 s for recalculations and plotting. Frame rates were typically 20 fps and exposure times were 2 ms, except for a period during the afternoon when background radiation was excessive due to viewing a star near the sun. Exposure times were increased to 7 ms. The greatest variability of image motion variance and r_o occur from midmorning to evening, while night values show slowing and varying patterns with less short-term fluctuations. Figures 40 and 41 show frequency distributions of daylight and night. A daytime broadening of the pattern is seen.

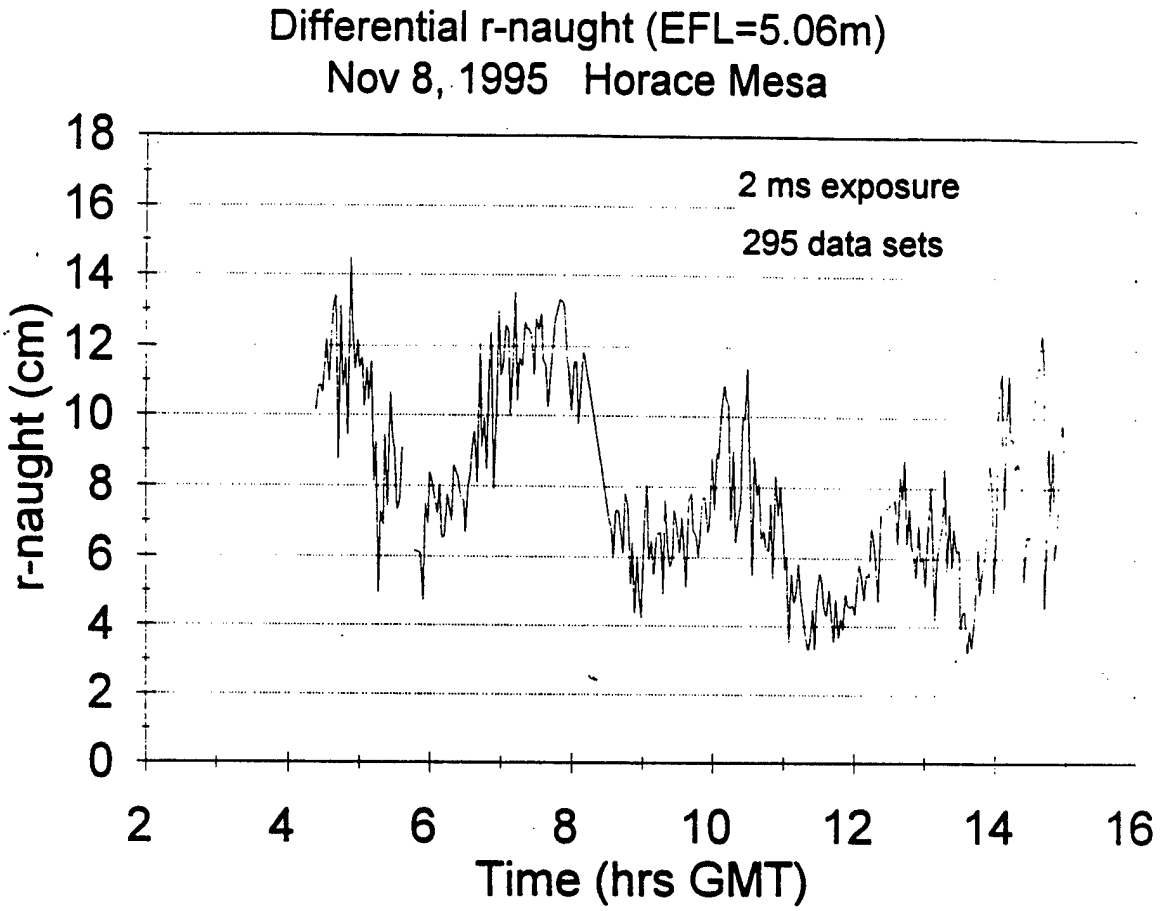

Figure 30. Measurements of r_0 taken on 8 Nov 95 at Horace Mesa.

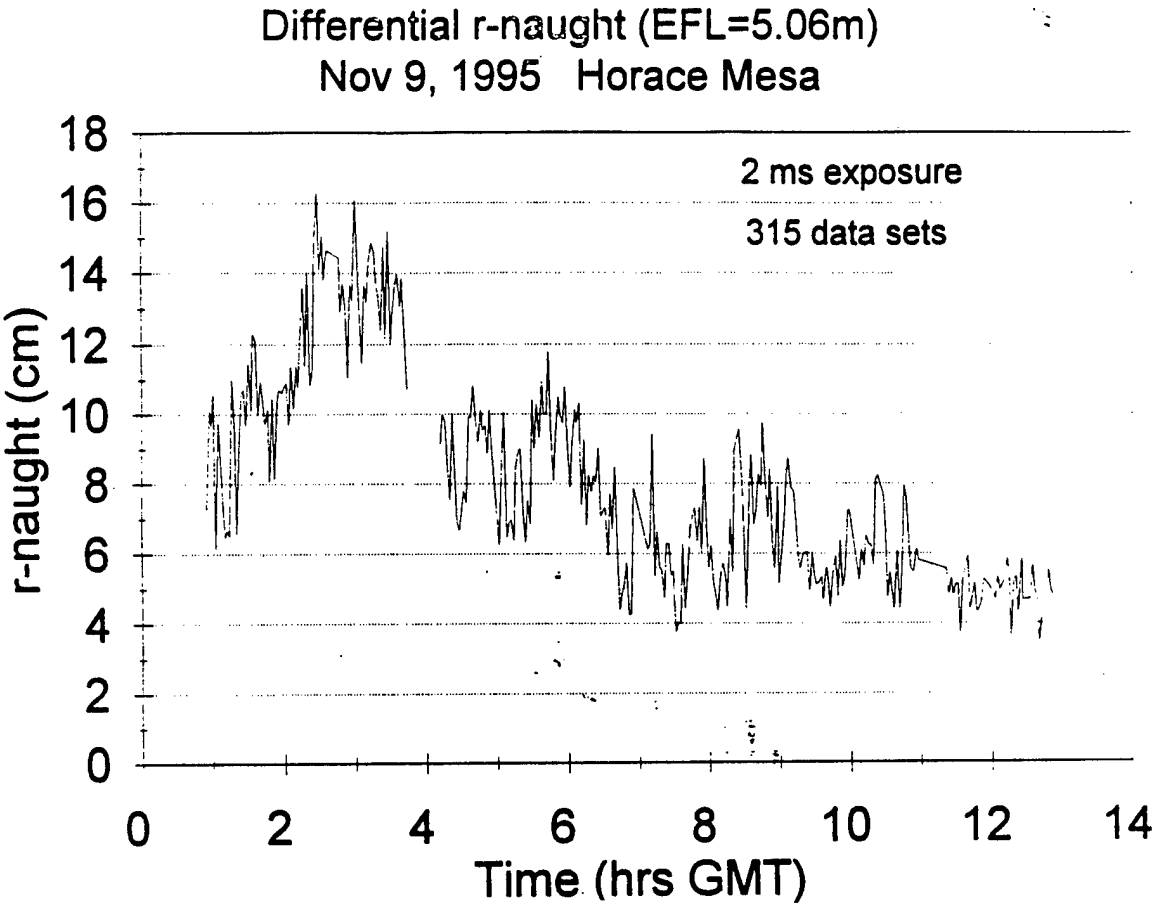

Figure 31. Measurements of r_0 taken on 9 Nov 95 at Horace Mesa.

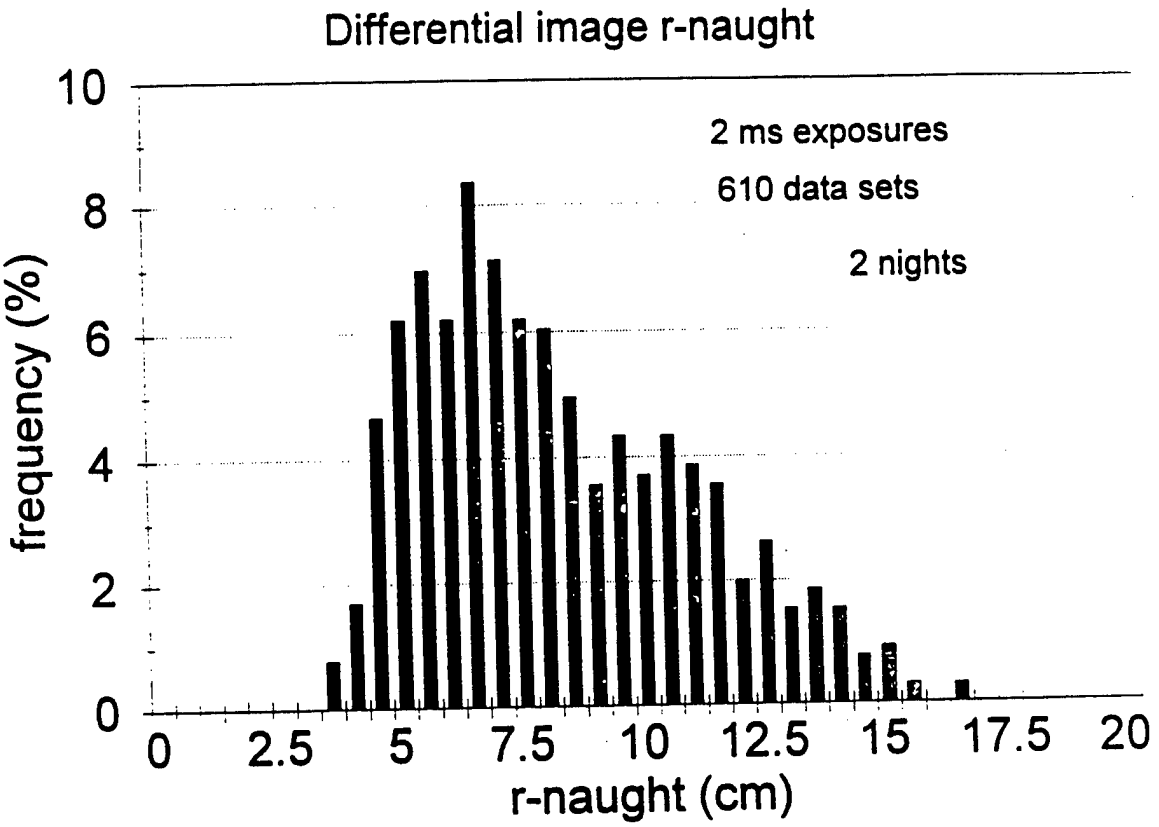

Figure 32. Distribution of the measurements of r_o taken on 8 and 9 Nov 95 at Horace Mesa.

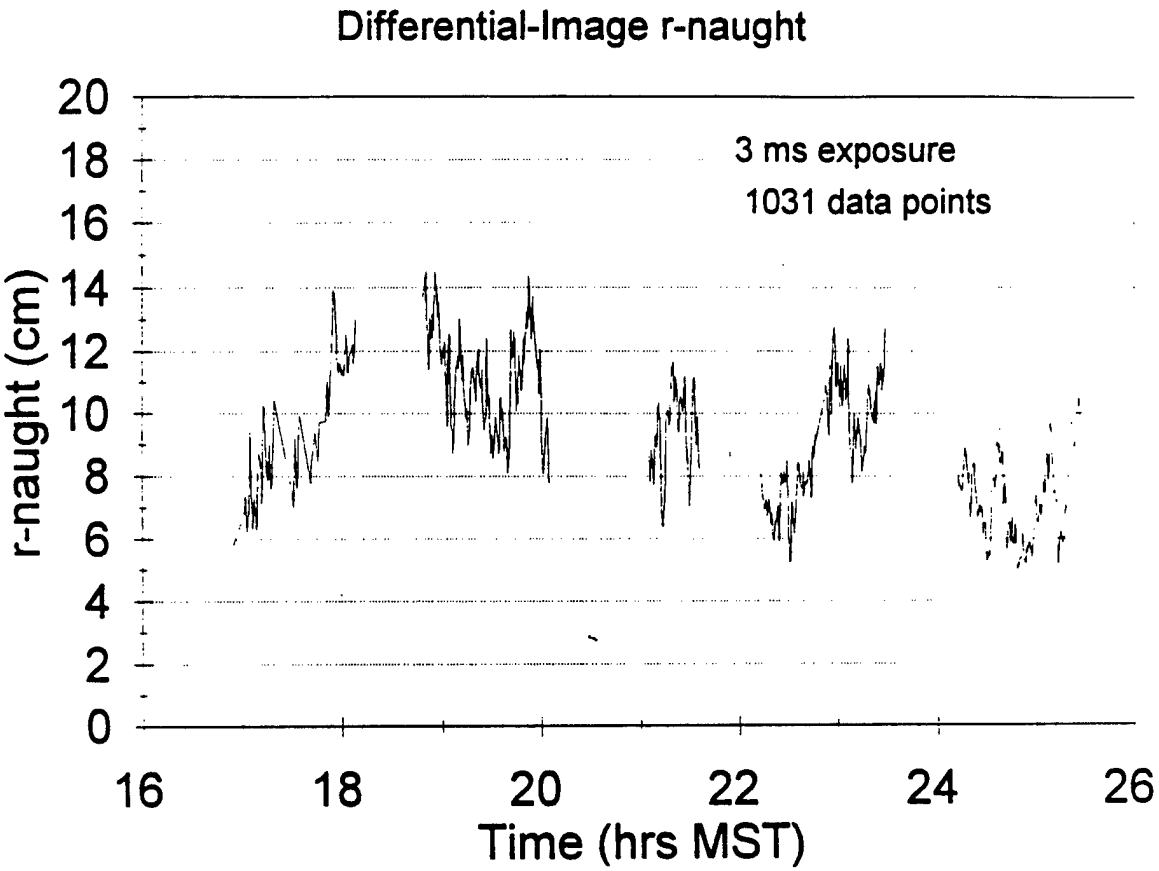

Figure 33. Measurements of r_0 taken on 24 May 91 at the APRF.

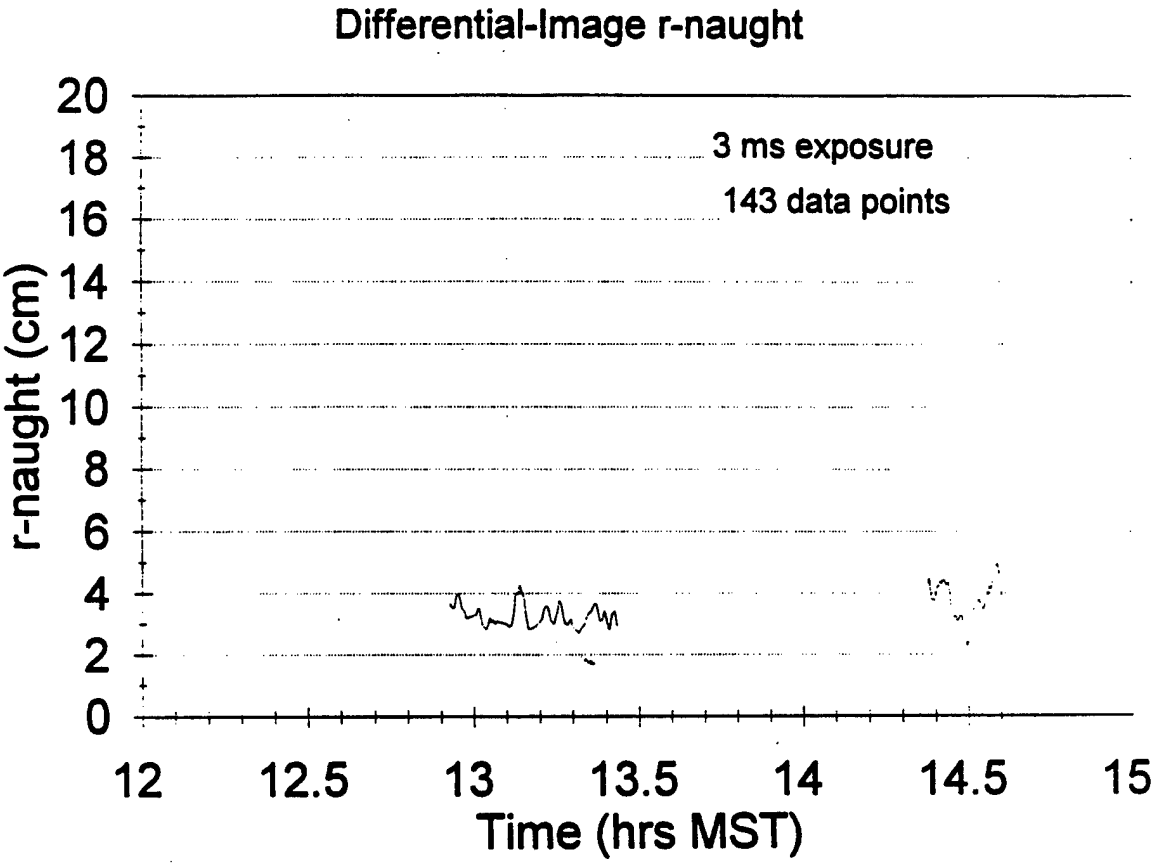

Figure 34. Measurements of r_o taken on 29 May 91 at the APRF.

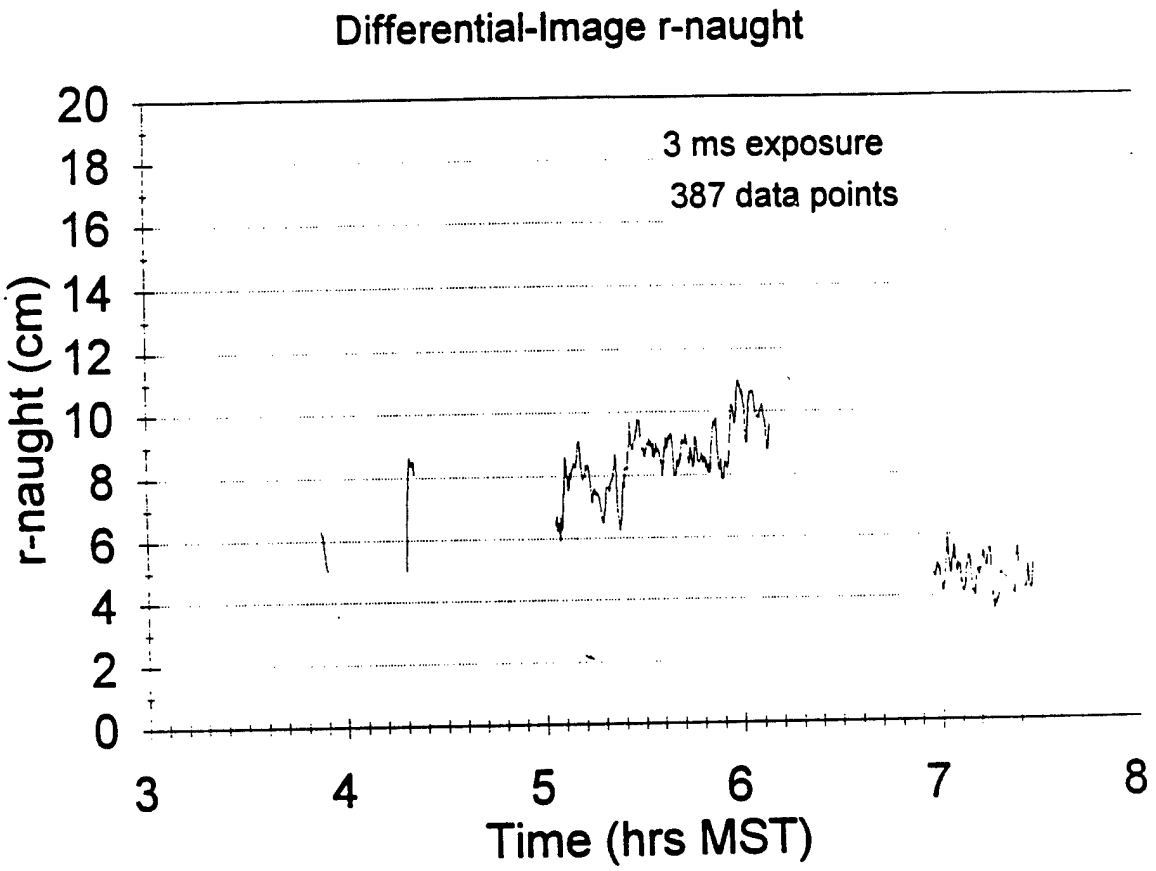

Figure 35. Measurements of r_0 taken on 4 Jun 91 at the APRF.

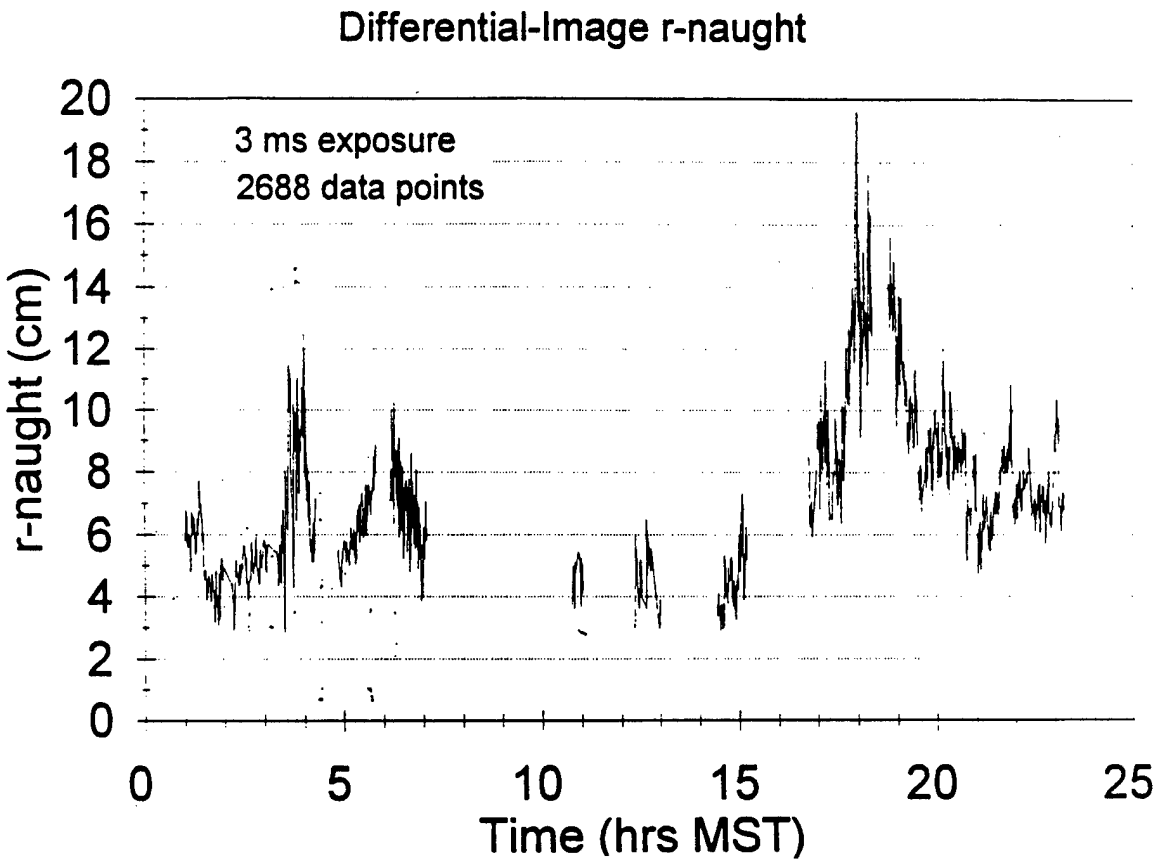

Figure 36. Measurements of r_o taken on 18 Jun 91 at the APRF.

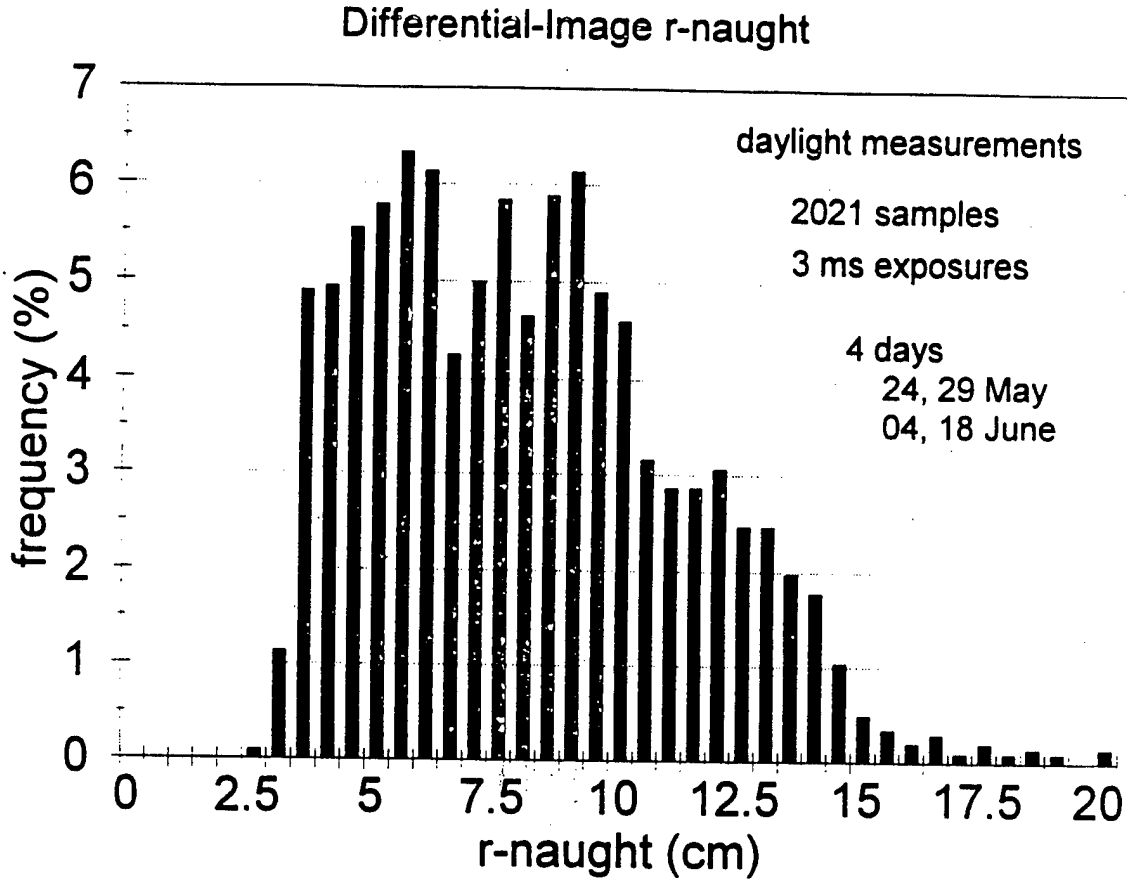

Figure 37. Frequency distribution of day measurements of r_o taken at the APRF during May and Jun 91.

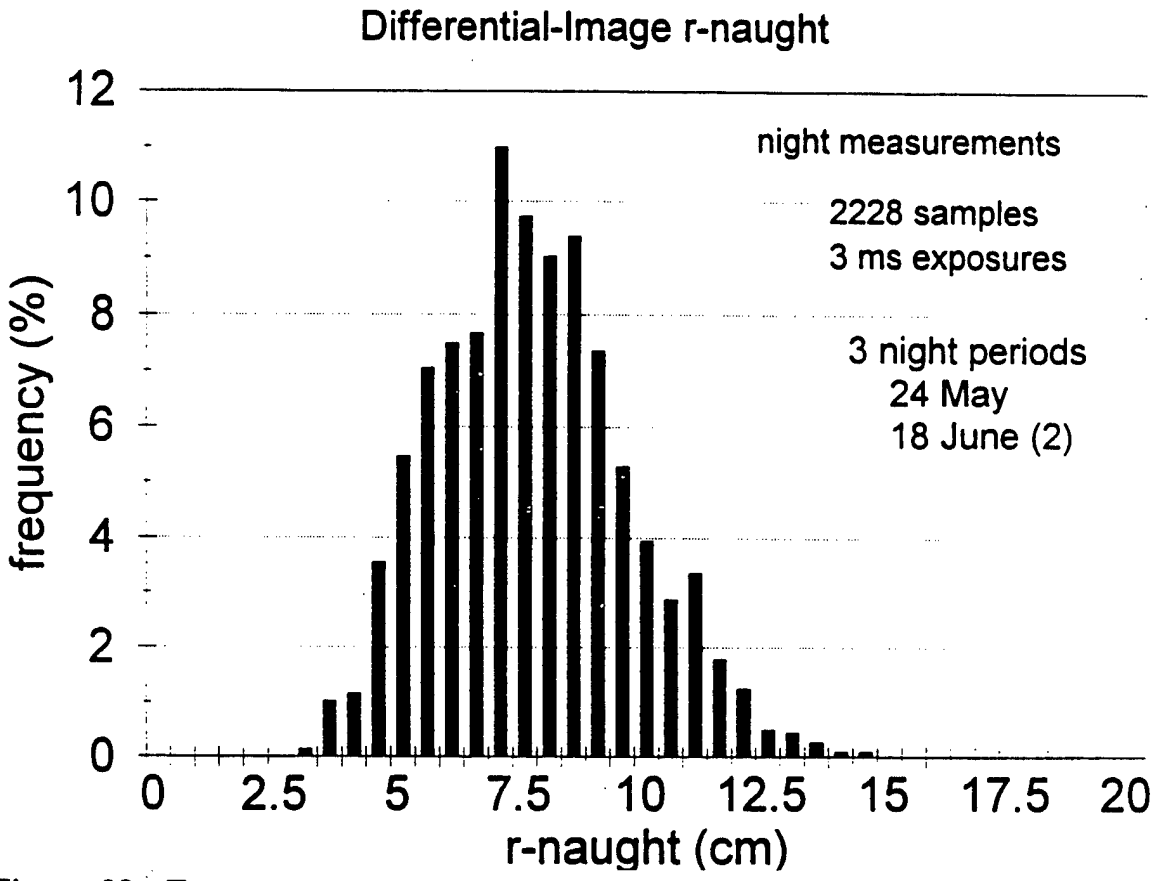

Figure 38. Frequency distribution of night measurements of r_o taken at the APRF during May and Jun 91.

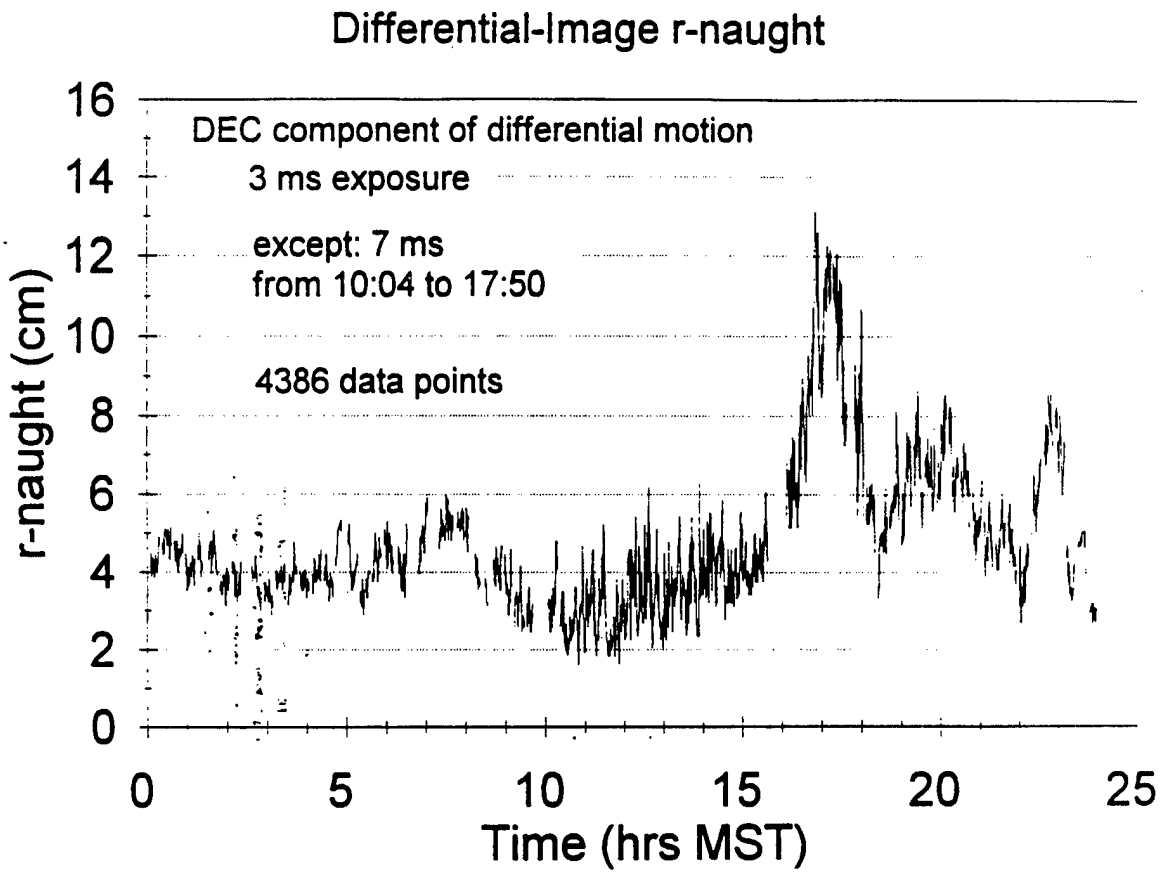

Figure 39. A continuous 24-h period of r_o measurements taken at the APRF on 8 Oct 91.

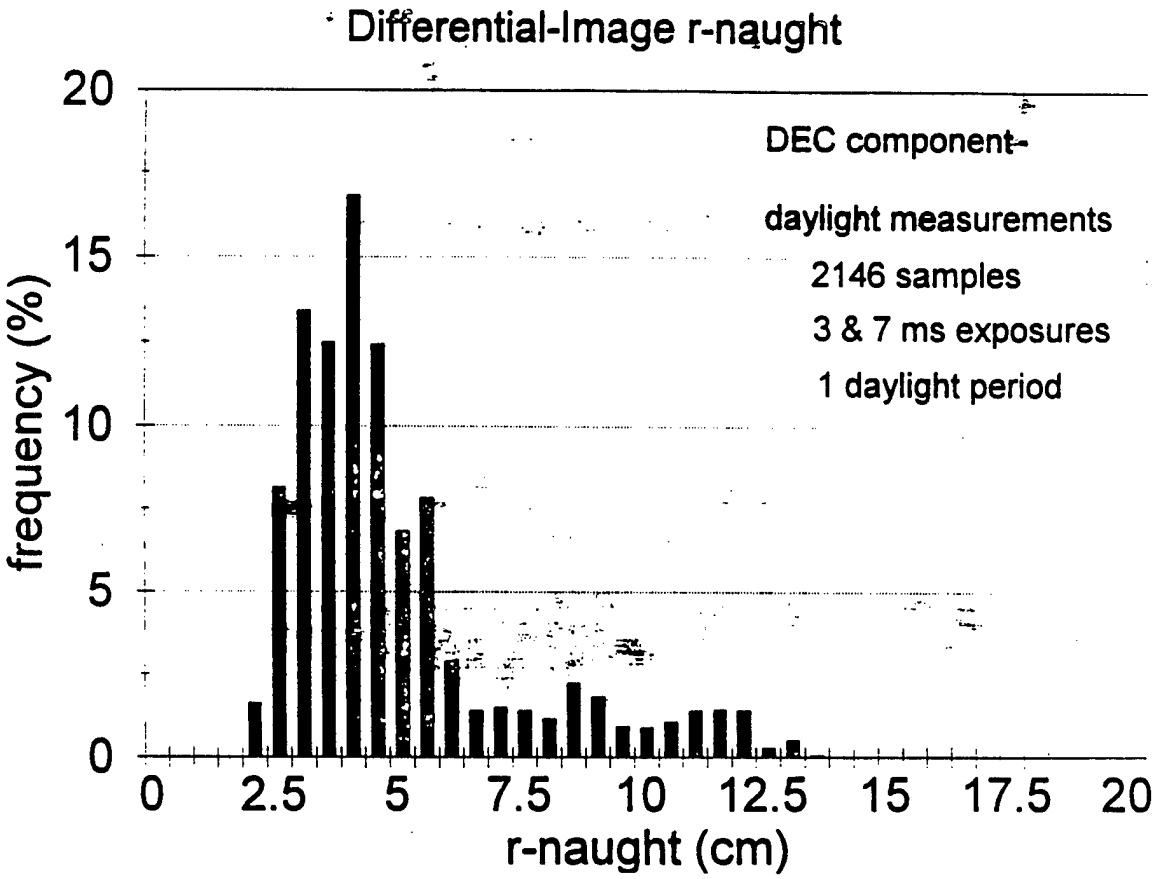

Figure 40. Frequency distribution of r_o measurements taken during daylight on 8 Oct 91.

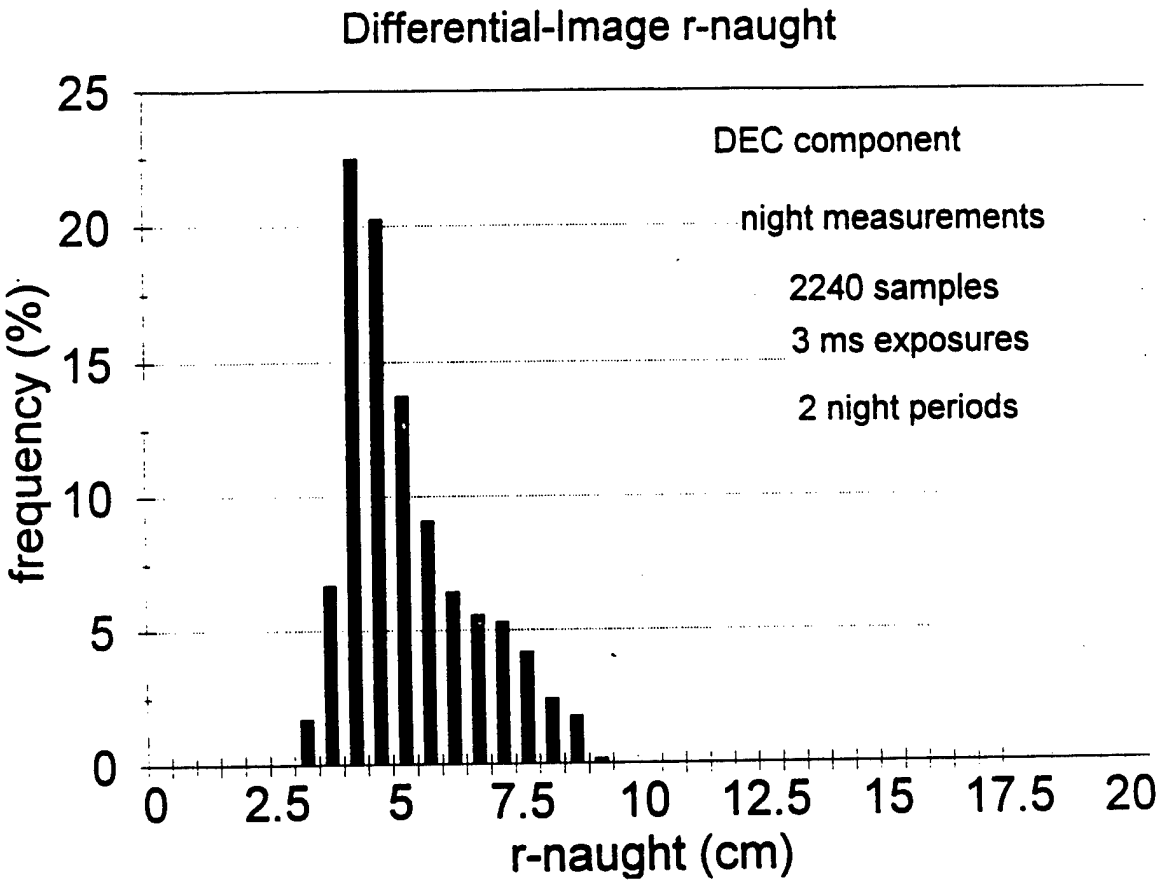

Figure 41. Frequency distribution of r_o measurements taken during the night of 8 Oct 91.

Poorest seeing conditions occur during midday when image motion is the greatest. Because r_o is inversely related to integrated C_n^2 profiles by the 3/5 power as seen in equation (1), the C_n^2 measurements taken with long-range scintillometers at 4 and 20 m AGL, shown in figure 42, confirm the diurnal pattern of r_o (and image motion variance). A complete description of the scintillometer design and theoretical background are found in Ochs et al (1980). The daily variation of C_n^2, seen in figure 42, is a typical pattern found near the surface. C_n^2 closely follows the surface radiation balance during the day and peaks during midday when net radiation reaches the maximum. The sensible heat flux, a component of the surface heat exchange, also generally follows the radiation balance daily pattern. Wyngaard, Izumi, and Collins (1971) and Kaimal et al. (1976) examined relationships between heat flux and the temperature structure parameter C_T^2 with particular emphasis on height dependency.

Two minima periods, identified as neutral events and occurring shortly after sunrise and before sunset, are seen in figure 42 for both measured heights. The minima periods correspond to times that the temperature lapse rate is moist adiabatic, the absolute value of the heat flux reaches a minimum, and temperature inhomogeneities required for production of C_n^2 are at a near surface daily minimum. During the night the variations in C_n^2 often are quite large. The scintillometer-derived data show greater variability from 1800 to 2400 MST than from 0000 to 0700 MST, agreeing with the variability of r_o seen in figure 39.

Figures 43 and 44 show 1-h plots of the measured differential image motion variance and r_o for three time periods; 1100 to 1200, 1630 to 1730, and 2000 to 2100 MST. The variances range for the midday hours from about 11 to 77 μrad^2. The corresponding r_o values range from slightly less than 2 cm to over 4 cm. Strong surface convection is responsible for the rapid and pronounced variations. The lowest overall differential image motion variances (and highest r_o values) are found during the evening neutral event (1630 to 1730 MST). Values of r_o often exceed 10 cm with a short time period where r_o is slightly above 12 cm. The overall patterns of differential image motion and r_o for the night measurements (2000 to 2100 MST) lack the sharp changes as seen during the day. The differential image motion and r_o results generally lie between the

midday and evening neutral events with the exception of a few midday data points, presumably during subsidence conditions, where the midday r_o values can exceed the lower night values.

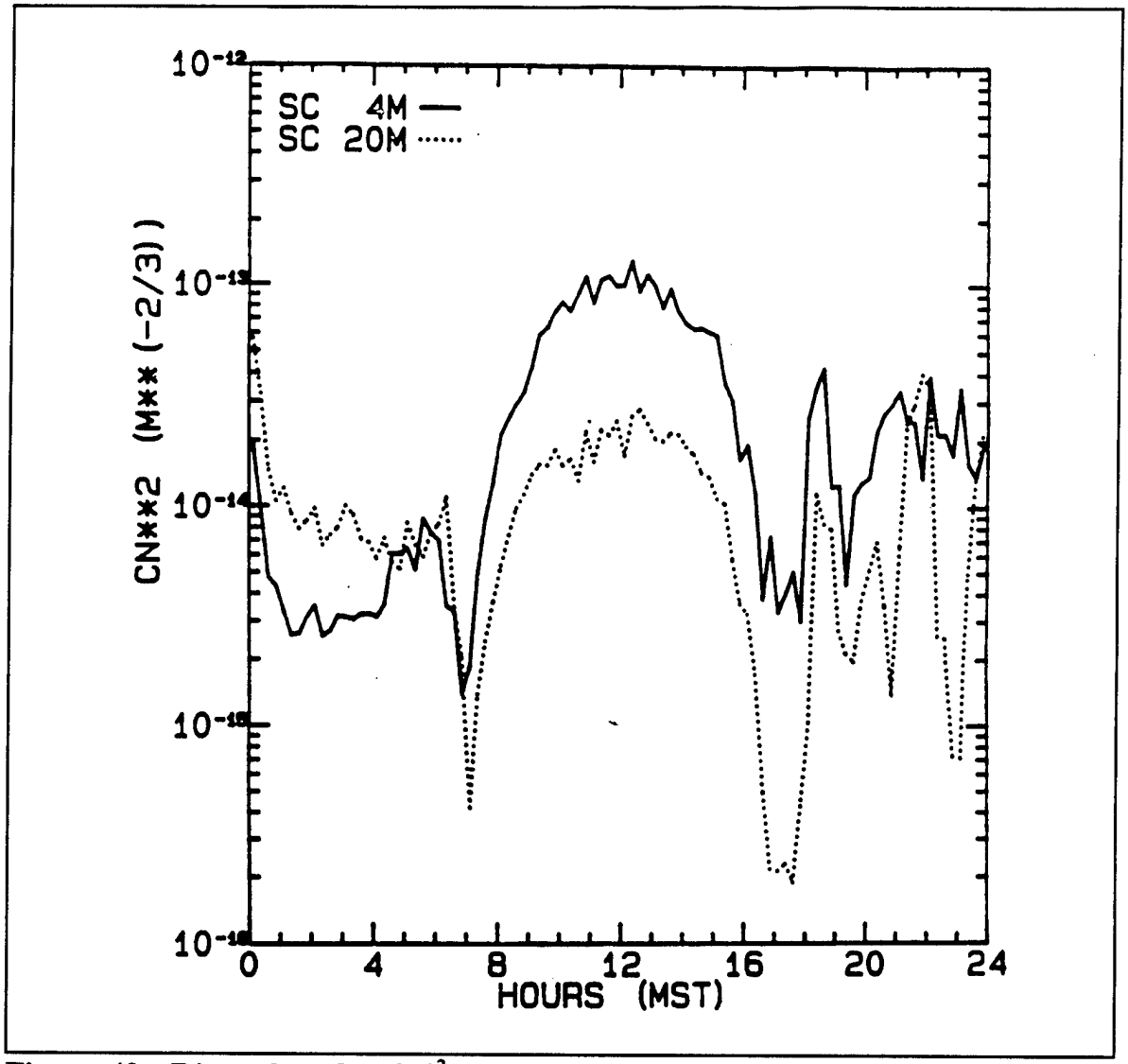

Figure 42. Diurnal cycle of C_n^2 measured with scintillometers mounted 4 and 20 m AGL at the APRF.

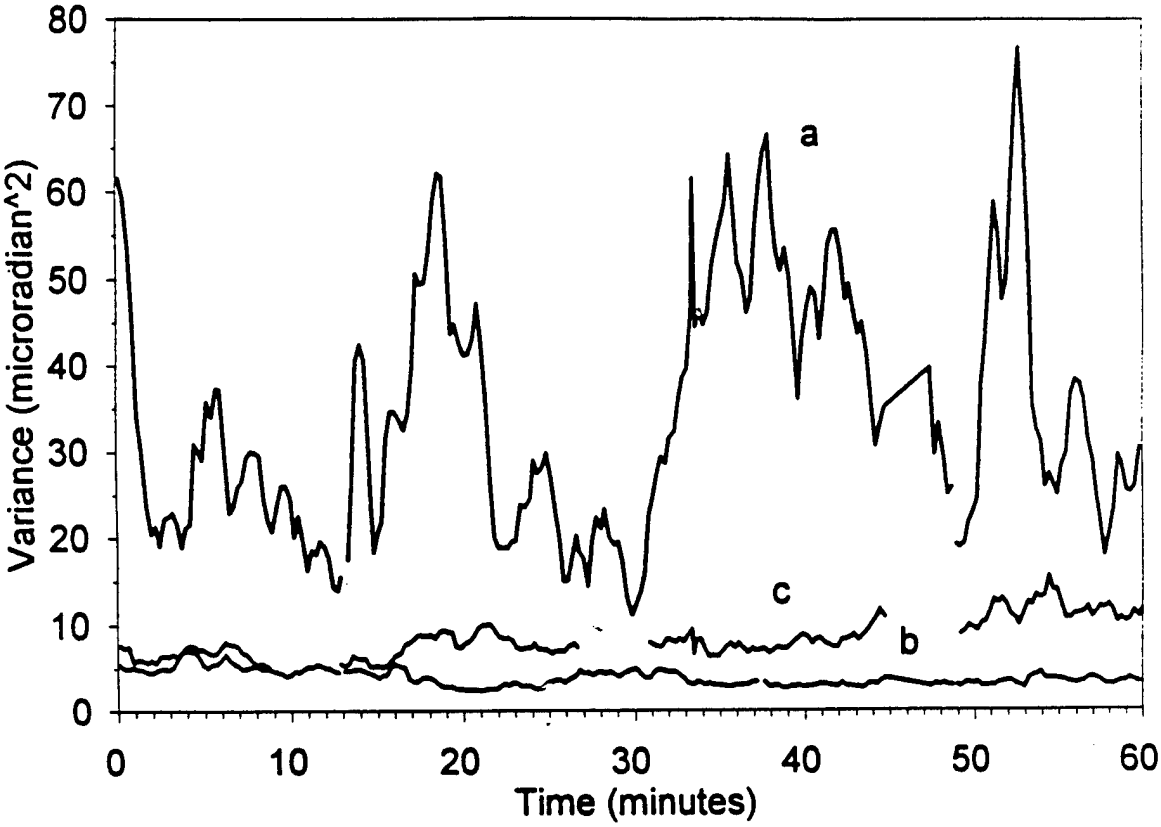

Figure 43. Differential image motion variances for three 1-h periods during the day: a) 1100 to 1200 MST, b) 1630 to 1730 MST, and c) 2000 to 2100 MST.

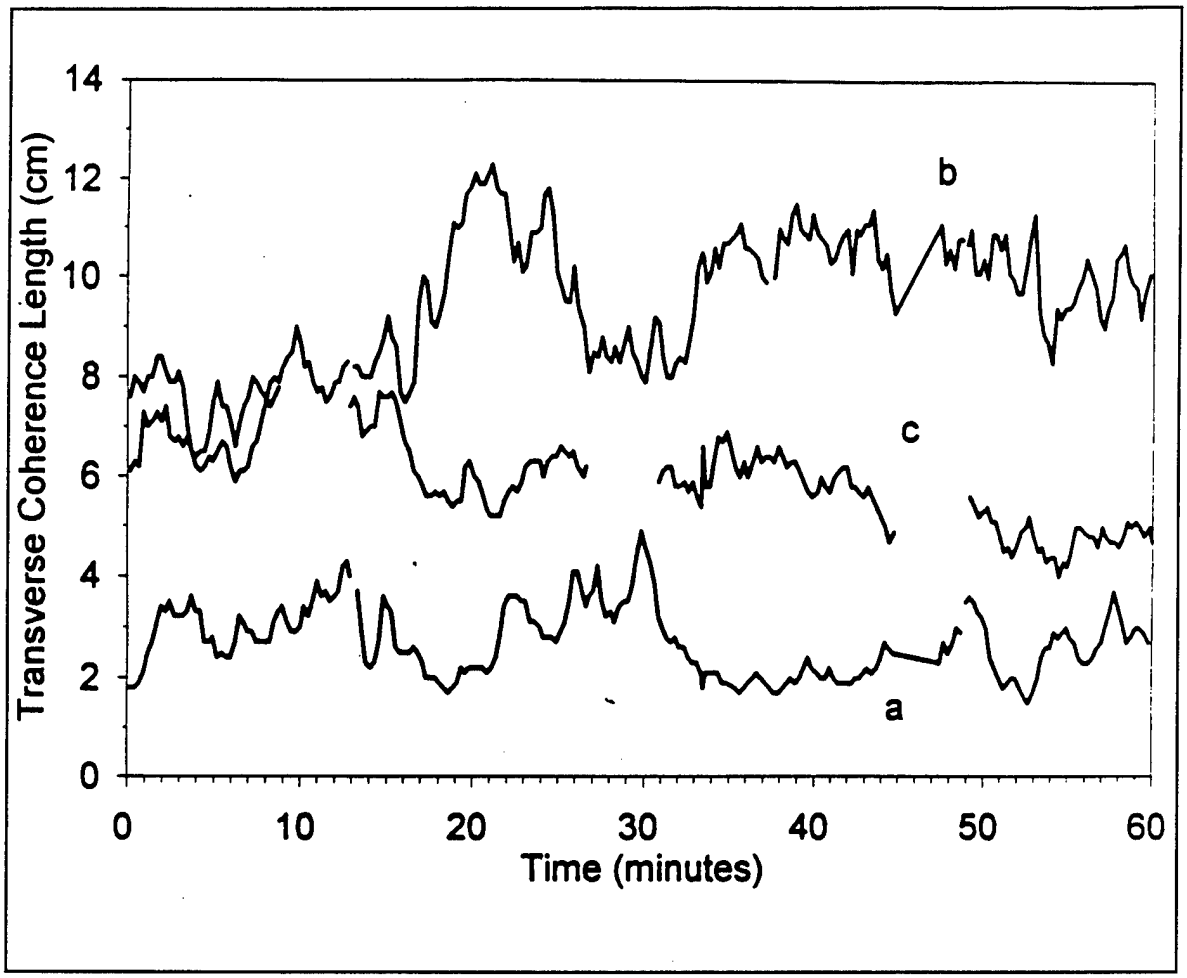

Figure 44. r_0 calculations using the image motion results in figure 43.

Atmospheric measurements were taken at various WSMR locations for characterization of optical sites from 1983 to 1990. The data, including r_0 results, are summarized by season (Grace et al., 1990). The r_0 measurements generally were taken at 5-min intervals; therefore, short term variability effects could not be studied. Some of the results were stratified as to fractional cloud cover. (Eaton et al. 1985). The averaged or climatological r_0 results agreed with the 8 Oct 91 results; they consistently showed the best seeing during neutral events (particularly the evening neutral event). The poorest average seeing results were during midday, and nighttime r_0 values showed high variability. Differences in r_0 were also small season-to-season.

Figure 45 shows a 24-h time-height display of the sodar echo measurements for 8 Oct 91 from 19 to 276 m AGL. Grey scales show 1-min averages of the backscattered power from the vertical beam antenna with white being the strongest and black the weakest returns. From 0000 to 0600 MST, there is a nocturnal inversion layer that increased in altitude from about 25 to 150 m. Wave activity is seen associated with the top of the stable layer. Formation of the elevated inversions depends on surface radiative cooling (Garrett and Brost 1981), turbulent heat-flux (Brost and Wyngaard 1978), and advective effects (Hootman and Blumen 1983). The nocturnal boundary layer at the APRF typically is formed by radiative cooling coupled with drainage flows and pooling of cold air from the surrounding mountains. The development of convection, associated upward movement of the capping inversion, and erosion of the stable air aloft are seen from near 0700 to 0930 MST. Well-developed thermal plumes, originating at the surface under superadiabatic conditions, are observed from about 0930 to after 1500 MST. The decreasing returns in height suggest a decreasing temperature gradient within each plume. The C_T^2 values decrease with height because a plume entrains surrounding air with low C_T^2 values into the plume as it rises. Subsiding air is commonly found in the volume between plumes. As the ground temperature declined toward evening, the thermal plume activity rapidly disappears.

Centered near 1700 MST, and after the convective activity ceases, sodar returns are very weak, a consequence of the evening neutral event. The transition from this period to stable conditions of the nocturnal boundary layer occurred at about 1800 MST. For the next 6 h, a complicated pattern of multilayered weak and strong echoes are found. Sinusoidal oscillations in the laminated structure are internal gravity waves perturbing strata in the planetary boundary layer, as described by Hooke and Jones (1986). Several examples of clear air sodar records including waves and instabilities are shown and discussed by Neff and Coulter (1986). Gossard and Hooke (1975) show several cases of night wave structures sensed by sodars in the boundary layer, similar to those shown in figure 45. Gossard and Hooke (1975) also define conditions supporting gravity waves in the stable boundary layer and describe some rigorous mathematical solutions of the phenomena.

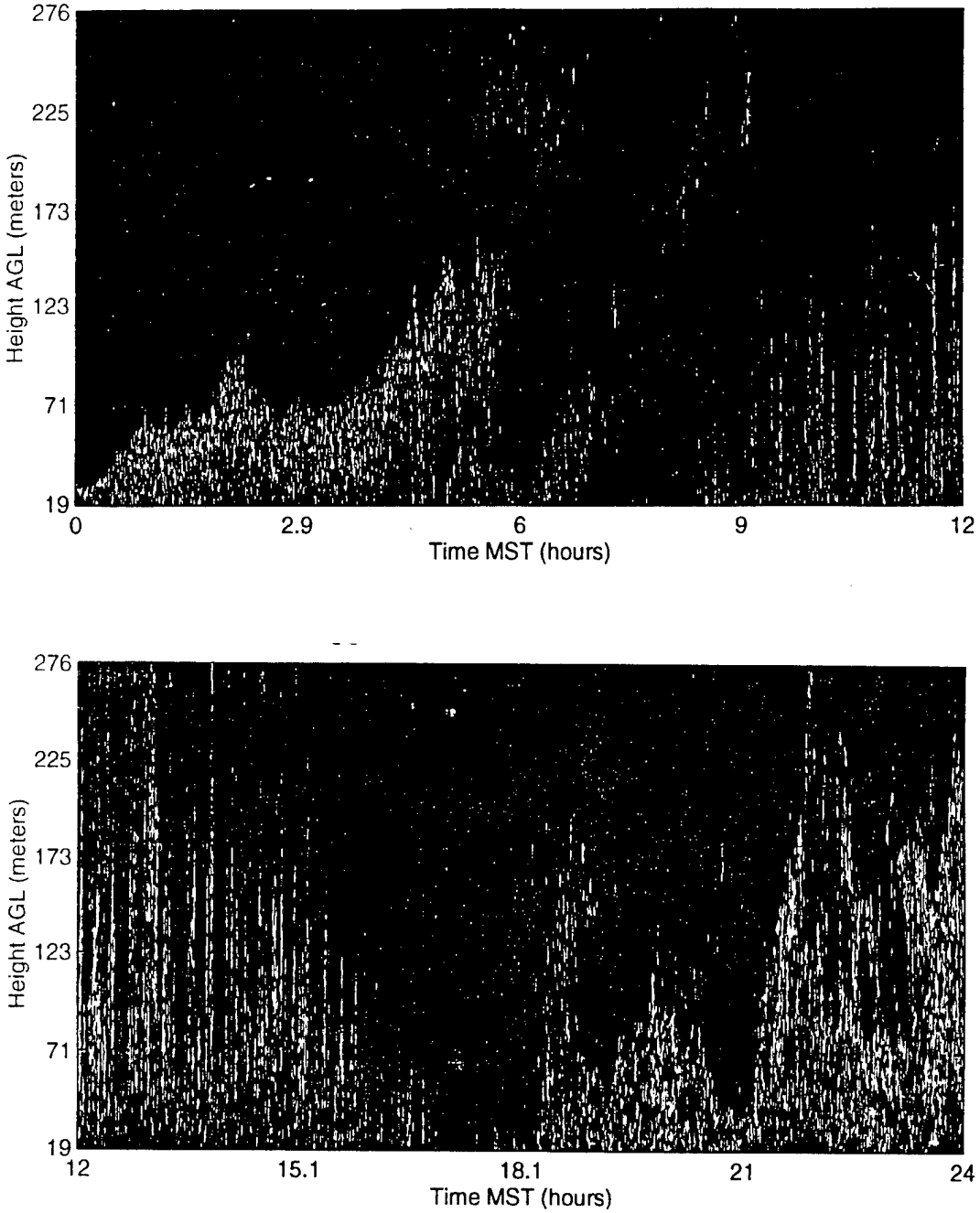

Figure 45. Time-height display of 1-min backscattered power sensed on 8 Oct 91. Backscatter is ordered as in a rainbow with red being the strongest return and dark blue being the weakest return. Black is the background strength.

Interest in gravity-wave research has increased over the past several years: waves play a key role in processes throughout the atmosphere and transport large quantities of energy and momentum in a short time. Hines (1970) shows that all the momentum in the lower boundary layer could be removed in less than 2 h by the vertical momentum flux associated with a gravity wave. A large, monochromatic wave event was documented by Van Zandt et al. (1993) at the Flatland Atmospheric Observatory, near Champaign/Urbana, IL. A surface-pressure network verified that the wave affected a wide mesoscale area. Surface winds oscillated between nearly westerly at about 5 m/s to nearly easterly at 3 m/s. Large gravity waves are also known to directly effect weather, including the development of thunderstorms and the intensification of snow lines, convection, and cyclones (Stobie, Einavdi, and Uccellini 1983; Schneider 1990; Redelsperger and Clark 1990; Uccellini and Koch 1987).

Figure 46 shows five-min C_n^2 values sensed by the sodar and averaged over the measured increment (19 to 276 m AGL) for the 24-h period of 8 Oct 91. The overall pattern has characteristics similar to those of the r_o measurements, such as a slow change in the first 3 h, a weak morning neutral event, strong midday fluctuations, a pronounced evening neutral event, and large slowly varying changes from 1800 to 2400 MST.

As shown in equation (1), the ATMOS senses the integrated, or ground-to-space, C_n^2 for determining r_o values. The scintillometer C_n^2 results are derived from volumes of atmosphere near 4 and 20 m AGL. The sodar provides profiles of C_n^2 from 19 to 276 m AGL. The scintillometer and sodar measurements do not provide ground-to-space profiles, so one-to-one comparisons with the ATMOS-derived results are not possible. However, the scintillometer and sodar provide contributions to the total C_n^2 profiles, which can be evaluated.

Linear regression analyses, using the method of least squares, was used to examine the relationships between the different turbulence-sensing instrumentation. Because r_o is inversely related by the -3/5 power to the integrated C_n^2 profile as shown in equation (1), $r_o^{5/3}$ values were used in the analyses. 15 min averages of log $r_o^{5/3}$ and log C_n^2 were used in the regression analyses. The coefficients of determination (r^2), where r is the correlation

coefficient, were calculated to determine the degrees to which the ATMOS results were associated to the results derived from the scintillometer and sodar.

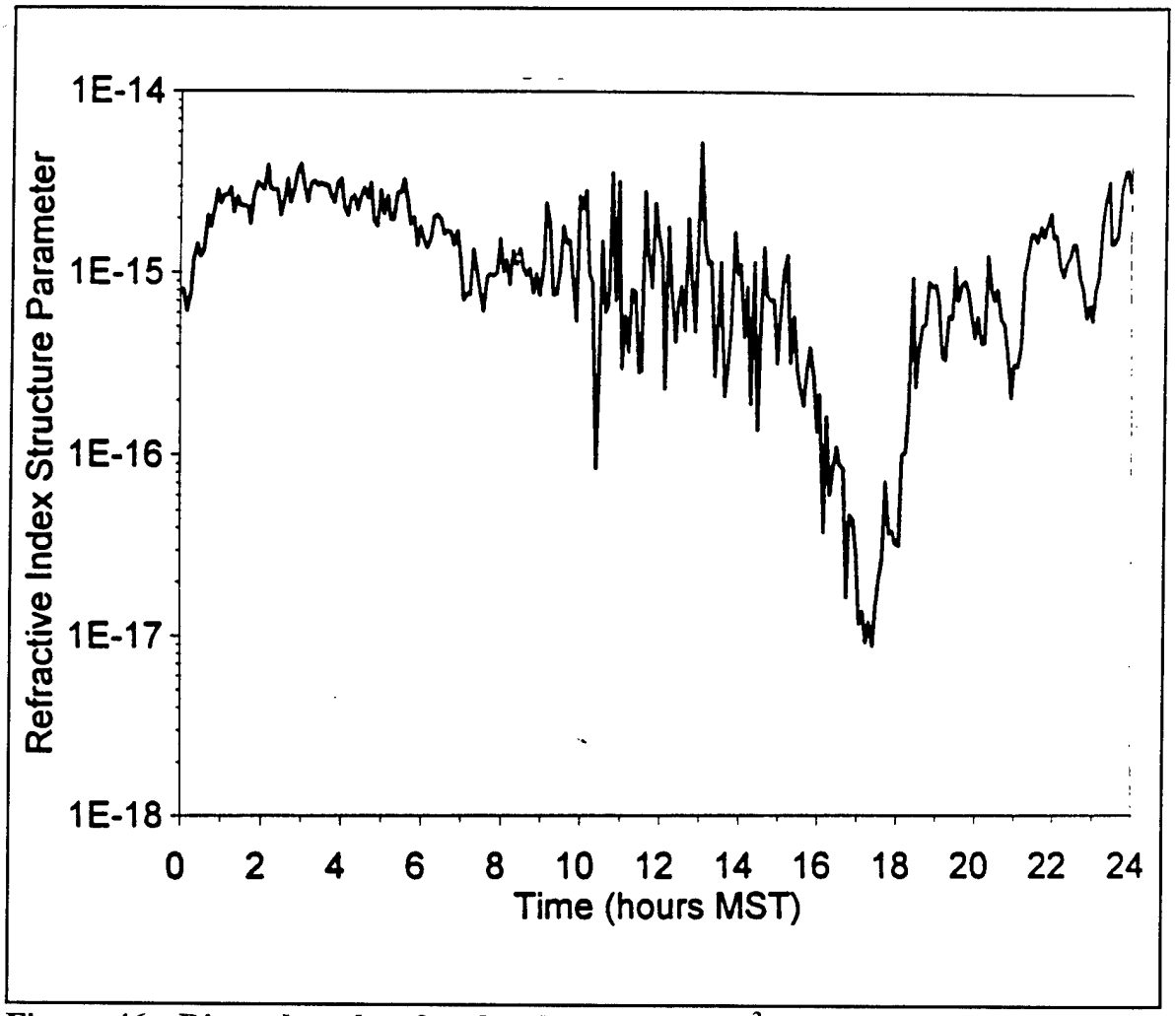

Figure 46. Diurnal cycle of sodar-derived 5-m C_n^2 averaged over the height increment 119 to 276 m.

Figure 47 displays the r^2 values derived from the ATMOS and scintillometer measurements and ATMOS and sodar measurements for the complete 24-h period. Every 5 m of the sodar C_n^2 profile was used in the analyses. The strongest correlations are seen at the lowest part of the sodar profile; slightly below 200 m AGL. To examine the differences in correlations at different times of the 24-h period, r^2 values were calculated for three separate periods: midnight to near sunrise, near sunrise to near sunset, and near sunset to midnight. Figure 48 shows that r^2 values from the ATMOS and scintillometer measurements for 0000 to 0630 MST decreased from the 24-h results. The ATMOS and sodar r^2 results also decreased except for two layers centered near 65 and 155 m AGL. The time-height sodar backscatter results (figure 45) show an elevated layer around 50 m AGL from about 0100 to 0300 MST and rose to near 150 m from 0430 to 0630 MST. Day r^2 values (figure 49) are considerably higher from 4 to 150 m (both scintillometer and sodar to ATMOS comparisons) than r^2 values shown for the 24-h period. The lower part of the convective unstable boundary layer contributes strongly to the total integrated profile. Figure 50 (near sunset to midnight) shows r^2 values from the ATMOS-scintillometer and the ATMOS-sodar comparisons at most heights to exceed the r^2 night values shown in figure 48. The effect is particularly pronounced in the bands centered at 30 and 120 m, and for all heights above 190 m. The complex structures shown by the clear-air returns in figure 7 are producing contributions to the r_o patterns sensed by the ATMOS.

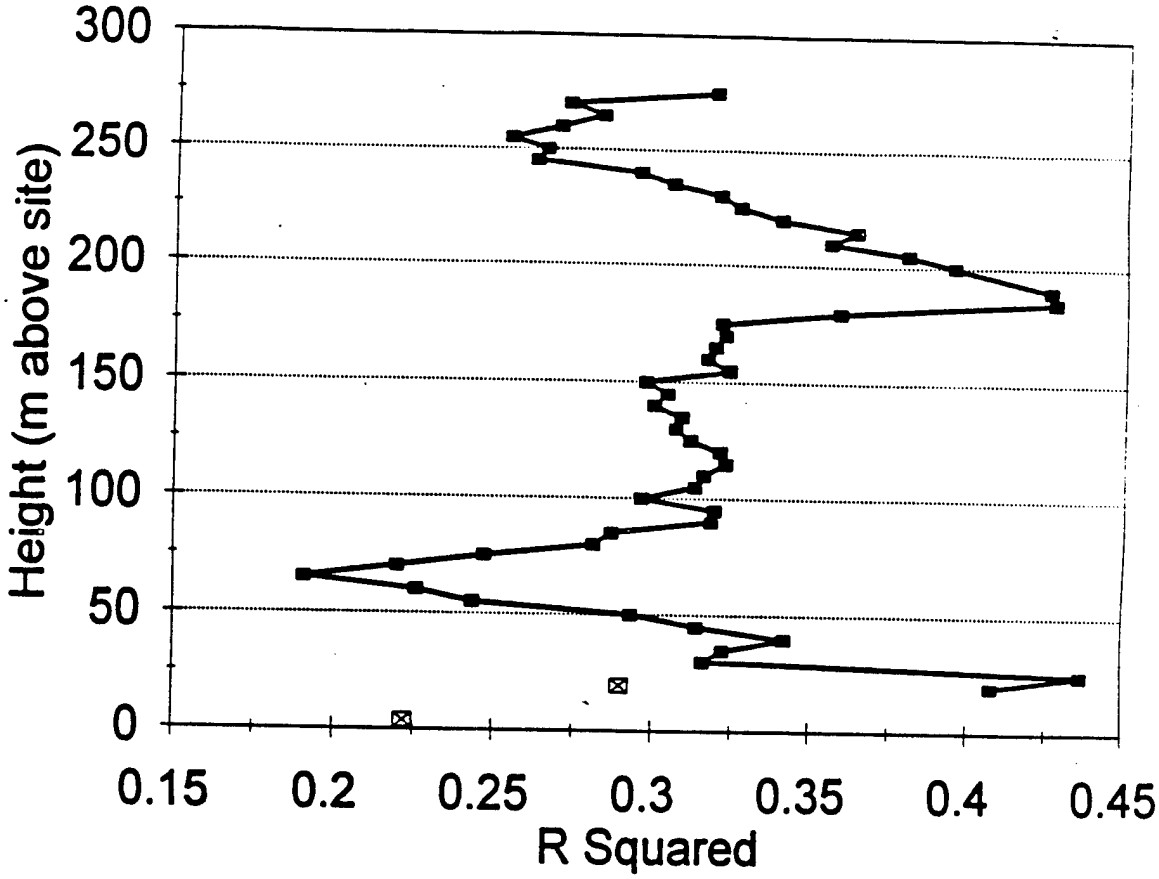

Figure 47. Coefficient of determination values (r^2) calculated for the ATMOS and scintillometer results (C_n^2) and the ATMOS and sodar results (C_n^2) for the 24-h period on 8 Oct 91.

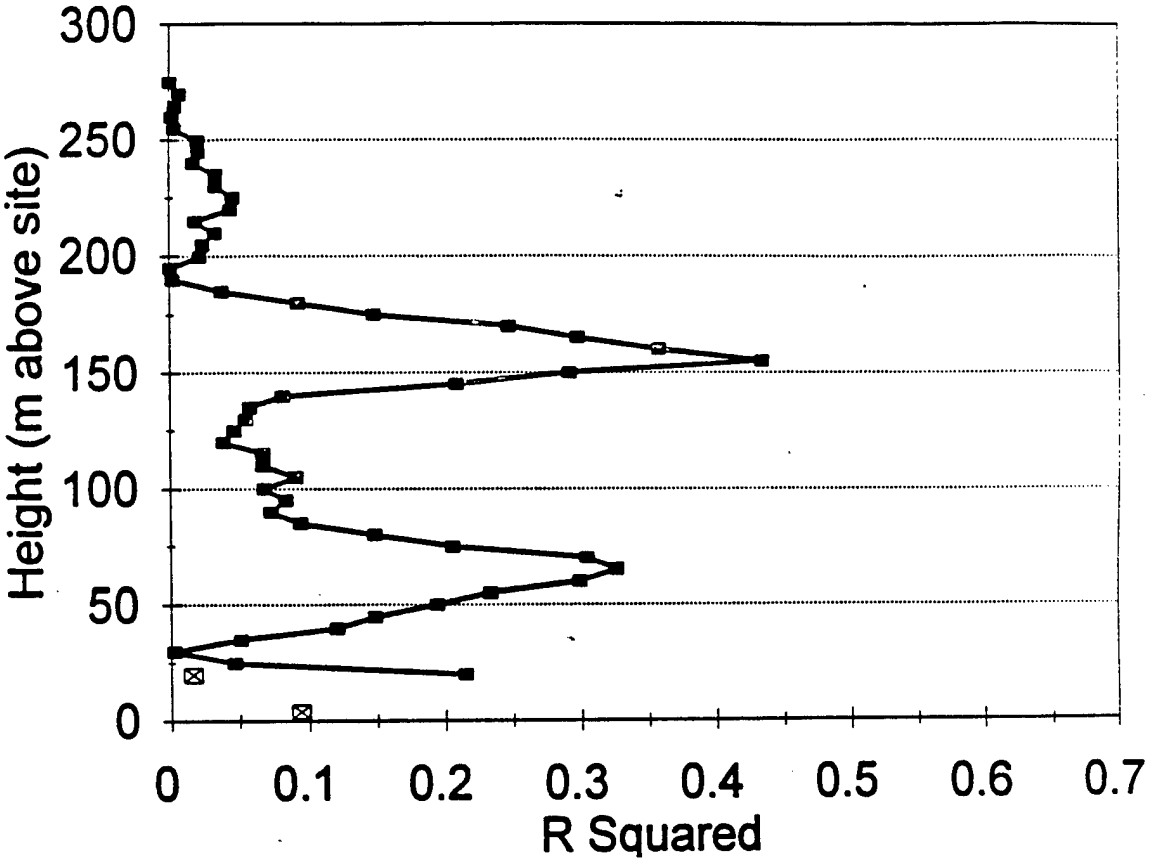

Figure 48. Coefficient of determination values (r^2) calculated for the ATMOS and scintillometer results (C_n^2) and the ATMOS and sodar results (C_n^2) for the midnight to near sunrise period (0000 to 0630 MST).

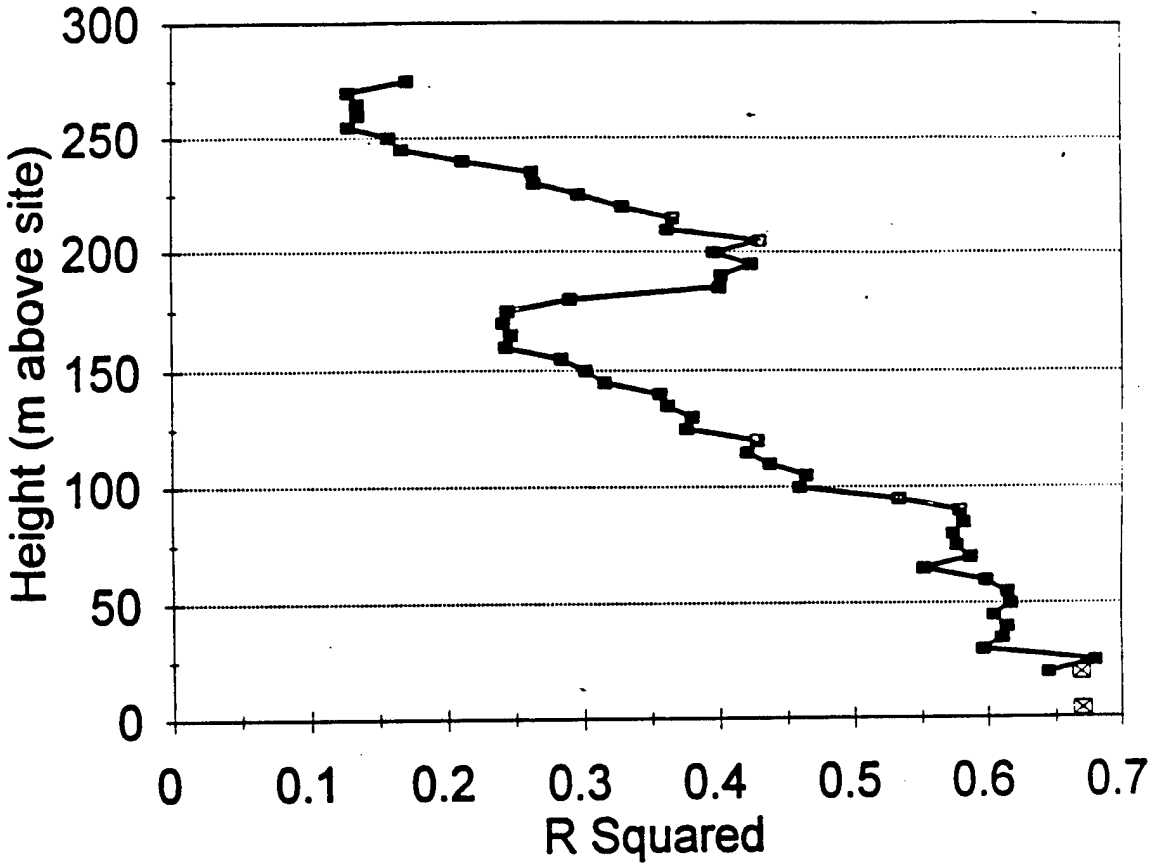

Figure 49. Coefficient of determination values (r^2) calculated for the ATMOS and scintillometer results (C_n^2) and the ATMOS and sodar results (C_n^2) for the near sunrise period (0630 to 1715 MST).

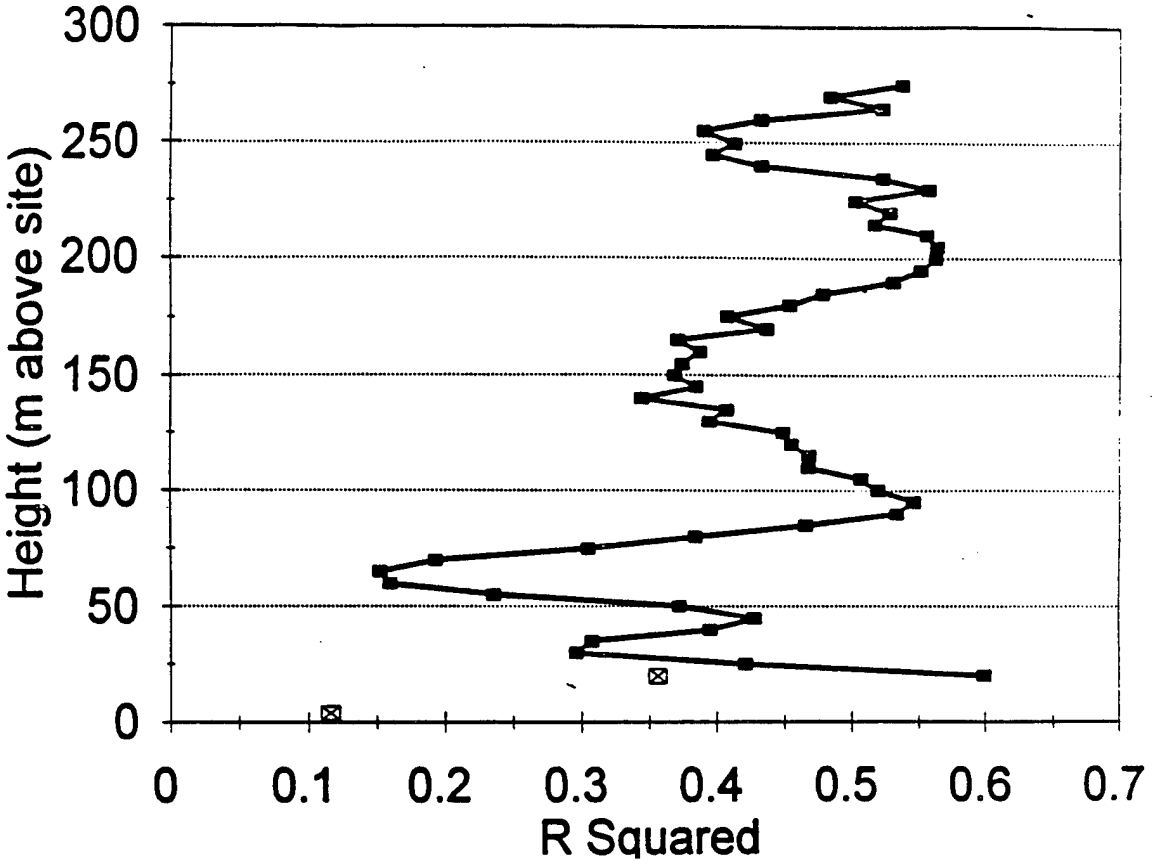

Figure 50. Coefficient of determination values (r^2) calculated for the ATMOS and scintillometer results (C_n^2) and the ATMOS and sodar results (C_n^2) for the near sunset to midnight period (1715 to 2400 MST).

5. Conclusions

From the results presented in this study, five main points emerge regarding the characteristics and fluctuations of r_o:

1. Measurements of r_o at different sites (astronomical observatories on mountaintops, a mesa, and a desert basin), all display lognormal, or near lognormal, distributions. Nastrom and Eaton (1995) found the variances of all three wind components, the spectral width, and the refractive index structure parameter, follow lognormal frequency distributions. Often, several days of data are required to produce a smooth distribution.

2. During times with well-developed convection, the thermal activity causes pronounced short-term fluctuations in ground-to-space measurements of the variance of differential image motion with patterns identified every few minutes. These effects are also seen in the transverse coherence length r_o. Scintillometer-derived horizontal path C_n^2 measurements, coupled with sodar C_n^2 measurements describe the diurnal evolution of C_n^2 from 4 to 276 m AGL. Strong fluctuations in the sodar time-height display of the unstable boundary layer were observed from about 0930 to 1600 MST, agreeing with the times of strong fluctuations in the ground-to-space observations.

3. All measurements (differential image motion variance and C_n^2 derived from the scintillometers and sodar) responded nearly simultaneously to the time of the evening neutral event (near 1700 MST). The best seeing conditions, and the lowest C_n^2 during the 24-h period were found during this event. The morning neutral event, as is typical, did not show as strong an effect as the evening event.

4. The night (stable) atmosphere showed the greatest complexity during the diurnal cycle with features observed using the sodar including elevated inversions, laminated structures, and sinusoidal oscillations identified as internal gravity waves. The scintillometer and ATMOS measurements showed slowly varying patterns presumably responding to the large complex turbulent patterns in the planetary boundary layer. Therefore, night changes in r_o can show

changes from several minutes to several hours, depending on the nature of the features present.

5. Although the poorest average seeing conditions are found during midday, the fine structure and patterns of convective activity shown here, along with the short-term observations of image motion variance and r_o, show that opportunities of a few minutes duration randomly occur in which the seeing is equivalent to some seeing conditions during night. Communication systems that may not be able to operate under the average day turbulent conditions may exceed their threshold requirements during the momentary good seeing conditions, presumably during times of subsidence.

Other atmospheric features and conditions create C_n^2 at heights high above the sensing capability of sodar, such as the tropopause (wind shear at the top and bottom of an overhead jet stream), and stratospheric breaking gravity waves (Nastrom and Eaton 1993b). These produce a contribution to the integrated-path C_n^2 as shown from high-resolution thermosonde measured profiles (Eaton et al. 1985), but the greatest contribution from C_n^2 to r_o is generally found in the planetary boundary layer. The features above the boundary layer usually are persistent and produce slowly varying optical effects.

References

Brost, R. A., and J. C. Wyngaard, "A Model Study of the Stably Stratified Planetary Boundary Layer, (U)" *Journal of Atomospheric Sciences*, **35**, p 1427-1440, 1978.

Couder, A., "Optique Atmospherique-Measure Photographique de l'agitation des Images Stellaries, (U)" *C.R. Academy Sciences, Paris*, **205**, p 609-611, 1936.

Eaton, F. D., D. M. Garvey, E. Dewan, and R. Beland, "Transverse Coherence Length (r_o) Observations, (U)" In *Proceedings of the SPIE Meeting*, **551**, Arlington, VA, p 42-50, 1985.

Eaton, F. D., W. A. Peterson, J. R. Hines, K. R. Peterman, R. E. Good, R. R. Beland, and J. H. Brown, "Comparisons of VHF Radar, Optical, and Temperature Fluctuation Measurements of C_n^2, r_o and θ_o, (U)" *Theoretical and Applied Climatology*, **39**, p 17-29, 1988a.

Eaton, F. D., W. A. Peterson, J. R. Hines, J. J. Drexler, A. H. Waldie, and D. B. Soules, "Comparison of Two Techniques for Atmospheric Seeing, (U)" In *Proceedings of the SPIE Meeting*, **926**, Orlando, FL, p 319-334, 1988b.

Eaton, F. D., W. A. Peterson, J. R. Hines, J. J. Drexler, A. H. Waldie, D. B. Soules, and J. A. Qualtrough, "Phase Structure Measurements With Multiple Apertures, (U)" In *Proceedings of the SPIE*, **1115**, Orlando, FL, p 218-223, 1989.

Eaton, F. D., W. A. Peterson, and J. R. Hines, "Morphology of Transparent Inhogeneities, (U)" In *Proceedings of the SPIE*, **1312**, Orlando, FL, p 134-146, 1990.

Forbes, F. F., "Dome Induced Image Motion, Advanced Technology Telescopes, (U)" In *Proceedings of SPIE 332*, Tucson, AZ, p 185-192, 1982.

Forbes, F. F., E. S. Barker, K. R. Peterman, D. D. Cudabeck, and D. A. Morse, "High Altitude Acoustic Sounders," In *Proceedings of the SPIE*, **551**, Arlington, VA, p 60-71, 1985.

Fried, D. L., "Optical Resolution Through a Randomly Inhomogeneous Medium for Very Long and Short Exposures," *Journal of the Optical Society of America*, **567**, p 1372-1379, 1966.

Fried, D. L., "Differential Angle of Arrival: Theory, Evaluation, and Measurement Feasibility," *Radio Science*, **10**, 77-86, 1975.

Garrett, J. R., and R. A. Brost, "Radiative Cooling Effects Within and Above the Nocturnal Boundary Layer," *Journal of Atmospheric Sciences*, **38**, p 2730-2746, 1981.

Gossard, E. E. and W. H. Hooke, "Waves in the Atmosphere," p 456, Elsevier, NY, 1975.

Grace, J., D. Garvey, F. Eaton, J. Hines, W. Peterson, G. Hoidale, J. Kahler, and B. Matise, *Atmospheric Characterization at White Sands Missile Range for the SDC IV Program Data Report*, ASL-DR-89-0005, **I-IV**, U.S. Army Atmospheric Sciences Laboratory, White Sands Missile Range, NM, 1990.

Hines, C. O., "Comments on a Paper by E. E. Gossard, J. H. Richter, and D. Atlas: Internal Waves in the Atmosphere From High Resolution Radar Measurements," *Journal of Geophysical Research*, **75**, p 5956-5959, 1970.

Hines, J. R., S. A. McLaughlin, F. D. Eaton, and W. H. Hatch, "The U.S. Army Atmospheric Profiler Research Facility: Introduction and Capabilities," In *Proceedings of the 8th Sympos. on Meteorol. Obs. and Instrumen., AMS*, Anaheim, CA, p 237-242, 1993.

Hoidale, M. M., M. P. Dayton, and L. Newman, *Atmospheric Structure, White Sands Missile Range, New Mexico, Part 3, Upper Air and Surface Data: Holloman Site*, ECOM-DR-877, U.S. Army Atmospheric Sciences Laboratory, White Sands Missile Range, NM, 1975.

Hooke, W. H., and R. M. Jones, "Dissipative Waves Excited by Gravity-Wave Encounters With the Stably Stratified Planetary Boundary Layer," *Journal of Atmospheric Sciences*, **43**, p 2048-2060, 1986.

Hootman, B. W., and W. Blumen, "Analysis of Nighttime Drainage Winds in Boulder, Colorado, During 1980," *Monthly Weather Review*, **111**, p 1052-1061, 1983.

Kaimal, J. C., J. C. Wyngaard, D. A. Haugen, O. R. Cote, and Y. Izumi, "Turbulent Structure in the Convective Boundary Layer," *Journal of Atmospheric Sciences*, **33**, p 2152-2169, 1976.

Merrill, K. M., G. Favot, F. Forbes, D. Morse, and G. Poczulp, "Planning the National New Technology Telescope (NNTT):VII, Site Evaluation Project Observation and Analysis Procedures, Advanced Technology Operational Telescopes III," In *Proceedings of SPIE 628*, Tucson, AZ, p 148-154, 1986.

Miller, M. G., and P. F. Kellen, "Astronomical Differential Angle of Arrival Measurements," in *Digest of Technical Papers, Meeting on Imaging in Astronomy*, Cambridge, MA, WB3/1-WB3/4, 1975.

Moroder, E., and A. Righini, "The Evaluation of Nighttime Seeing from Polar Star Trails," *Astronomy and Astrophysics* **23**, p 307-310, 1973.

Nastrom, G. D., and F. D. Eaton, "Onset of the Summer Monsoon Over White Sands Missile Range, New Mexico, As Seen By VHF Radar," *Journal of Geophysical Research*, **98**, No. D12, p 23, 235-23, 243, 1993a.

Nastrom, G. D., and F. D. Eaton, "The Coupling of Gravity Waves and Turbulence at White Sands, New Mexico, From VHF Radar Observations," *Journal of Applied Meteorology*, **32**, p 81-87, 1993b.

Nastrom, G. D., and F. D. Eaton, "Variations of Winds and Turbulence Seen by the 50 MHz Radar at White Sands Missile Range, New Mexico," *Journal of Applied Meteorology*, **34**, 10, p 2135-2148, 1995.

Neff, W. D., and R. L. Coulter, "Acoustic Remote Sensing," *Probing the Atmospheric Boundary Layer*, ed. D. H. Lenschow, American Meteorological Society, Boston, MA, p 269, 1986.

Ochs, G. R., W. D. Cartwright, and D. D. Russell, NOAA Tech. Memo ERL WPL-51, "Optical Instrument Model II," 1980.

Redelsperger, J. L., and T. L. Clark, "The Initiation and Horizontal Scale Selection of Convection Over Gently Sloping Terrain," *Journal of Atmospheric Sciences*, **47**, p 515-541, 1990.

Roddier, F., "The Effects of Atmospheric Turbulence in Optical Astronomy," *Progress in Optics*, **XIX**, North Holland, p 283-368, 1981.

Schneider, R. S., "Large Amplitude Mesoscale Wind Disturbances Within the Intense Midwest Extratropical Cyclone of 15 December 1987," *Weather and Forecasting*, **5**, p 721-729, 1990.

Stobie, J. G., F. Einaudi, and L. W. Uccellini, "A Case Study of Gravity Waves - Convective Storms Interaction: May 1979," *Journal of Atmospheric Sciences*, **40**, p 2804-2830, 1983.

Taft, P. H., and M. M. Hoidale, *White Sands Missile Range Climatography No. 3, Apache Site, WSMR*, ECOM-DR-387, U.S. Army Electronics Command, Atmospheric Office Report, U.S. Army Atmospheric Sciences Laboratory, WSMR, NM, 1969.

Tatarskii, V. I., *Wave Propagation in a Turbulent Medium*, New York, NY, McGraw-Hill, p 285, 1961.

Uccellini, L. W., and S. E. Koch, "The Synoptic Setting and Possible Energy Sources for Mesoscale Wave Disturbances," *Monthly Weather Review*, **115**, p 721-729, 1987.

Van Zandt, T. E., H. Y. Chun, W. Clark, F. Einaudi, G. D. Nastrom, A. C. Riddle, and J. M. Warnock, "A Monochromatic Gravity Wave Observed by the Flatland Atmospheric Observatory," Reprints *9th Conference on Atmospheric and Oceanic Waves and Stability*, San Antonio, TX, p 185-188, 1993.

Whitford, A. E., and J. Stebbins, "Photoelectric Measurement of Scintillation of Stars," *Publication of American Astronomy*, **8**, p 228, 1936.

Wyngaard, J. C., Y. Izumi, and S. A. Collins, "Behavior of the Refractive-Index-Structure Parameter Near the Ground," *Journal of the Optical Society of America*, **61**, p 1646-1650, 1971.

Acronyms and Abbreviations

AGL	above ground level
APO	Apache Point Observatory
APRF	Atmospheric Profiler Research Facility
ATMOS	Atmospheric Turbulence Measurement and Observation System
CCD	charge-coupled device
FLWO	Fred Lawrence Whipple Observatory
KPNO	Kitt Peak National Observatory
MSL	mean sea level
MST	mountain standard time
NOAO	National Optical Astronomy Observatories
NRAO	National Radio Astronomy Observatory
NSF	National Science Foundation
NSO	National Solar Observatory
SDSS	Sloan Digital Sky Survey
WIYN	University of Wisconsin, Indiana University, Yale University and NOAO Consortium
WSMR	White Sands Missile Range

Appendix

Due to the large amount of data collected at Apache Point Observatory during 1995 (84 nights), these data are included in the appendix. For convenience to the reader, a frequency summarizing each month's data is included at the end of each month's ensemble of time series data.

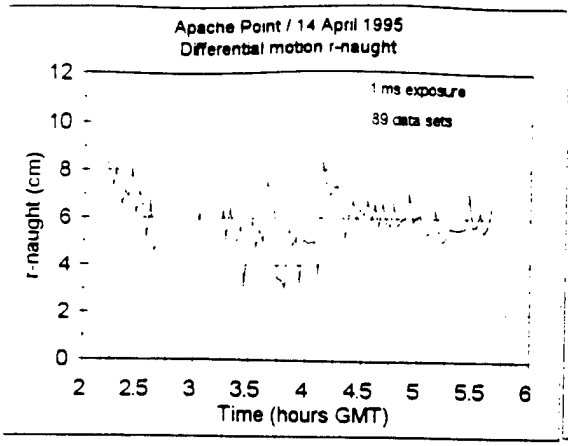
Apache Point / 14 April 1995
Differential motion r-naught
1 ms exposure
89 data sets
r-naught (cm)
Time (hours GMT)

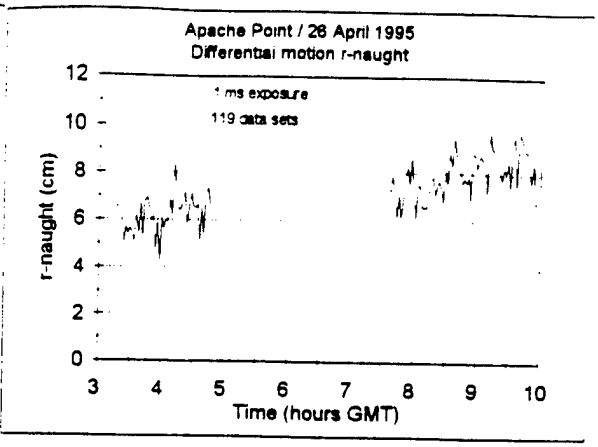
Apache Point / 26 April 1995
Differential motion r-naught
1 ms exposure
119 data sets
r-naught (cm)
Time (hours GMT)

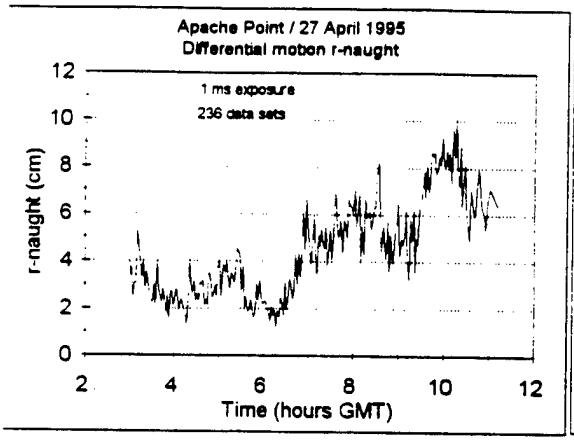
Apache Point / 27 April 1995
Differential motion r-naught
1 ms exposure
236 data sets
r-naught (cm)
Time (hours GMT)

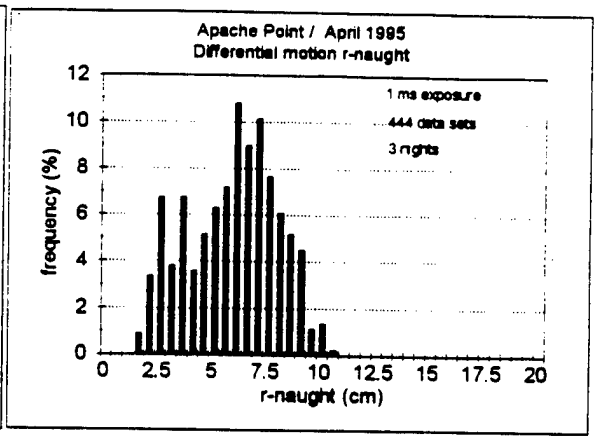
Apache Point / April 1995
Differential motion r-naught
1 ms exposure
444 data sets
3 nights
frequency (%)
r-naught (cm)

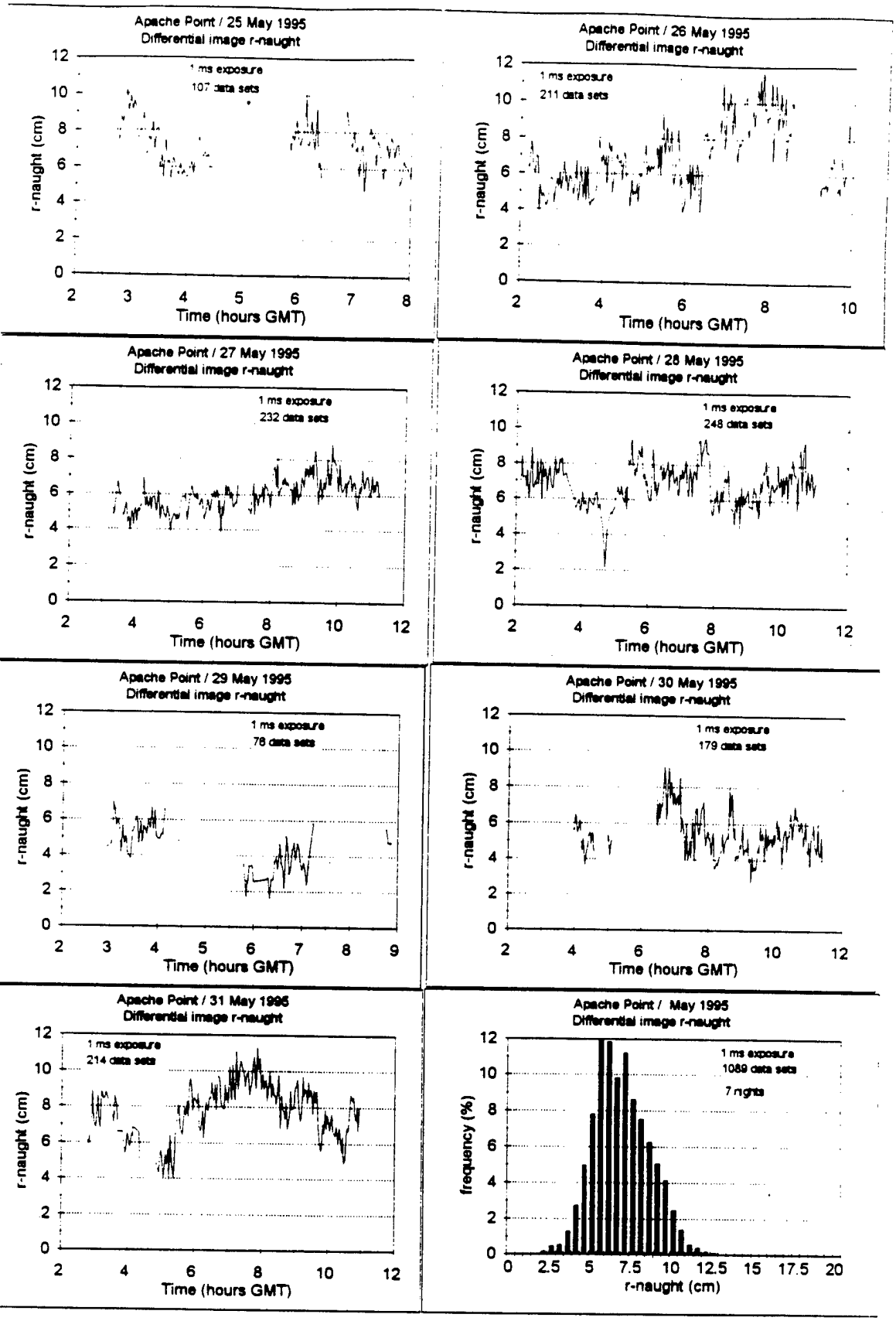
Apache Point / 25 May 1995
Differential image r-naught
1 ms exposure
107 data sets
r-naught (cm)
Time (hours GMT)
Apache Point / 26 May 1995
Differential image r-naught
1 ms exposure
211 data sets
r-naught (cm)
Time (hours GMT)
Apache Point / 27 May 1995
Differential image r-naught
1 ms exposure
232 data sets
r-naught (cm)
Time (hours GMT)
Apache Point / 28 May 1995
Differential image r-naught
1 ms exposure
248 data sets
r-naught (cm)
Time (hours GMT)
Apache Point / 29 May 1995
Differential image r-naught
1 ms exposure
78 data sets
r-naught (cm)
Time (hours GMT)
Apache Point / 30 May 1995
Differential image r-naught
1 ms exposure
179 data sets
r-naught (cm)
Time (hours GMT)
Apache Point / 31 May 1995
Differential image r-naught
1 ms exposure
214 data sets
r-naught (cm)
Time (hours GMT)
Apache Point / May 1995
Differential image r-naught
1 ms exposure
1089 data sets
7 nights
frequency (%)
r-naught (cm)

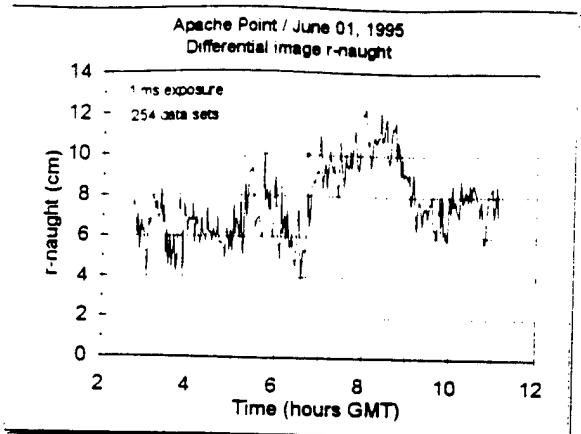
Apache Point / June 01, 1995
Differential image r-naught
1 ms exposure
254 data sets
r-naught (cm)
Time (hours GMT)

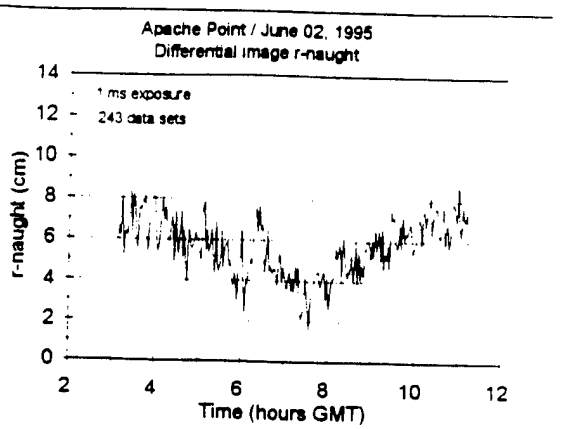
Apache Point / June 02, 1995
Differential image r-naught
1 ms exposure
243 data sets
r-naught (cm)
Time (hours GMT)

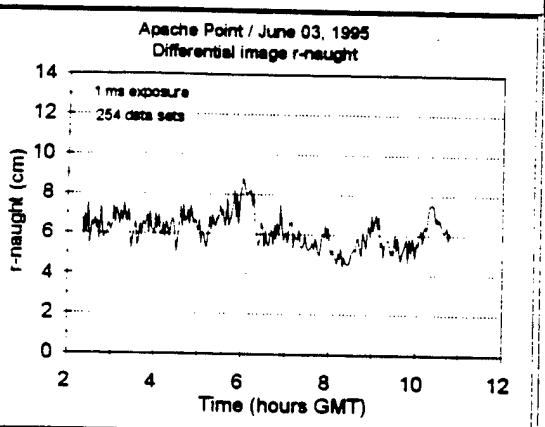
Apache Point / June 03, 1995
Differential image r-naught
1 ms exposure
254 data sets
r-naught (cm)
Time (hours GMT)

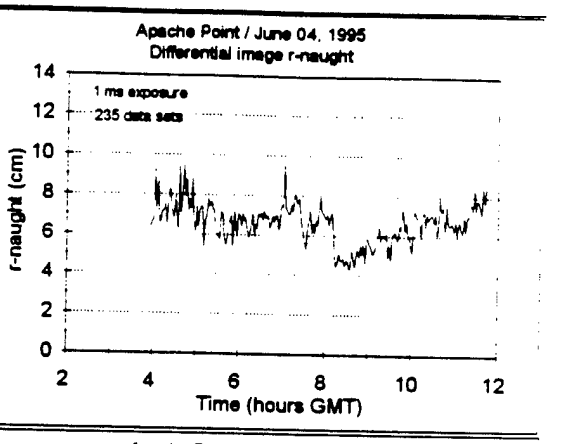
Apache Point / June 04, 1995
Differential image r-naught
1 ms exposure
235 data sets
r-naught (cm)
Time (hours GMT)

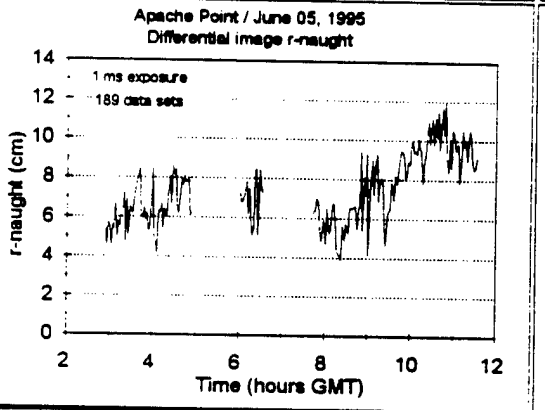
Apache Point / June 05, 1995
Differential image r-naught
1 ms exposure
189 data sets
r-naught (cm)
Time (hours GMT)

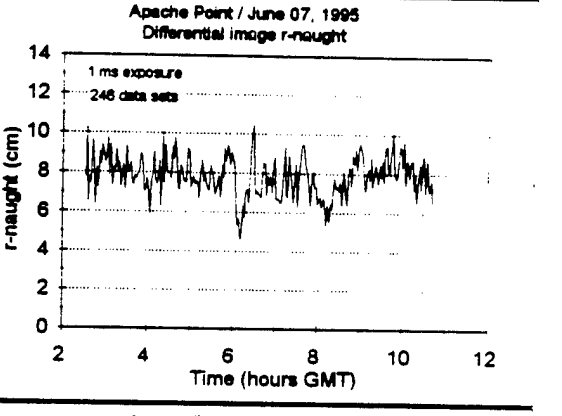
Apache Point / June 07, 1995
Differential image r-naught
1 ms exposure
246 data sets
r-naught (cm)
Time (hours GMT)

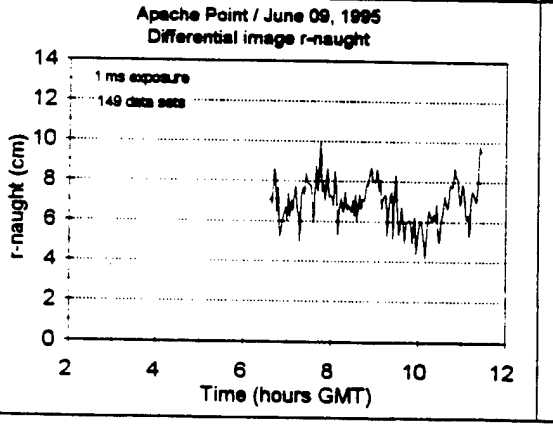
Apache Point / June 09, 1995
Differential image r-naught
1 ms exposure
149 data sets
r-naught (cm)
Time (hours GMT)

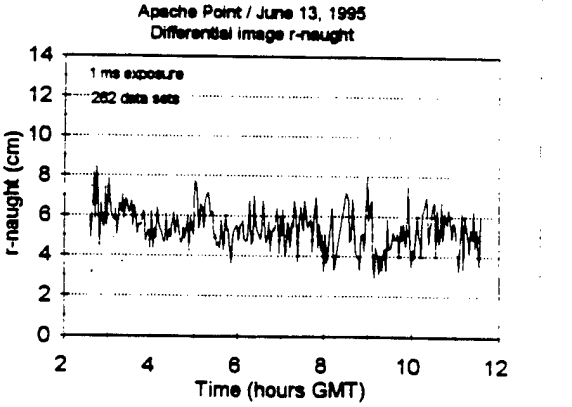
Apache Point / June 13, 1995
Differential image r-naught
1 ms exposure
262 data sets
r-naught (cm)
Time (hours GMT)

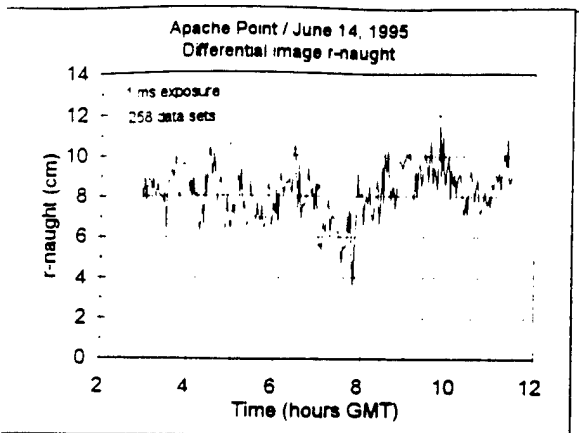
Apache Point / June 14, 1995
Differential image r-naught
1 ms exposure
258 data sets
r-naught (cm)
Time (hours GMT)

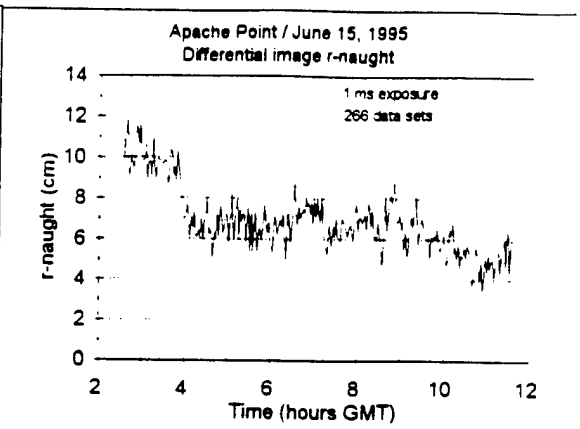
Apache Point / June 15, 1995
Differential image r-naught
1 ms exposure
266 data sets
r-naught (cm)
Time (hours GMT)

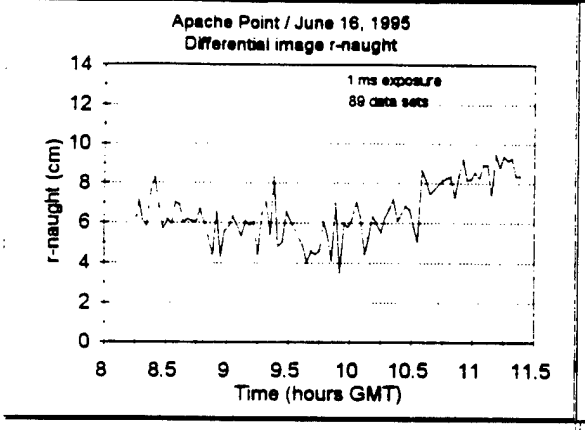
Apache Point / June 16, 1995
Differential image r-naught
1 ms exposure
89 data sets
r-naught (cm)
Time (hours GMT)

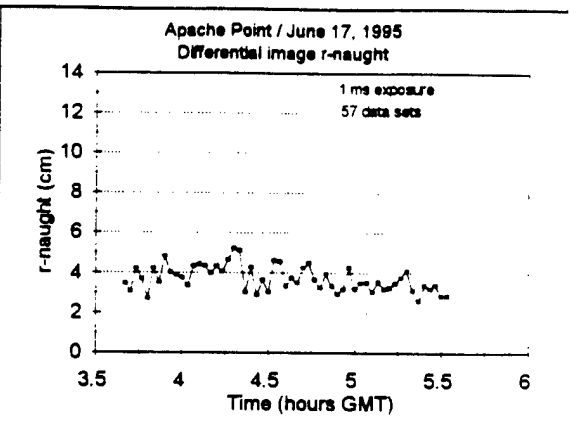
Apache Point / June 17, 1995
Differential image r-naught
1 ms exposure
57 data sets
r-naught (cm)
Time (hours GMT)

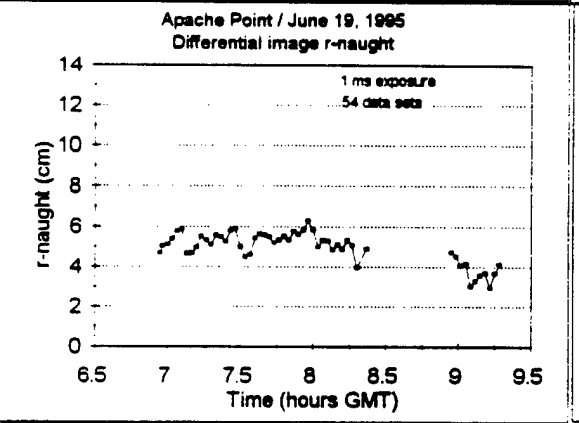
Apache Point / June 19, 1995
Differential image r-naught
1 ms exposure
54 data sets
r-naught (cm)
Time (hours GMT)

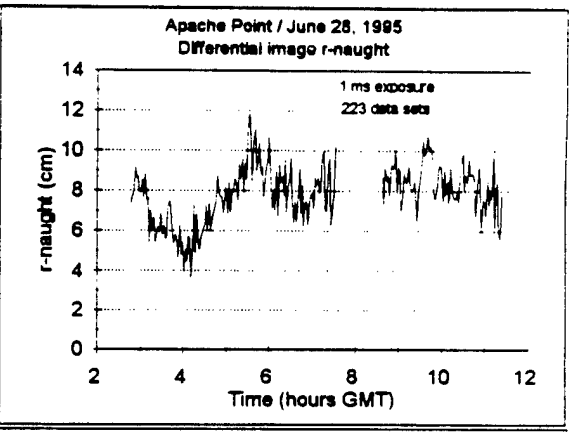
Apache Point / June 28, 1995
Differential image r-naught
1 ms exposure
223 data sets
r-naught (cm)
Time (hours GMT)

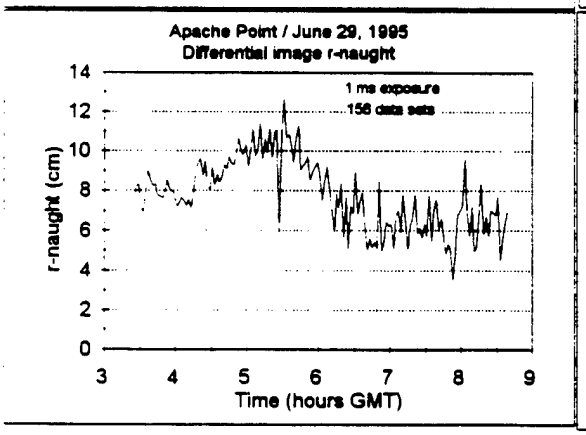
Apache Point / June 29, 1995
Differential image r-naught
1 ms exposure
156 data sets
r-naught (cm)
Time (hours GMT)

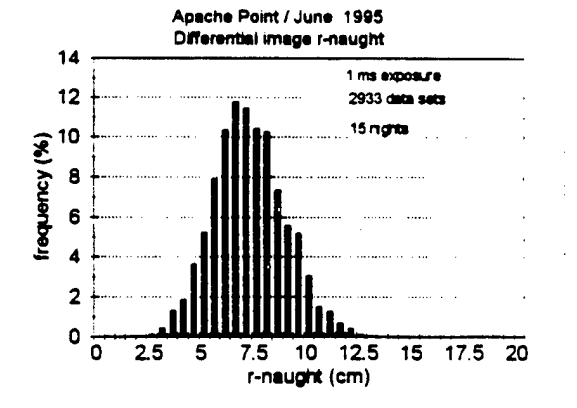
Apache Point / June 1995
Differential image r-naught
1 ms exposure
2933 data sets
15 nights
frequency (%)
r-naught (cm)

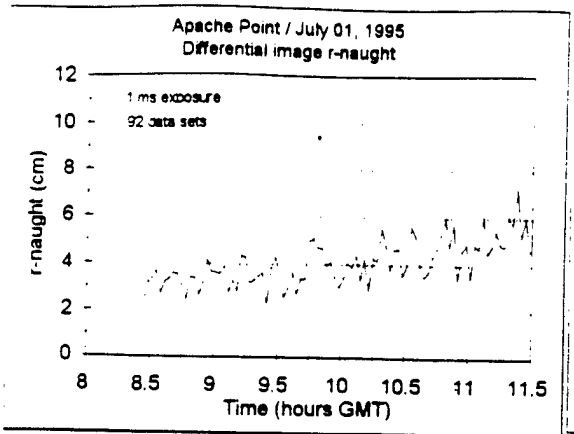
Apache Point / July 01, 1995
Differential image r-naught
1 ms exposure
92 data sets
r-naught (cm)
Time (hours GMT)

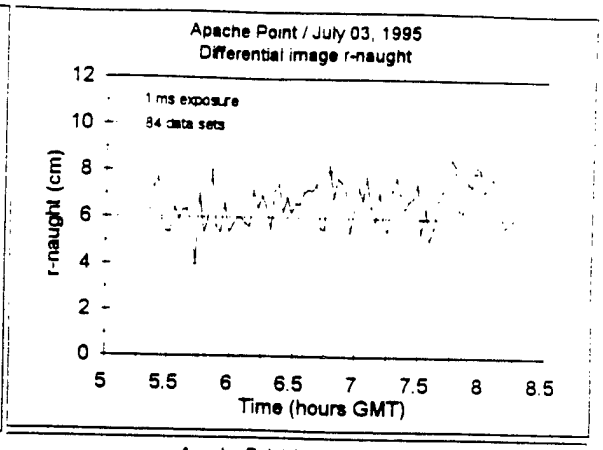
Apache Point / July 03, 1995
Differential image r-naught
1 ms exposure
84 data sets
r-naught (cm)
Time (hours GMT)

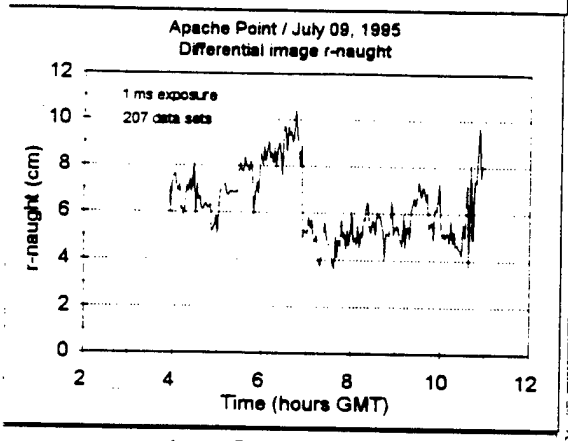
Apache Point / July 09, 1995
Differential image r-naught
1 ms exposure
207 data sets
r-naught (cm)
Time (hours GMT)

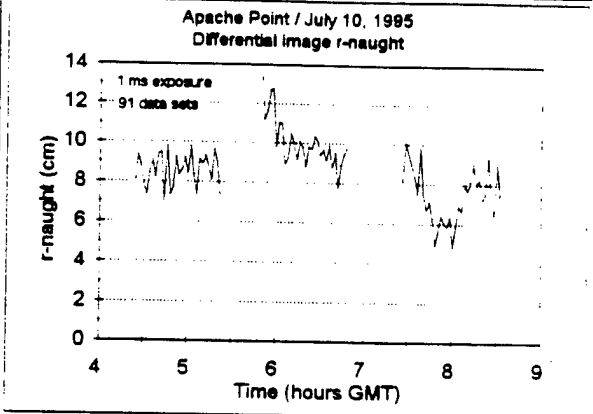
Apache Point / July 10, 1995
Differential image r-naught
1 ms exposure
91 data sets
r-naught (cm)
Time (hours GMT)

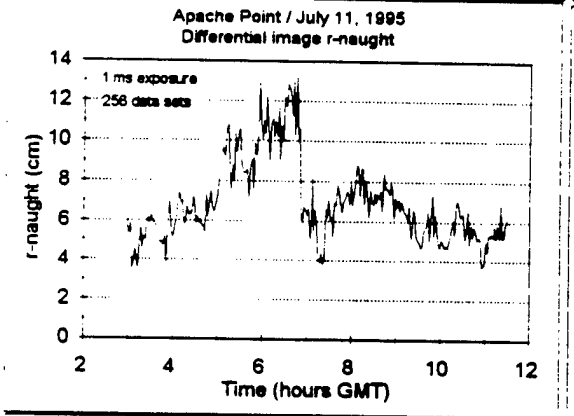
Apache Point / July 11, 1995
Differential image r-naught
1 ms exposure
256 data sets
r-naught (cm)
Time (hours GMT)

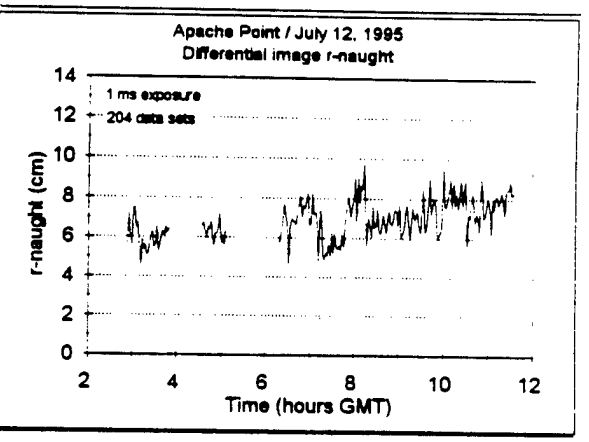
Apache Point / July 12, 1995
Differential image r-naught
1 ms exposure
204 data sets
r-naught (cm)
Time (hours GMT)

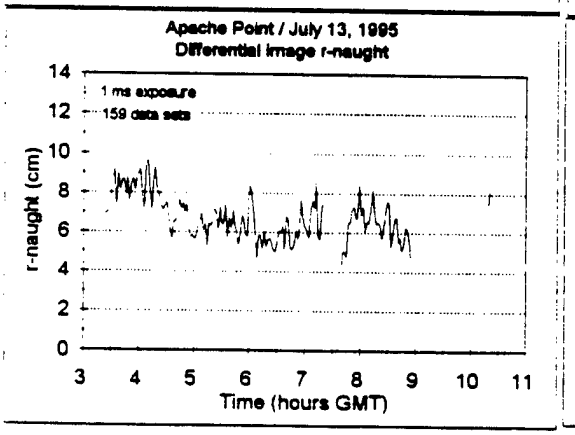
Apache Point / July 13, 1995
Differential image r-naught
1 ms exposure
159 data sets
r-naught (cm)
Time (hours GMT)

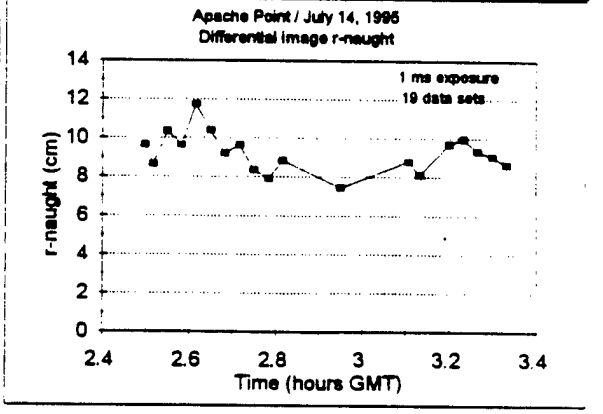
Apache Point / July 14, 1995
Differential image r-naught
1 ms exposure
19 data sets
r-naught (cm)
Time (hours GMT)

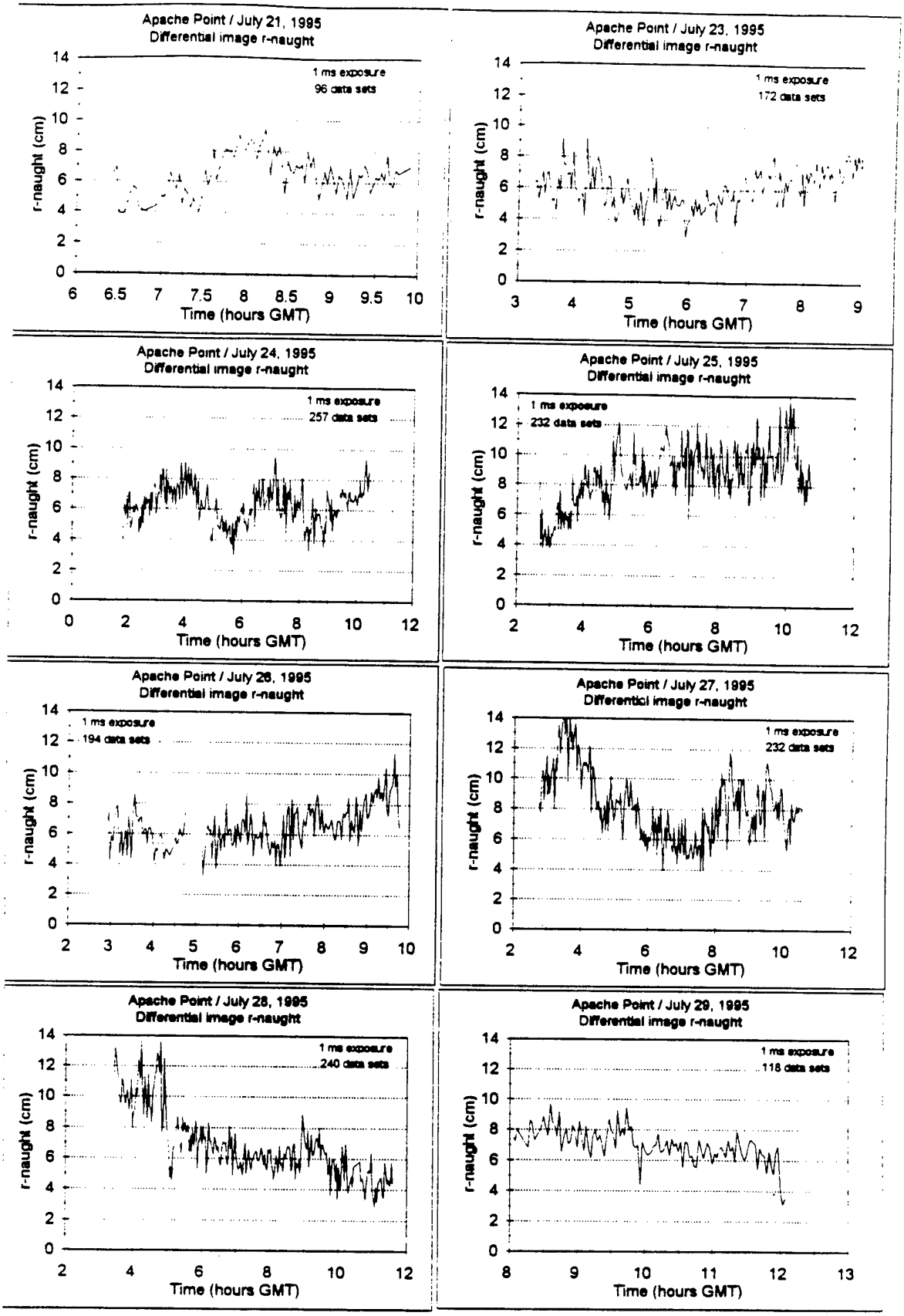
Apache Point / July 21, 1995
Differential image r-naught
1 ms exposure
96 data sets
r-naught (cm)
Time (hours GMT)
Apache Point / July 23, 1995
Differential image r-naught
1 ms exposure
172 data sets
r-naught (cm)
Time (hours GMT)
Apache Point / July 24, 1995
Differential image r-naught
1 ms exposure
257 data sets
r-naught (cm)
Time (hours GMT)
Apache Point / July 25, 1995
Differential image r-naught
1 ms exposure
232 data sets
r-naught (cm)
Time (hours GMT)
Apache Point / July 26, 1995
Differential image r-naught
1 ms exposure
194 data sets
r-naught (cm)
Time (hours GMT)
Apache Point / July 27, 1995
Differential image r-naught
1 ms exposure
232 data sets
r-naught (cm)
Time (hours GMT)
Apache Point / July 28, 1995
Differential image r-naught
1 ms exposure
240 data sets
r-naught (cm)
Time (hours GMT)
Apache Point / July 29, 1995
Differential image r-naught
1 ms exposure
118 data sets
r-naught (cm)
Time (hours GMT)

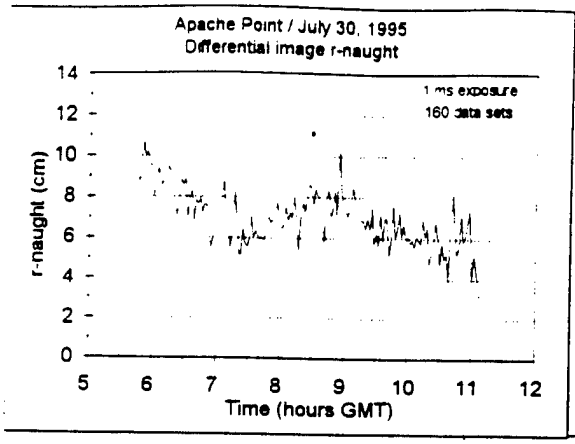
Apache Point / July 30, 1995
Differential image r-naught
1 ms exposure
160 data sets
r-naught (cm)
Time (hours GMT)

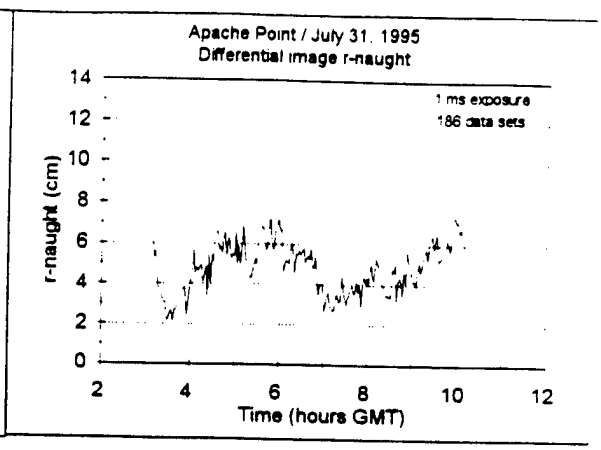
Apache Point / July 31, 1995
Differential image r-naught
1 ms exposure
186 data sets
r-naught (cm)
Time (hours GMT)

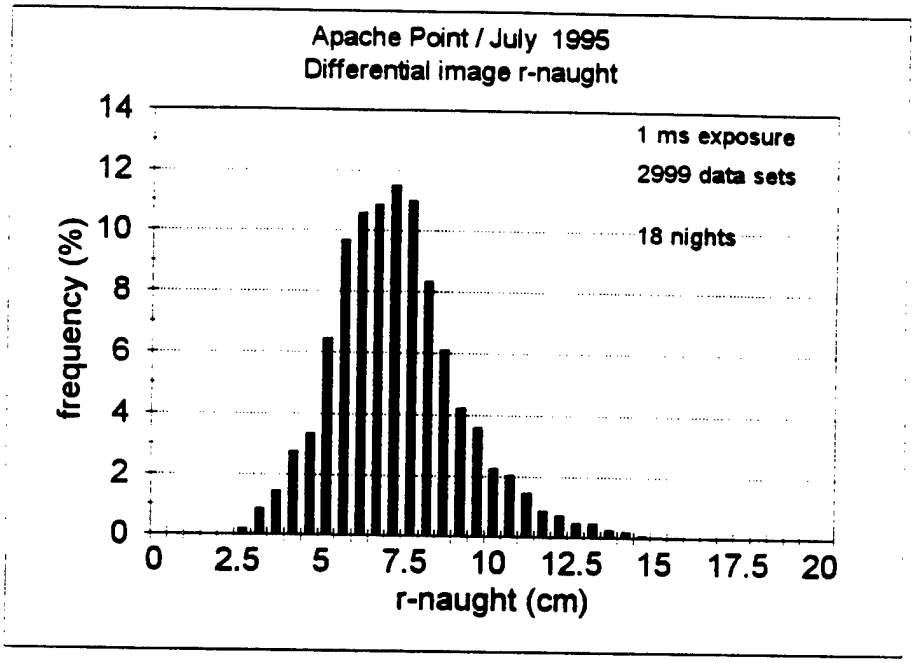
Apache Point / July 1995
Differential image r-naught
1 ms exposure
2999 data sets
18 nights
frequency (%)
r-naught (cm)

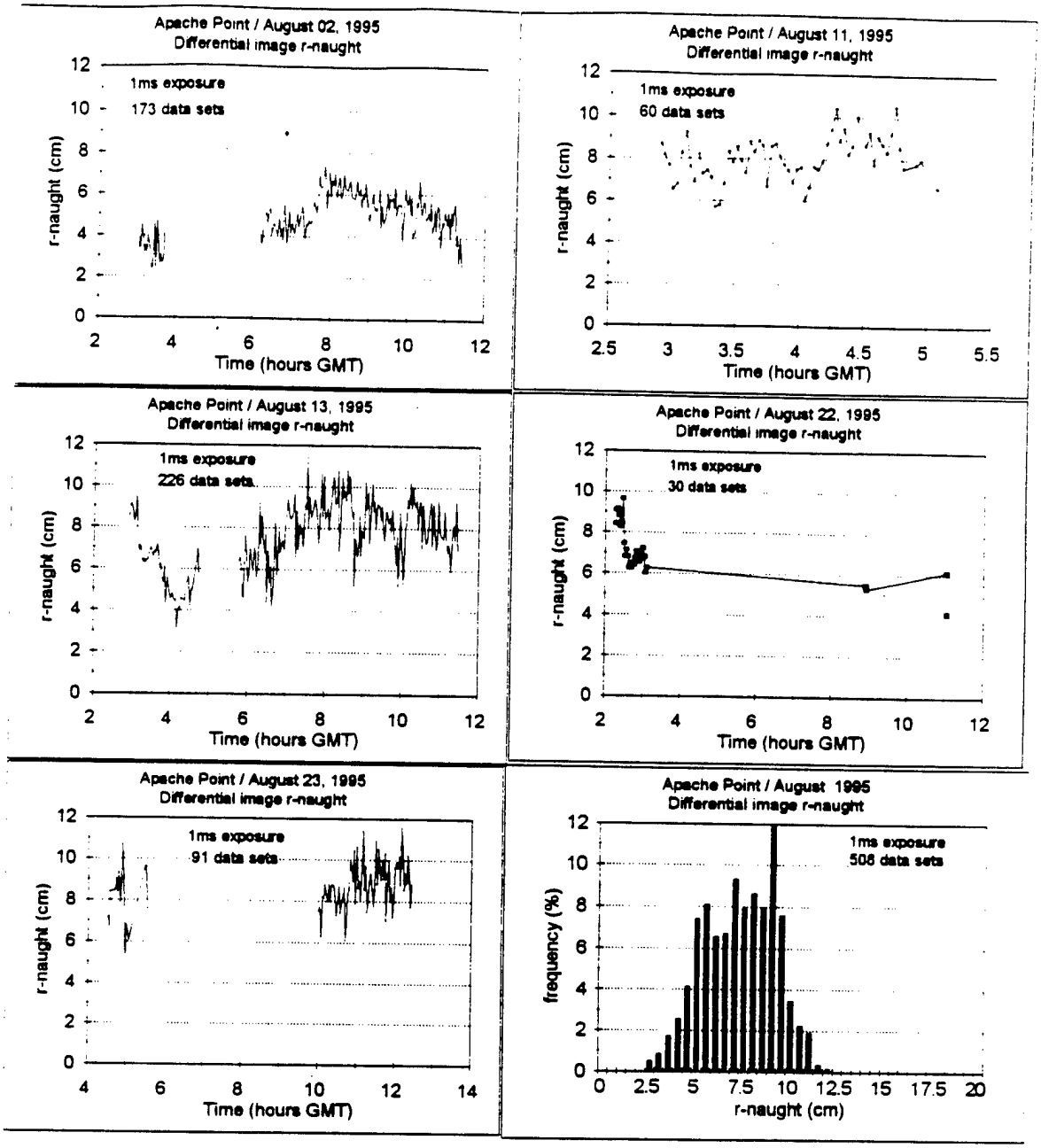
Apache Point / August 02, 1995
Differential image r-naught
1ms exposure
173 data sets
r-naught (cm)
Time (hours GMT)
Apache Point / August 11, 1995
Differential image r-naught
1ms exposure
60 data sets
r-naught (cm)
Time (hours GMT)
Apache Point / August 13, 1995
Differential image r-naught
1ms exposure
226 data sets
r-naught (cm)
Time (hours GMT)
Apache Point / August 22, 1995
Differential image r-naught
1ms exposure
30 data sets
r-naught (cm)
Time (hours GMT)
Apache Point / August 23, 1995
Differential image r-naught
1ms exposure
91 data sets
r-naught (cm)
Time (hours GMT)
Apache Point / August 1995
Differential image r-naught
1ms exposure
508 data sets
frequency (%)
r-naught (cm)

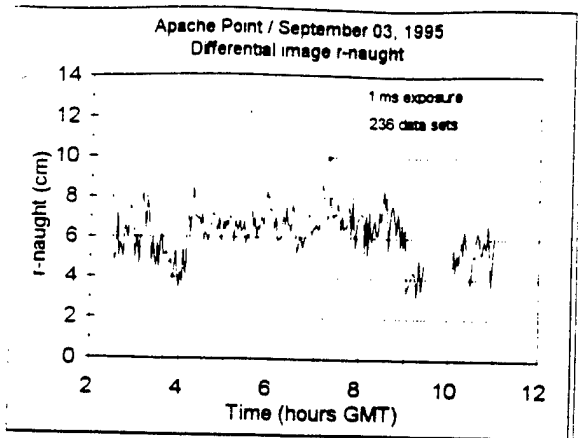
Apache Point / September 03, 1995
Differential image r-naught
1 ms exposure
236 data sets
r-naught (cm)
Time (hours GMT)

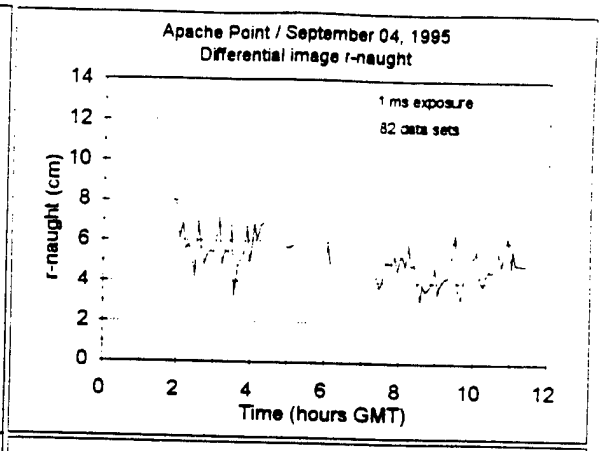
Apache Point / September 04, 1995
Differential image r-naught
1 ms exposure
82 data sets
r-naught (cm)
Time (hours GMT)

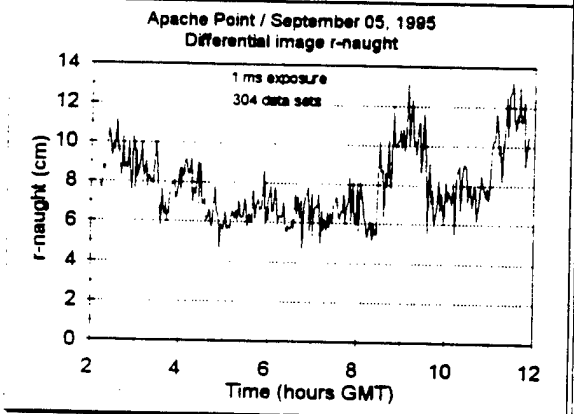
Apache Point / September 05, 1995
Differential image r-naught
1 ms exposure
304 data sets
r-naught (cm)
Time (hours GMT)

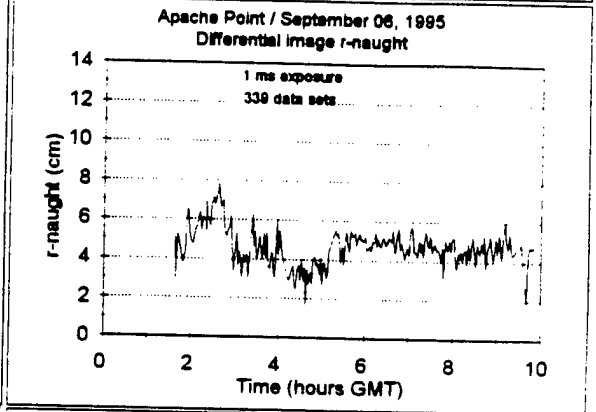
Apache Point / September 06, 1995
Differential image r-naught
1 ms exposure
339 data sets
r-naught (cm)
Time (hours GMT)

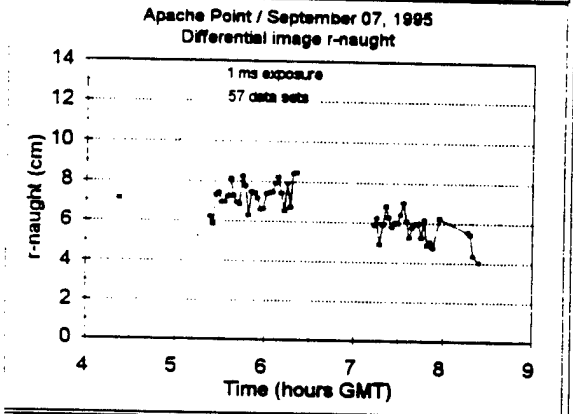
Apache Point / September 07, 1995
Differential image r-naught
1 ms exposure
57 data sets
r-naught (cm)
Time (hours GMT)

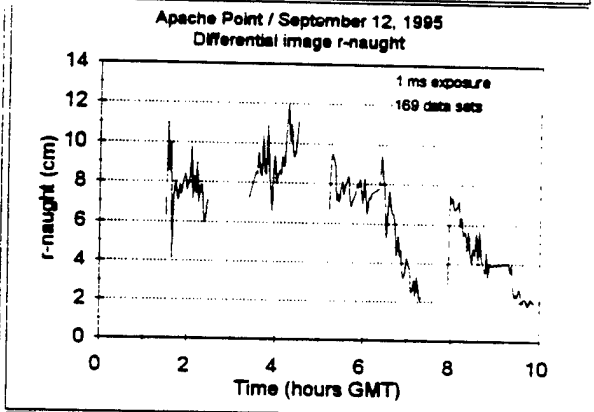
Apache Point / September 12, 1995
Differential image r-naught
1 ms exposure
169 data sets
r-naught (cm)
Time (hours GMT)

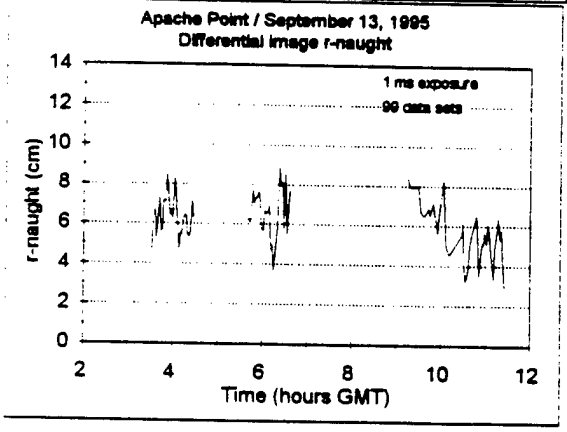
Apache Point / September 13, 1995
Differential image r-naught
1 ms exposure
99 data sets
r-naught (cm)
Time (hours GMT)

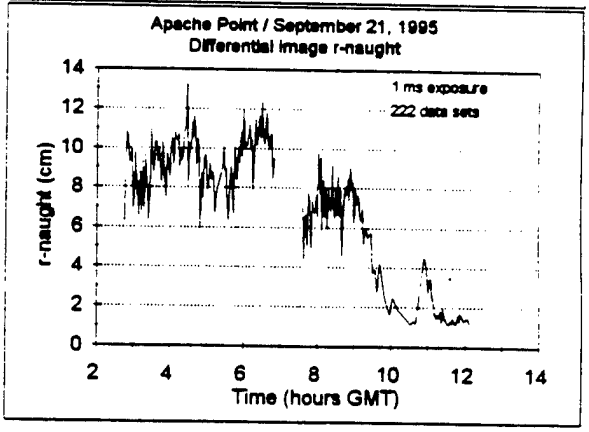
Apache Point / September 21, 1995
Differential image r-naught
1 ms exposure
222 data sets
r-naught (cm)
Time (hours GMT)

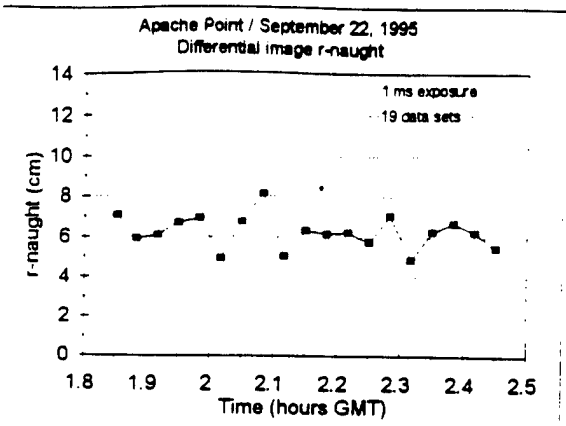
Apache Point / September 22, 1995
Differential image r-naught
1 ms exposure
19 data sets
r-naught (cm)
Time (hours GMT)

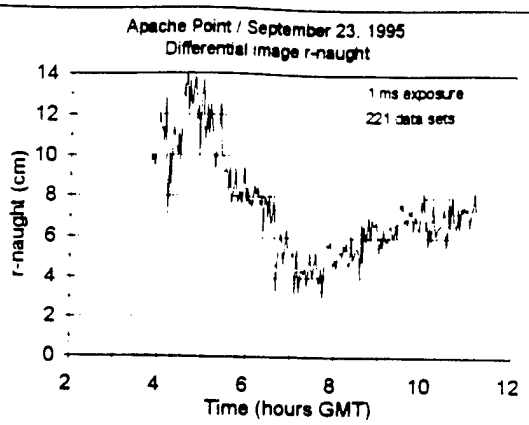
Apache Point / September 23, 1995
Differential image r-naught
1 ms exposure
221 data sets
r-naught (cm)
Time (hours GMT)

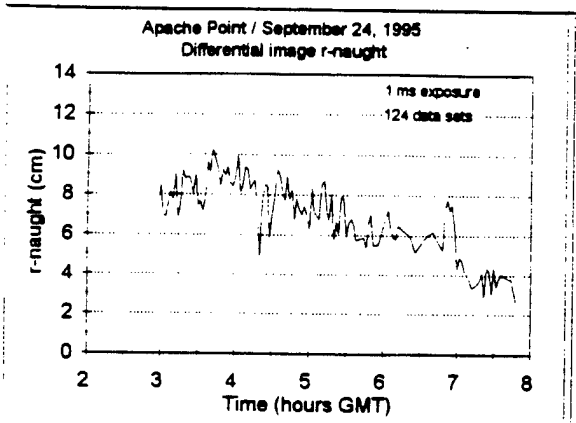
Apache Point / September 24, 1995
Differential image r-naught
1 ms exposure
124 data sets
r-naught (cm)
Time (hours GMT)

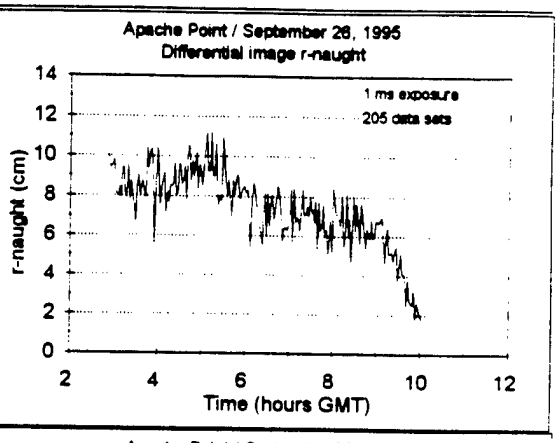
Apache Point / September 26, 1995
Differential image r-naught
1 ms exposure
205 data sets
r-naught (cm)
Time (hours GMT)

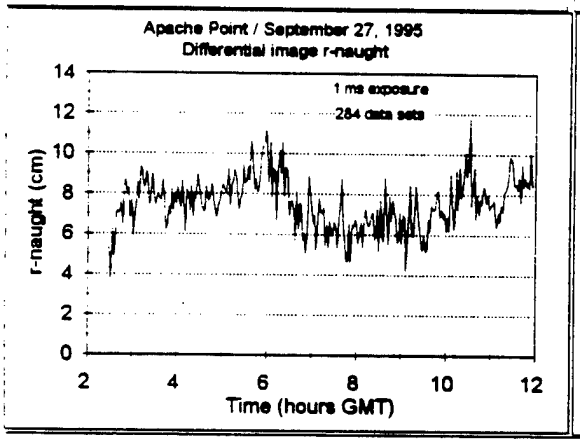
Apache Point / September 27, 1995
Differential image r-naught
1 ms exposure
284 data sets
r-naught (cm)
Time (hours GMT)

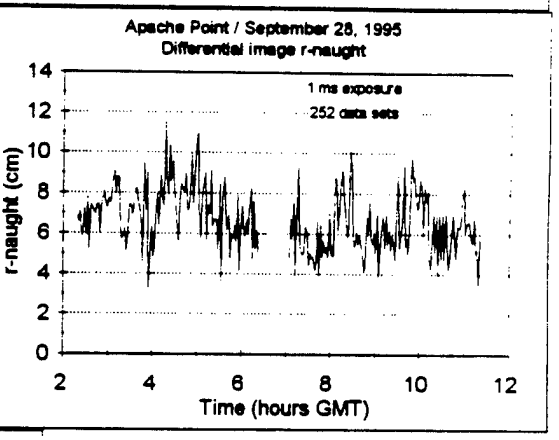
Apache Point / September 28, 1995
Differential image r-naught
1 ms exposure
252 data sets
r-naught (cm)
Time (hours GMT)

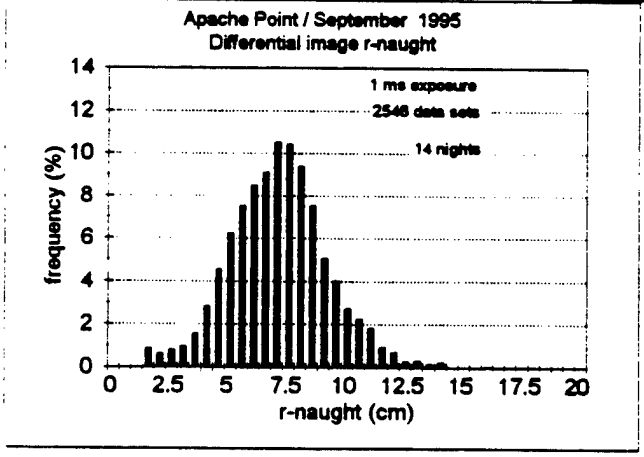
Apache Point / September 1995
Differential image r-naught
1 ms exposure
2546 data sets
14 nights
frequency (%)
r-naught (cm)

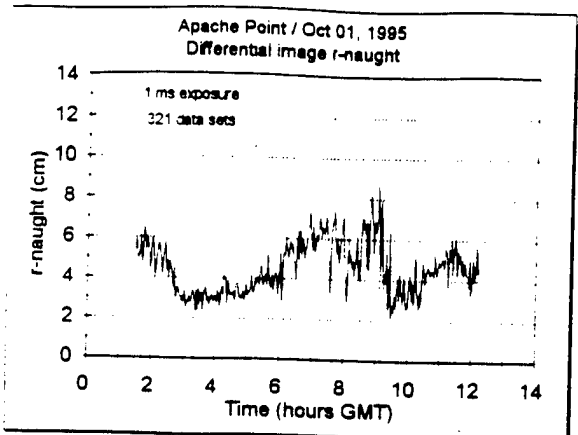
Apache Point / Oct 01, 1995
Differential image r-naught
1 ms exposure
321 data sets
r-naught (cm)
Time (hours GMT)

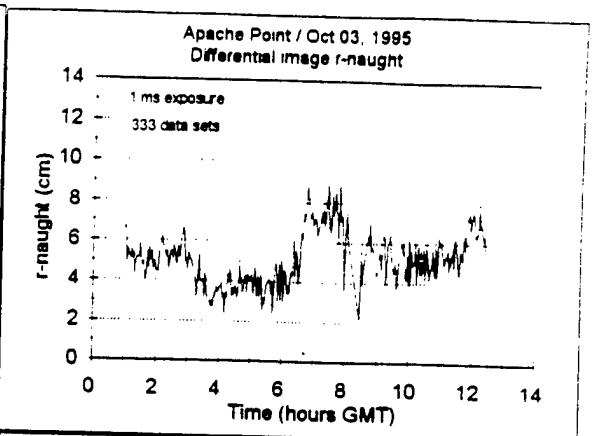
Apache Point / Oct 03, 1995
Differential image r-naught
1 ms exposure
333 data sets
r-naught (cm)
Time (hours GMT)

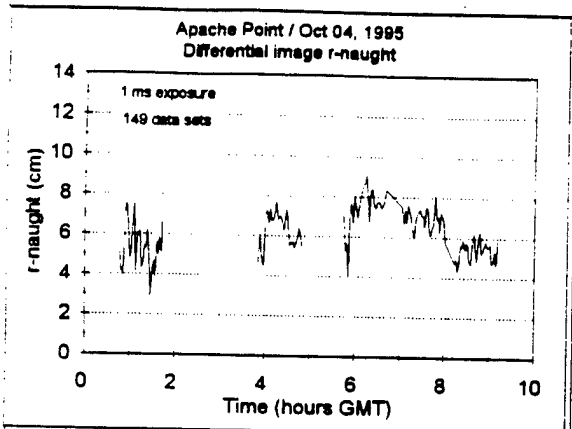
Apache Point / Oct 04, 1995
Differential image r-naught
1 ms exposure
149 data sets
r-naught (cm)
Time (hours GMT)

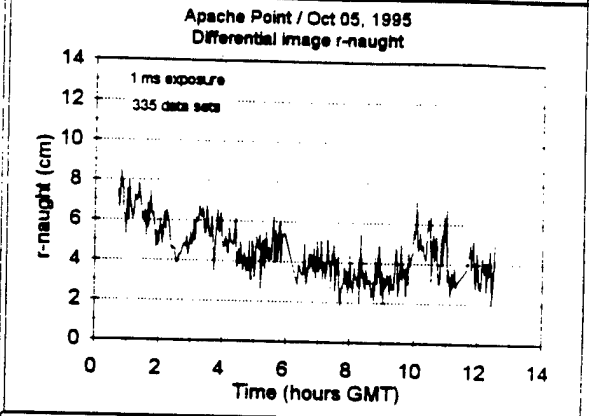
Apache Point / Oct 05, 1995
Differential image r-naught
1 ms exposure
335 data sets
r-naught (cm)
Time (hours GMT)

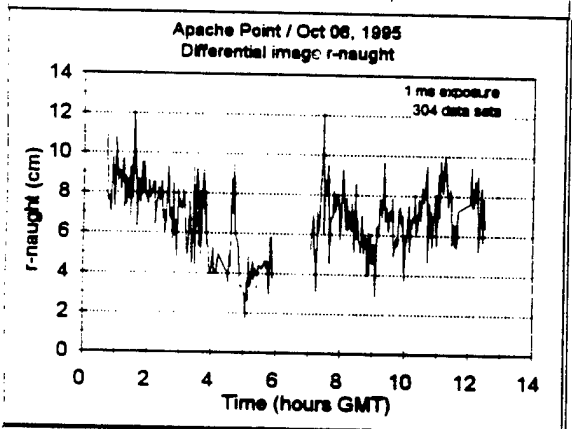
Apache Point / Oct 06, 1995
Differential image r-naught
1 ms exposure
304 data sets
r-naught (cm)
Time (hours GMT)

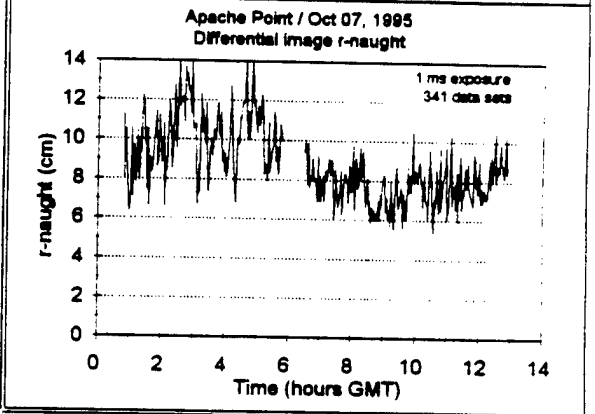
Apache Point / Oct 07, 1995
Differential image r-naught
1 ms exposure
341 data sets
r-naught (cm)
Time (hours GMT)

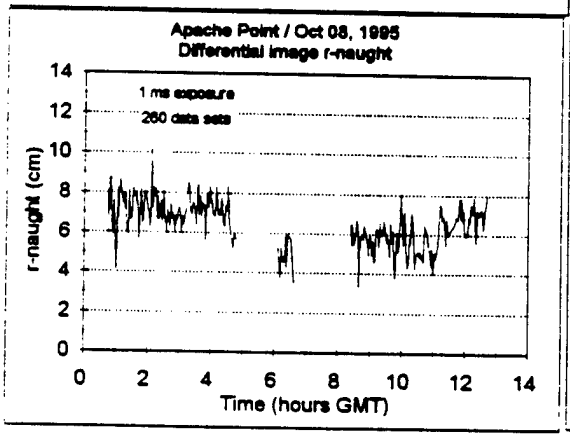
Apache Point / Oct 08, 1995
Differential image r-naught
1 ms exposure
260 data sets
r-naught (cm)
Time (hours GMT)

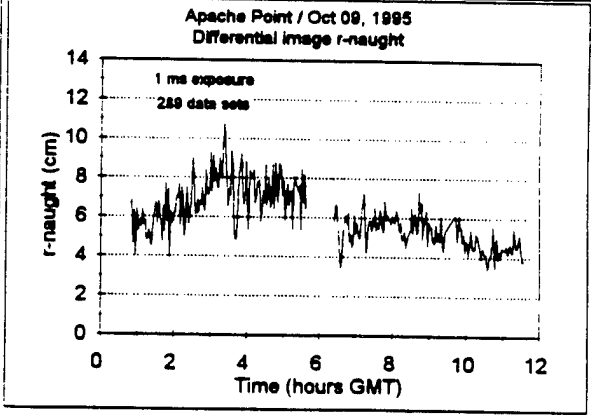
Apache Point / Oct 09, 1995
Differential image r-naught
1 ms exposure
289 data sets
r-naught (cm)
Time (hours GMT)

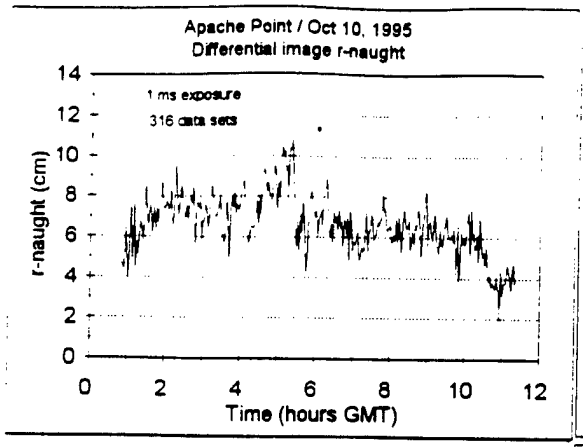
Apache Point / Oct 10, 1995
Differential image r-naught
1 ms exposure
316 data sets
r-naught (cm)
Time (hours GMT)

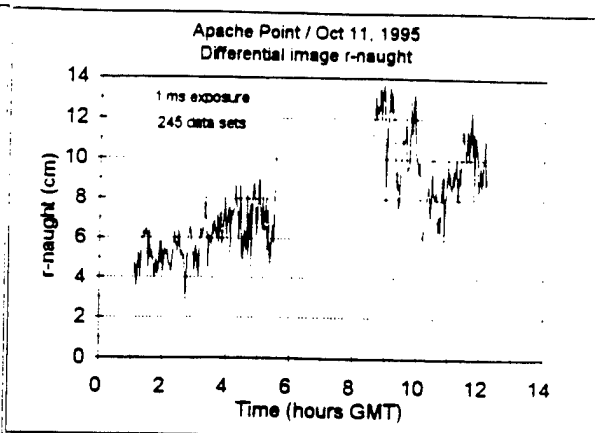
Apache Point / Oct 11, 1995
Differential image r-naught
1 ms exposure
245 data sets
r-naught (cm)
Time (hours GMT)

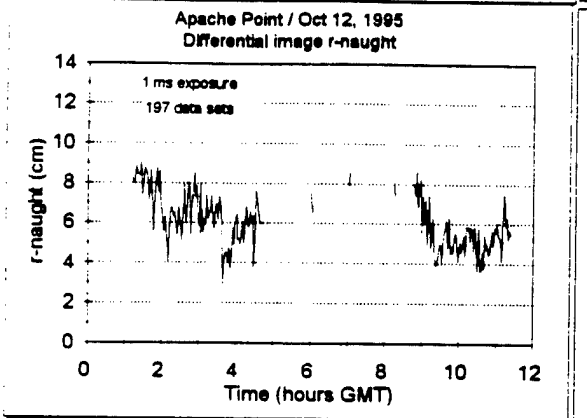
Apache Point / Oct 12, 1995
Differential image r-naught
1 ms exposure
197 data sets
r-naught (cm)
Time (hours GMT)

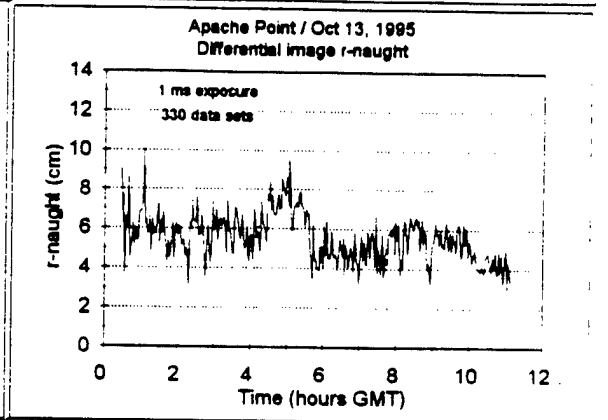
Apache Point / Oct 13, 1995
Differential image r-naught
1 ms exposure
330 data sets
r-naught (cm)
Time (hours GMT)

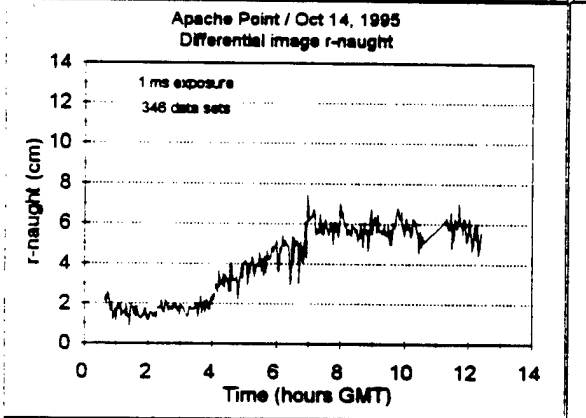
Apache Point / Oct 14, 1995
Differential image r-naught
1 ms exposure
348 data sets
r-naught (cm)
Time (hours GMT)

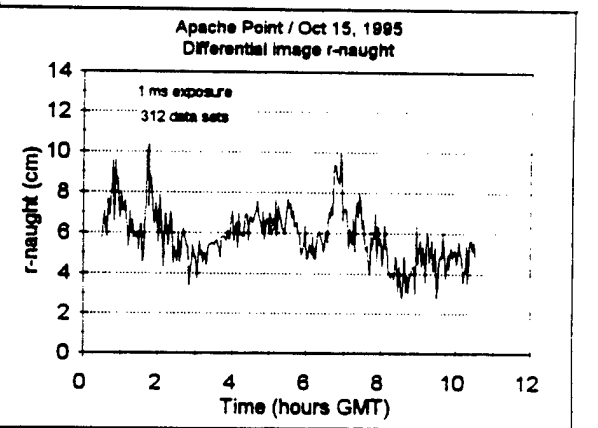
Apache Point / Oct 15, 1995
Differential image r-naught
1 ms exposure
312 data sets
r-naught (cm)
Time (hours GMT)

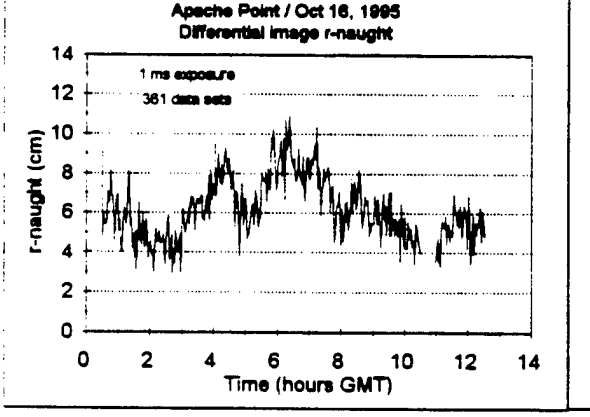
Apache Point / Oct 16, 1995
Differential image r-naught
1 ms exposure
361 data sets
r-naught (cm)
Time (hours GMT)

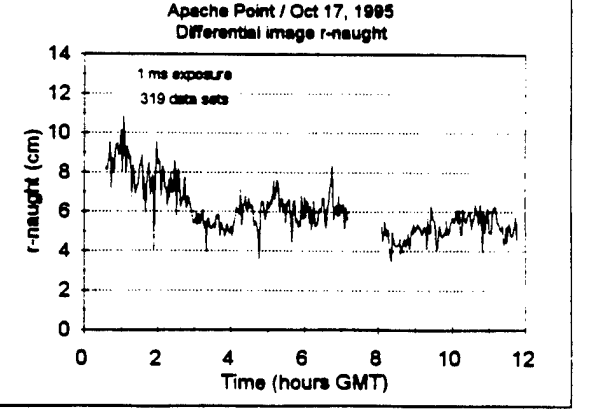
Apache Point / Oct 17, 1995
Differential image r-naught
1 ms exposure
319 data sets
r-naught (cm)
Time (hours GMT)

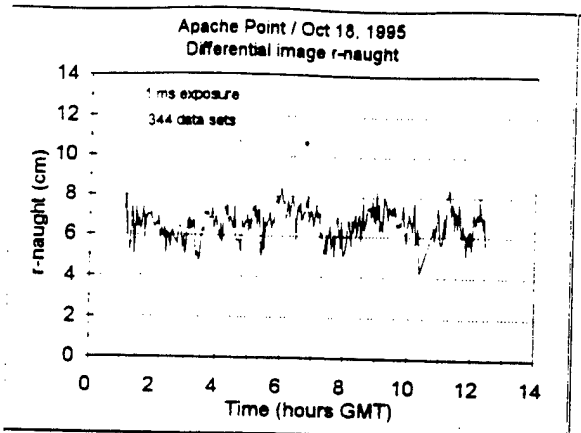
Apache Point / Oct 18, 1995
Differential image r-naught
1 ms exposure
344 data sets
r-naught (cm)
Time (hours GMT)

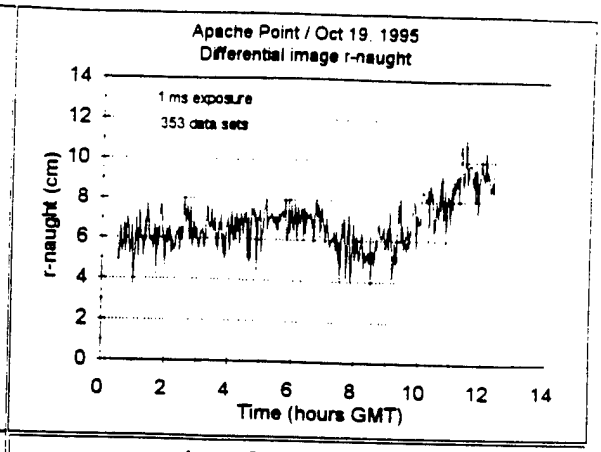
Apache Point / Oct 19, 1995
Differential image r-naught
1 ms exposure
353 data sets
r-naught (cm)
Time (hours GMT)

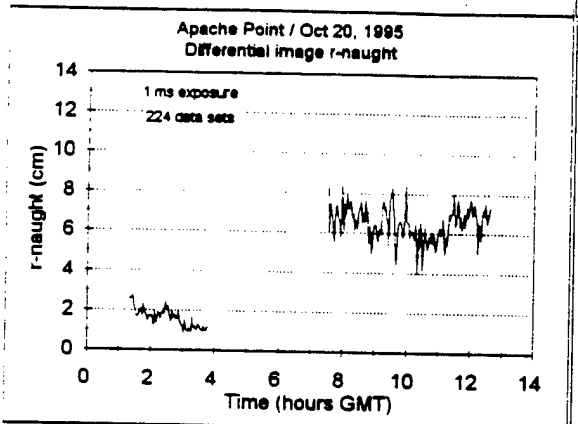
Apache Point / Oct 20, 1995
Differential image r-naught
1 ms exposure
224 data sets
r-naught (cm)
Time (hours GMT)

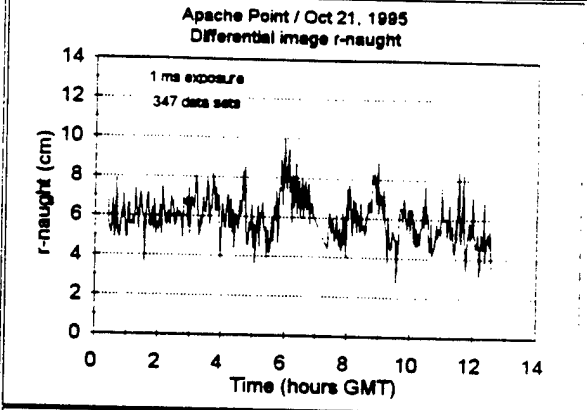
Apache Point / Oct 21, 1995
Differential image r-naught
1 ms exposure
347 data sets
r-naught (cm)
Time (hours GMT)

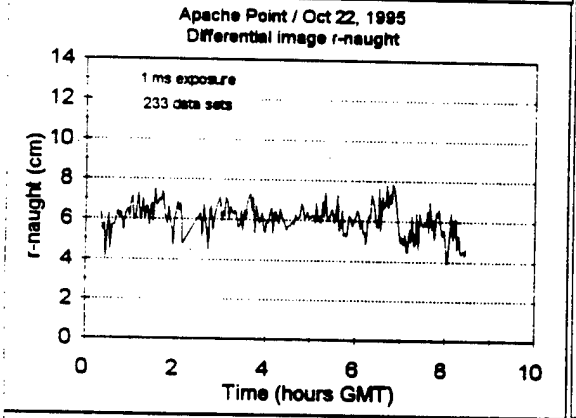
Apache Point / Oct 22, 1995
Differential image r-naught
1 ms exposure
233 data sets
r-naught (cm)
Time (hours GMT)

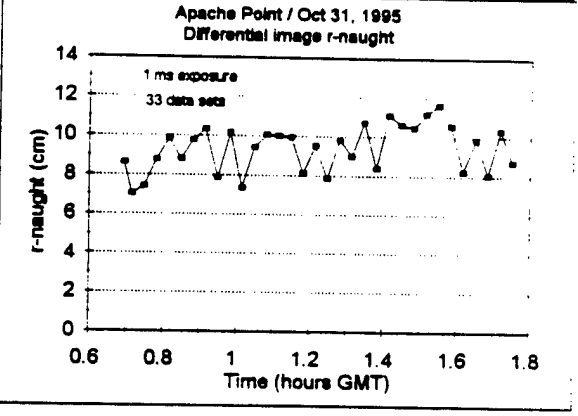
Apache Point / Oct 31, 1995
Differential image r-naught
1 ms exposure
33 data sets
r-naught (cm)
Time (hours GMT)

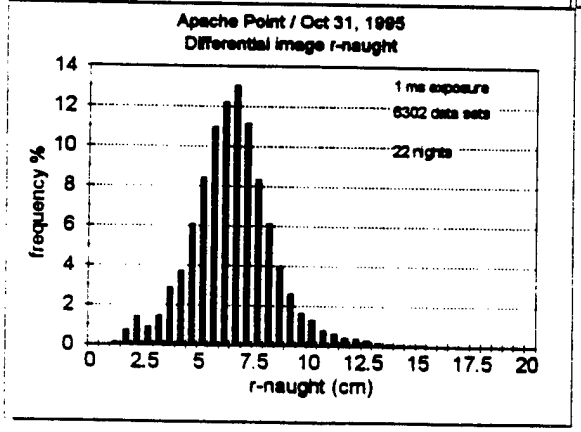
Apache Point / Oct 31, 1995
Differential image r-naught
1 ms exposure
6302 data sets
22 nights
frequency %
r-naught (cm)

Distribution

	Copies
NASA MARSHAL SPACE FLT CTR ATMOSPHERIC SCIENCES DIV E501 ATTN DR FICHTL HUNTSVILLE AL 35802	1
NASA SPACE FLT CTR ATMOSPHERIC SCIENCES DIV CODE ED 41 1 HUNTSVILLE AL 35812	1
ARMY STRAT DEFNS CMND CSSD SL L ATTN DR LILLY PO BOX 1500 HUNTSVILLE AL 35807-3801	1
ARMY MISSILE CMND AMSMI RD AC AD ATTN DR PETERSON REDSTONE ARSENAL AL 35898-5242	1
ARMY MISSILE CMND AMSMI RD AS SS ATTN MR H F ANDERSON REDSTONE ARSENAL AL 35898-5253	1
ARMY MISSILE CMND AMSMI RD AS SS ATTN MR B WILLIAMS REDSTONE ARSENAL AL 35898-5253	1

ARMY MISSILE CMND 1
AMSMI RD DE SE
ATTN MR GORDON LILL JR
REDSTONE ARSENAL
AL 35898-5245

ARMY MISSILE CMND 1
REDSTONE SCI INFO CTR
AMSMI RD CS R DOC
REDSTONE ARSENAL
AL 35898-5241

ARMY MISSILE CMND 1
AMSMI
REDSTONE ARSENAL
AL 35898-5253

CMD 420000D C0245 1
ATTN DR A SHLANTA
NAVAIRWARCENWPNDIV
1 ADMIN CIR
CHINA LAKE CA 93555-6001

PACIFIC MISSILE TEST CTR 1
GEOPHYSICS DIV
ATTN CODE 3250
POINT MUGU CA 93042-5000

LOCKHEED MIS & SPACE CO 1
ATTN KENNETH R HARDY
ORG 91 01 B 255
3251 HANOVER STREET
PALO ALTO CA 94304-1191

NAVAL OCEAN SYST CTR 1
CODE 54
ATTN DR RICHTER
SAN DIEGO CA 92152-5000

METEOROLOGIST IN CHARGE 1
KWAJALEIN MISSILE RANGE
PO BOX 67
APO SAN FRANCISCO
CA 96555

DEPT OF COMMERCE CTR 1
MOUNTAIN ADMINISTRATION
SPPRT CTR LIBRARY R 51
325 S BROADWAY
BOULDER CO 80303

DR HANS J LIEBE 1
NTIA ITS S 3
325 S BROADWAY
BOULDER CO 80303

NCAR LIBRARY SERIALS 1
NATL CTR FOR ATMOS RSCH
PO BOX 3000
BOULDER CO 80307-3000

DEPT OF COMMERCE CTR 1
325 S BROADWAY
BOULDER CO 80303

DAMI POI 1
WASH DC 20310-1067

MIL ASST FOR ENV SCI OFC 1
OF THE UNDERSEC OF DEFNS
FOR RSCH & ENGR R&AT E LS
PENTAGON ROOM 3D129
WASH DC 20301-3080

DEAN RMD 1
ATTN DR GOMEZ
WASH DC 20314

ARMY INFANTRY 1
ATSH CD CS OR
ATTN DR E DUTOIT
FT BENNING GA 30905-5090

AIR WEATHER SERVICE 1
TECH LIBRARY FL4414 3
SCOTT AFB IL 62225-5458

USAFETAC DNE 1
ATTN MR GLAUBER
SCOTT AFB IL 62225-5008

HQ AWS DOO 1 1
SCOTT AFB IL 62225-5008

PHILLIPS LABORATORY 1
PL LYP
ATTN MR CHISHOLM
HANSCOM AFB MA 01731-5000

ATMOSPHERIC SCI DIV 1
GEOPHYSICS DIRCTRT
PHILLIPS LABORATORY
HANSCOM AFB MA 01731-5000

PHILLIPS LABORATORY 1
PL LYP 3
HANSCOM AFB MA 01731-5000

ARMY MATERIEL SYST 1
ANALYSIS ACTIVITY
AMXSY
ATTN MP H COHEN
APG MD 21005-5071

ARMY MATERIEL SYST 1
ANALYSIS ACTIVITY
AMXSY AT
ATTN MR CAMPBELL
APG MD 21005-5071

ARMY MATERIEL SYST 1
ANALYSIS ACTIVITY
AMXSY CR
ATTN MR MARCHET
APG MD 21005-5071

ARL CHEMICAL BIOLOGY 1
NUC EFFECTS DIV
AMSRL SL CO
APG MD 21010-5423

ARMY MATERIEL SYST 1
ANALYSIS ACTIVITY
AMXSY
APG MD 21005-5071

ARMY MATERIEL SYST 1
ANALYSIS ACTIVITY
AMXSY CS
ATTN MR BRADLEY
APG MD 21005-5071

ARMY RESEARCH LABORATORY 1
AMSRL D
2800 POWDER MILL ROAD
ADELPHI MD 20783-1145

ARMY RESEARCH LABORATORY 1
AMSRL OP SD TP
TECHNICAL PUBLISHING
2800 POWDER MILL ROAD
ADELPHI MD 20783-1145

ARMY RESEARCH LABORATORY 1
AMSRL OP CI SD TL
2800 POWDER MILL ROAD
ADELPHI MD 20783-1145

ARMY RESEARCH LABORATORY 1
AMSRL SS SH
ATTN DR SZTANKAY
2800 POWDER MILL ROAD
ADELPHI MD 20783-1145

ARMY RESEARCH LABORATORY 1
AMSRL
2800 POWDER MILL ROAD
ADELPHI MD 20783-1145

NATIONAL SECURITY AGCY W21 1
ATTN DR LONGBOTHUM
9800 SAVAGE ROAD
FT GEORGE G MEADE
MD 20755-6000

OIC NAVSWC 1
TECH LIBRARY CODE E 232
SILVER SPRINGS
MD 20903-5000

ARMY RSRC OFC 1
AMXRO GS
ATTN DR BACH
PO BOX 12211
RTP NC 27709

DR JERRY DAVIS 1
NCSU
PO BOX 8208
RALEIGH NC 27650-8208

US ARMY CECRL 1
CECRL GP
ATTN DR DETSCH
HANOVER NH 03755-1290

ARMY ARDEC 1
SMCAR IMI I BLDG 59
DOVER NJ 07806-5000

ARMY SATELLITE COMM AGCY 1
DRCPM SC 3
FT MONMOUTH NJ 07703-5303

ARMY COMMUNICATIONS 1
ELECTR CTR FOR EW RSTA
AMSEL EW D
FT MONMOUTH NJ 07703-5303

ARMY COMMUNICATIONS 1
ELECTR CTR FOR EW RSTA
AMSEL EW MD
FT MONMOUTH NJ 07703-5303

ARMY DUGWAY PROVING GRD
STEDP MT DA L 3
DUGWAY UT 84022-5000 1

ARMY DUGWAY PROVING GRD
STEDP MT M
ATTN MR BOWERS
DUGWAY UT 84022-5000 1

DEPT OF THE AIR FORCE
OL A 2D WEATHER SQUAD MAC
HOLLOMAN AFB
NM 88330-5000 1

PL WE
KIRTLAND AFB NM
87118-6008 1

USAF ROME LAB TECH
CORRIDOR W STE 262 RL SUL
26 ELECTR PKWY BLD 106
GRIFFISS AFB
NY 13441-4514 1

AFMC DOW
WRIGHT PATTERSON AFB
OH 0334-5000 1

ARMY FIELD ARTLLRY SCHOOL
ATSF TSM TA
FT SILL OK 73503-5600 1

NAVAL AIR DEV CTR
CODE 5012
ATTN AL SALIK
WARMINISTER PA 18974 1

ARMY FOREGN SCI TECH CTR
CM
220 7TH STREET NE
CHARLOTTESVILLE
VA 22901-5396 1

NAVAL SURFACE WEAPONS CTR 1
CODE G63
DAHLGREN VA 22448-5000

ARMY OEC 1
CSTE EFS
PARK CENTER IV
4501 FORD AVE
ALEXANDRIA VA 22302-1458

ARMY CORPS OF ENGRS 1
ENGR TOPOGRAPHICS LAB
ETL GS LB
FT BELVOIR VA 22060

ARMY TOPO ENGR CTR 1
CETEC ZC 1
FT BELVOIR VA 22060-5546

LOGISTICS CTR 1
ATCL CE
FT LEE VA 23801-6000

SCI AND TECHNOLOGY 1
101 RESEARCH DRIVE
HAMPTON VA 23666-1340

ARMY NUCLEAR CML AGCY 1
MONA ZB BLDG 2073
SPRINGFIELD VA 22150-3198

USATRADOC 1
ATCD FA
FT MONROE VA 23651-5170

ARMY TRADOC ANALYSIS CTR 1
ATRC WSS R
WSMR NM 88002-5502

ARMY RESEARCH LABORATORY 1
AMSRL BE W
BATTLEFIELD ENVIR DIR
WSMR NM 88002-5501

ARMY RESEARCH LABORATORY AMSRL BE ATTN MR VEAZY BATTLEFIELD ENVIR DIR WSMR NM 88002-5501	1
DTIC 8725 JOHN J KINGMAN RD SUITE 0944 FT BELVOIR VA 22060-6218	1
ARMY MISSILE CMND AMSMI REDSTONE ARSENAL AL 35898-5243	1
ARMY DUGWAY PROVING GRD STEDP 3 DUGWAY UT 84022-5000	1
USATRADOC ATCD FA FT MONROE VA 23651-5170	1
WSMR TECH LIBRARY BR STEWS IM IT WSMR NM 88001	1
Record Copy	42
TOTAL	115